LARGE-EDDY SIMULATION AND RANS STUDIES OF THE FLOW AND HEAT TRANSFER IN A U-DUCT WITH TRAPEZOIDAL CROSS SECTION

by

**Kenny S. Hu**

A Dissertation

Submitted to the Faculty of Purdue University

In Partial Fulfillment of the Requirements for the degree of

Doctor of Philosophy
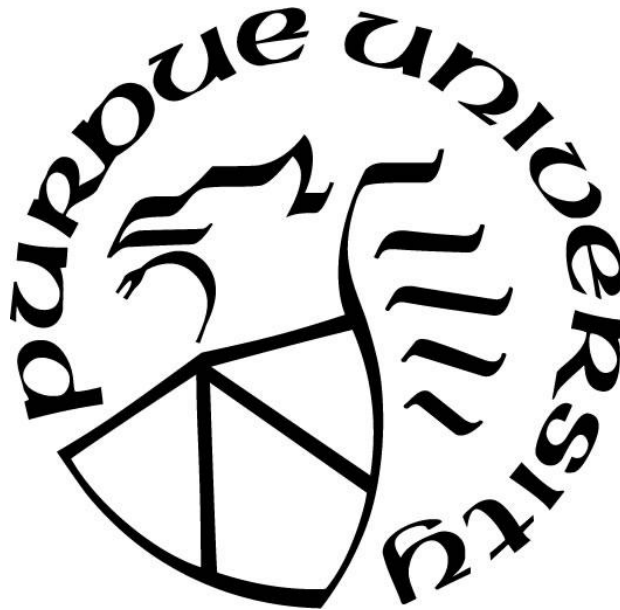
Department of Aeronautics and Astronautics

West Lafayette, Indiana

December 2018

THE PURDUE UNIVERSITY GRADUATE SCHOOL
STATEMENT OF DISSERTATION APPROVAL

Dr. Tom I-P Shih, Chair

    Department of Aeronautics and Astronautics

Dr. Gregory A. Blaisdell

    Department of Aeronautics and Astronautics

Dr. Jonathan Poggie

    Department of Aeronautics and Astronautics

Dr. Jun Chen

    Department of Mechanical Engineering

Approved by:

    Dr. Tom I-P Shih

        Head of the Departmental of Aeronautics and Astronautics

To my parents
Mr. Mou-ning Hu & Mrs. Pi-chu Lee

To my wife
Phoebe Hsiao-Fang Huang

To my son and daughter
Kendrick & Sophie

ACKNOWLEDGMENTS

I would like to acknowledge everyone who played a role in my academic accomplishments. First of all, I would like to thank my advisor Professor Tom I-P Shih, for his guidance for the past decade. Secondly, I would like to thank my mentor Xingkai Chi for his patience, support, and friendship in both academic and daily life. Third, I would like to thank my committee members, each of whom had provided advices throughout the research process. Fourth, I would like to thank my labmates for their enthusiasm and support in providing relevant assistance and help to complete this study. Thanks to Chien-Shing Lee, Jason Liu, Irsha Ashok Pardeshi, Ashutosh Pandey, Wanjia Zhang, Adwiteey Raj Shishodia, and James Peck. A special thank to Zachary Stratton for all the discussion and the course project relevant to this thesis, and the company during the travels to and in the conferences.

Also, I would like to express my deepest appreciation to my parents, my uncle, my wife, my children, and other members of my family for their emotional and financial support and providing a lovely environment for me.

Finally, I thank the American Society of Mechanical Engineers (ASME) and the American Institute of Aeronautics and Astronautics (AIAA) for granting me permission to use materials that my co-authors and I published in the following papers as a part of my dissertation: AIAA 2018-4432, GT2018-75530 and GT2018-75535.

TABLE OF CONTENTS

LIST OF FIGURES

NOMENCLATURE

D_h : hydraulic diameter

$D_{p,ij}$: pressure diffusion tensor

$D_{t,ij}$: turbulent diffusion tensor

h   : heat transfer coefficient

h_{avg} : area-weighted averaged heat transfer coefficient

h_0 : reference heat transfer coefficient

I   : turbulent intensity

k : turbulent kinetic energy

P_{exit} : pressure at the exit of the U-duct

Pr_t : turbulent Prandtl

q   : heat flux

$q_w^{''}$: local heat flux from the wall

Re   : Reynolds number (Re = $\rho V_{in} D_h / \mu$)

Re_τ : Reynolds number based on the friction velocity

            ($Re_\tau = \rho u_\tau D_h / \mu$)

T   : temperature

T_b : bulk temperature

$T_{b,in}$: bulk temperature at the inlet of the straight duct

T_{in} : temperature at the inlet of the U-duct

$T_{T,ij}$: turbulent transport tensor

T_w : wall temperature

u, v, w : x-, y-, z- components of the velocity vector

u_B : bulk velocity at the inlet of the straight duct

u_τ : friction velocity ($u_\tau = \sqrt{\tau_w / \rho}$), τ_w = averaged wall shear stress

|V| : velocity magnitude

V_{in} : magnitude of the mean velocity at the inlet of the U-duct

x, y, z : Cartesian coordinates for straight ducts

X, Y, Z : Cartesian coordinates for the U-duct

Greek

δ_{ij} : Kronecker delta

ε : dissipation rate of the turbulent kinetic energy

Γ_t : eddy-diffusivity of heat

μ_w : turbulent or eddy viscosity

Π_{ij} : pressure-strain rate tensor

ρ : density

τ_{ij} : Reynolds stress tensor

$\tilde{\tau}_{ij}$: subgrid-scale stress tensor

τ_w : averaged wall shear stress

υ : laminar viscosity

υ_{sgs} : subgrid-scale viscosity

$\upsilon_{t,eff}$: effective eddy-viscosity

ω : specific turbulent dissipation

ABSTRACT

Author: Hu, Kenny, S.-Y. Ph.D.
Institution: Purdue University
Degree Received: December 2018
Title: Large-Eddy Simulation And RANS Studies Of The Flow And Heat Transfer In A U-Duct
     With Trapezoidal Cross Section.
Committee Chair: Tom I-P Shih

The thermal efficiency of gas turbines increases with the temperature of the gas entering its turbine component. To enable high inlet temperatures, even those that far exceed the melting point of the turbine materials, the turbine must be cooled. One way is by internal cooling, where cooler air passes through U-ducts embedded inside turbine vanes and blades. Since the flow and heat transfer in these ducts are highly complicated, computational fluid dynamics (CFD) based on RANS have been used extensively to explore and assess design concepts. However, RANS have been found to be unreliable – giving accurate results for some designs but not for others. In this study, large-eddy simulations (LES) were performed for a U-duct with a trapezoidal cross section to assess four widely used RANS turbulence models: realizable k-ε (k-ε), shear-stress transport (SST), Reynolds stress model with linear pressure strain (RSM-LPS), and the seven-equation stress-omega full Reynolds stress model (RSM).

When examining the capability of steady RANS, two versions of the U-duct were examined, one with a staggered array of pin fins and one without pin fins. Results obtained for the heat-transfer coefficient (HTC) were compared with experimental measurements. The maximum relative error in the predicted "averaged" HTC was found to be 50% for k-ε and RSM-LPS, 20% for SST, and 30% for RSM-τω when there are no pin fins and 25% for k-ε, 12% for the SST and RSM-τω when there are pin fins. When there are no pin fins, all RANS models predicted a large separated flow region downstream of the turn, which the experiment does show to exist. Thus, all models predicted local distributions poorly. When there were pin fins, they behaved like guide vanes in turning the flow and confined the separation around the turn. For this configuration, all RANS models predicted reasonably well.

To understand why RANS cannot predict the HTC in the U-duct after the turn when there are no pin fins, LES were performed. To ensure that the LES is benchmark quality, verification and validation were performed via LES of a straight duct with square cross section

where data from experiments and direct numerical simulation (DNS) are available. To ensure correct inflow boundary condition is provided for the U-duct, a concurrent LES is performed of a straight duct with the same trapezoidal cross section and flow conditions as the U-duct. Results obtained for the U-duct show RANS models to be inadequate in predicting the separation due to their inability to predict the unsteady separation about the tip of the turn. To investigate the limitations of the RANS models, LES results were generated for the turbulent kinetic energy, Reynolds-stresses, pressure-strain rate, turbulent diffusion, pressure diffusion, turbulent transport, and velocity-temperature correlations with focus on understanding their behavior induced by the turn region of the U-duct. As expected, the Boussinesq assumption was found to be incorrect, which led to incorrect predictions of Reynolds stresses. For RSM-$\tau\omega$, the modeling of the pressure-strain rate was found to match LES data well, but huge error was found on modeling the turbulent diffusion. This huge error indicates that the two terms in the turbulent diffusion – pressure diffusion and turbulent transport – should be modeled separately. Since the turbulent transport was found to be ignorable, the focus should be on modeling the pressure diffusion. On the velocity-temperature correlations, the existing eddy-diffusivity model was found to be over simplified if there is unsteady separation with shedding. The generated LES data could be used to provide the guidance for a better model.

CHAPTER 1.   INTRODUCTION

The thermal efficiency of gas turbines can be improved by increasing the gas turbine inlet temperature. In the modern design of the gas turbines, the temperatures sought far exceed the melting temperature of the best superalloys. Thus, cooling is indispensable to ensure that all material of the gas turbine components never exceeds the maximum allowable temperature for strength and desired service life [1]. Since cooling requires work, the amount of coolant used should be kept to a minimum. Tremendous advances have been made in the internal cooling of turbine vanes and blades by using multi-pass serpentine passages that involve 180 degree turns and varying passage shape and aspect ratios [1-7] as well as a wide variety of heat-transfer enhancement features [1]. To make the next advance, a leap is needed in our understanding on how geometry affects the flow and surface heat transfer, including those enabled by addictive printing. Thus, high fidelity physics-based design tools such as computational fluid dynamics (CFD) are of interest.

The major challenge facing CFD is how to accurately and efficiently model and/or simulate the physics of turbulence. CFD based on the Reynolds-Averaged Navier-Stokes (RANS) equations is by far the most widely used tools to design internal-cooling strategies because it is computationally less demanding. Thus, there is considerable interest in RANS. However, since such models invoke a number of assumptions that limit their applicability, accuracy is a major concern [8-13].

On CFD studies of ducts with 180 degrees turns, referred to as U-ducts, most have focused on ducts with square or rectangular cross sections (see, e.g., [14] and the literature reviewed there). Also, almost all CFD studies of ducts have been based on RANS. Few have performed LES of ducts. Vázquez & Métais [15] used LES to analyze the turbulent flow through a heated straight square duct. Métais [16] and Munch [17] used LES to study a heated curved square ducts. They found a dean-type secondary flow to form that eventually caused the formation of Ekman vortices, which no RANS model can predict. Guleren & Turan [18] performed an LES study of a U-duct and provided data on its mean flow and its Reynolds stresses. So far, no studies have been reported on LES of flow and heat transfer in high-aspect ratio ducts and ducts with cross sections that are not square or rectangular.

CFD based on direct numerical simulation (DNS) have also been used to study turbulent flows in ducts. Huser & Biringen [19], Gavrilakis [20], and Joung et al. [21] performed DNS to study turbulent flow in a straight duct with square cross section. DNS has the potential to provide the most accurate and the most comprehensive data because all turbulent length and time scales are simulated by first principles [1]. However, it is currently limited to low-Reynolds-number flows because it is extremely demanding on computational resources. Since flows in turbine-cooling passages are typically at very high Reynolds-numbers, DNS is not feasible for studying turbine cooling under engine-relevant conditions.

Thus, for turbine cooling, LES is the best possible at present. Fortunately, LES should be adequate. This is because in LES, the large scales of the turbulent flow are also simulated by first principles just like DNS. Only the small scales are modeled, and those scales have fairly universal properties that can be expressed in terms of the resolved larger scales [22]. Also, for turbine cooling, it is the mean and the large-scale structures that dominate the mechanisms that affect the flow and heat transfer. The exception would be if there are chemical reactions and/or particulates in the turbulent flow, and their effects must be accounted for.

Though LES should be ideal for simulating turbine cooling flows, it is still expensive computationally. For example, each LES of a complicated problem could use hundreds of CPU or GPU cores and run for weeks, whereas RANS could do the same simulation with a small fraction of the cores and run time [23-25]. Parneix et al. [26] showed that some terms in RANS models can be substitute with LES or DNS data to improve accuracy. To assess the performance of RANS models, one needs benchmark-quality data that provides all information needed to calculate all terms in RANS models. LES can be used to generate the data set. Thus, the best use of LES is to understand the fundamental mechanisms of heat transfer and show where RANS models succeed and fail so that RANS models can be used correctly.

The organization of the rest of this thesis is as follows: First, steady RANS simulations are performed for trapezoidal U-ducts to examine the ability of four turbulence models – realizable k-ε (k-ε), shear-stress transport (SST), Reynolds stress model with linear pressure strain (RSM-LPS), and the seven-equation stress-omega full Reynolds stress model (RSM) – in CHAPTER 2. The results generated for the heat transfer coefficient (HTC) were compared with the experimental measurements. Next, in CHAPTER 3, LES was verified and validated by studying the flow in a square duct. LES is also performed in this chapter to examine the details

of the heat-transfer mechanisms in the U-duct with the same geometry as shown in CHAPTER 2. Results were compared with RANS results obtained in CHAPTER 2 and the experimental measurements. Afterwards, in CHAPTER 4, the LES results obtained in CHAPTER 3 were presented for the turbulent kinetic energy (TKE), Reynolds-stresses, pressure-strain rate, turbulent diffusion, turbulent transport, and velocity-temperature correlations with focus on understanding their behavior induced by the turn region of the U-duct. These results were compared with those predict by the RANS models to show their limitations and to provide data so that these models could be improved for computing this class of turbulent flows. This is followed by a conclusion of the key findings in CHAPTER 5.

CHAPTER 2.   STEADY RANS OF FLOW AND HEAT TRANSFER IN A SMOOTH AND PIN-FINNED TRAPEZOIDAL U-DUCT

An earlier version of this chapter was published as 'Kenny S.-Y. Hu, Xingkai Chi, Minking Chyu, Michael Crawford, and Tom I-P. Shih, "Steady RANS of Flow and Heat Transfer in a Smooth and Pin-Finned U-Duct with a Trapezoidal Cross Section," ASME Journal of Engineering for Gas Turbines and Power GTP-18-1307, Proceeding of ASME TurboExpo 2018, Turbomachinery Technical Conference & Exposition, June 2018, Oslo, Norway'.

2.1   Objective

The objective of this chapter is to assess the ability of four popular RANS models in predicting the turbulent flow and heat transfer in a U-duct that has a trapezoidal cross section with and without a staggered array of pin fins. The four RANS models to be examined are (1) the realizable k-ε model [27, 28]; (2) the shear-stress transport (SST) [29-32]; (3) the seven-equation Reynolds stress model with linear pressure strain (RSM-LPS) [25, 33-35], (4) the stress-omega full Reynolds stress model (RSM-$\tau\omega$) [11, 31].

The organization of the rest of this chapter is as follows: First, the U-duct problems studied are described. Next, the formulations of the problems along with the four turbulence models examined are given. This is followed by the numerical method of solution and efforts on verification. Afterwards, the results of this study are presented, which includes comparison with experimental data.

2.2   Problem Description

In the experimental study, the U-duct is fed by a series of ducts upstream as shown in Fig. 1. The U-duct is made with Plexiglas covered by liquid crystal. There are two variations. One has smooth walls, and the other has a staggered array of pins to enhance the heat transfer in the duct. Each of these U-ducts is described below.

2.2.1   Smooth U-Duct

A schematic of the smooth U-duct studied is shown in Fig. **2**. It has a trapezoidal cross section characterized by H_1= 11.72 mm, H_2= 28.48 mm, W_1= 54.24 mm, W_2= 114.83 mm, L_1=

246 mm, L_2= 192 mm, and d= 6.35 mm. The hydraulic diameter (D_h) of the trapezoidal cross section is 29.04 mm.

In this CFD study, the upstream duct is modeled as a straight duct with the same cross section as the U-duct and a length of $40D_h$. To ensure that there is no reverse flow at the U-duct's exit, a straight duct with the same cross section as the U-duct of length L_E = 13D_h was appended to the U-duct's exit. For this smooth U-duct, the wall temperature is maintained at T_w = 313.15 K, and the static pressure at the exit is maintained at P_{exit} = 1 atm. At the U-duct's inlet, air enters with uniform velocity V_{in} = 12.65 m/s and uniform temperature T_{in} = 343.15 K. This gives rise to a Reynolds number (Re) of 20,000 based on the hydraulic diameter, where all thermodynamic and transport properties are evaluated at $(T_{in}+T_w)/2$.

2.2.2   Pin-Finned U-Duct

A schematic of the U-duct with pin fins is shown in Fig. 3. It is identical to the smooth U-duct described in Fig. 2 except for the staggered array of pin fins. Each pin in this array extends from one wall to the other and has a diameter of d = 6.35 mm. The spacing between the center of the pins are characterized by P = 18.08 mm in the main flow direction and S = 15.67 mm in the spanwise direction. Since there is no reverse flow at the exit of the U-duct when there are pin fins, no extension duct was appended there. The operating conditions for the pin-finned duct are the same as that for the smooth duct. The smooth and pin-finned U-duct problems just described are both symmetric about y= 0. Thus, only a symmetric half of the problem need to analyzed in the CFD study.
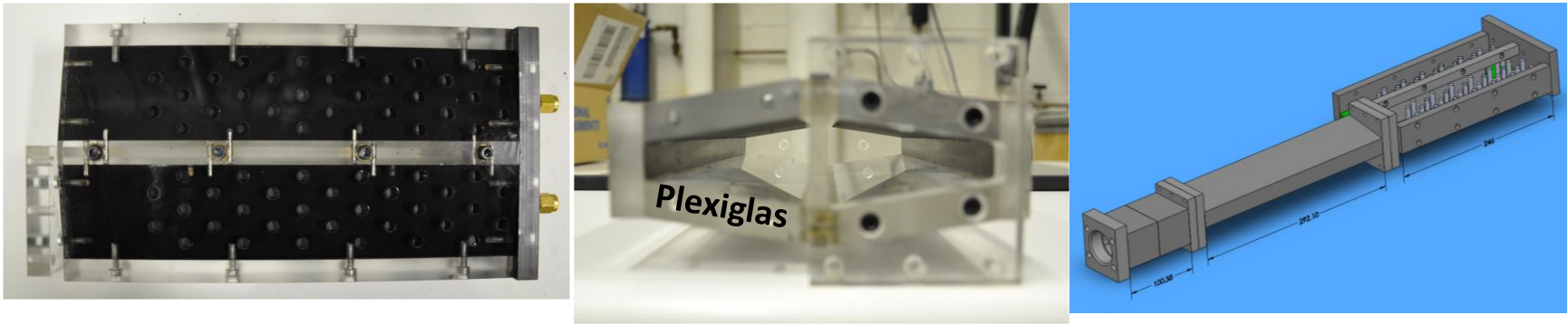
Figure 1. U-duct and the upstream straight duct used in experiment.

Unit: mm

D_h = 29.04	**Re** = **20,000**
d = 6.35	V_{in} = 12.65 m/s
L_1 = 246	T_{in} = 343.15 K
L_2 = 192	T_{wall}= 313.15 K
W_1 = 54.24	P_{exit} = 101325 Pa
W_2 = 114.83	I = 5%
H_1 = 11.72	
H_2 = 28.48	
L_E = 384	
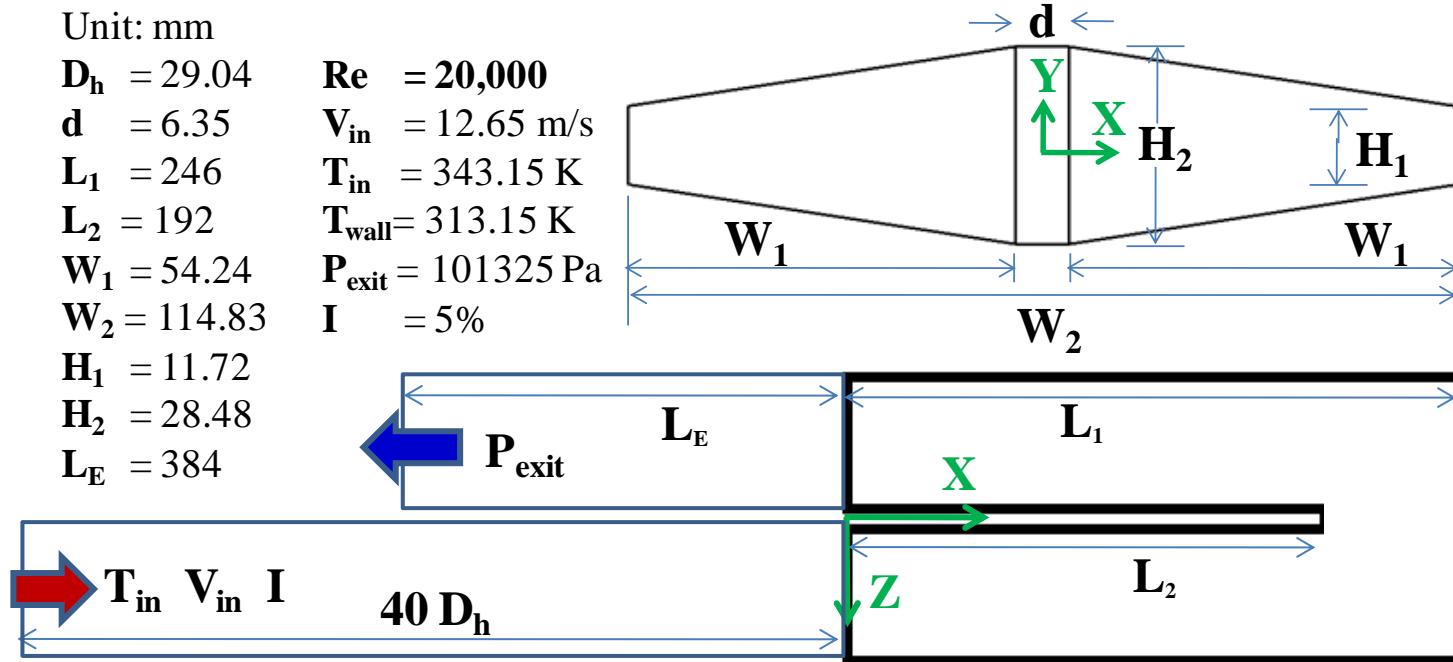
Figure 2. Schematic of the "smooth" U-duct.
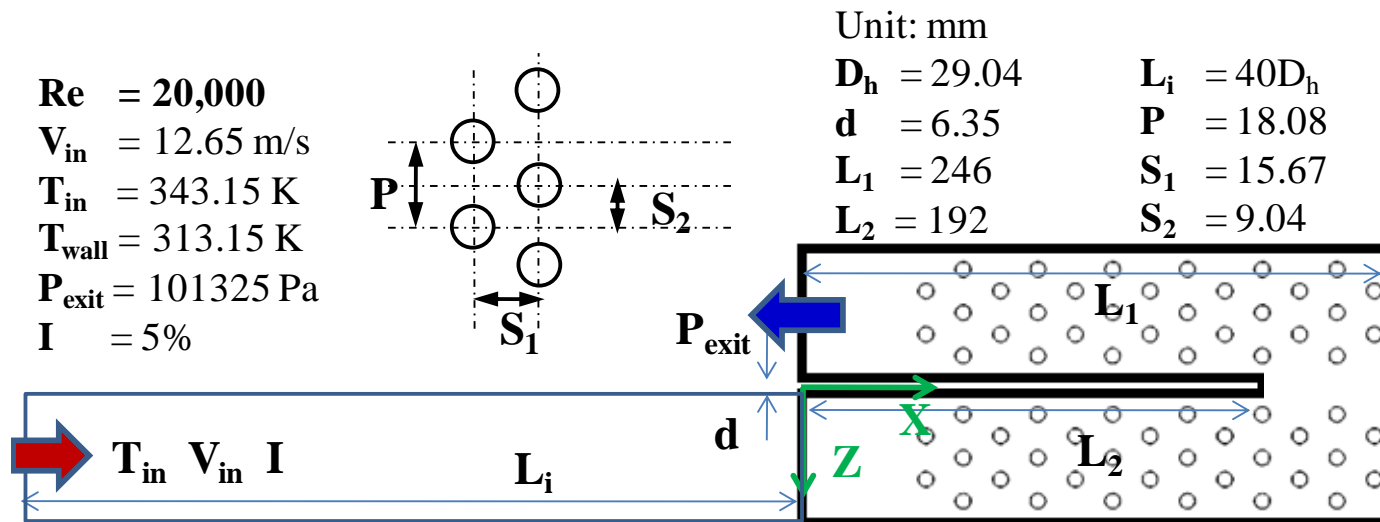
Figure 3. Schematic of the "pin-finned" U-duct.

2.3   Formulations

For the smooth and pin-fin U-duct problems described in the previous section, the flow is taken to be incompressible with constant properties.   All thermodynamic and transport properties were evaluated at T= $(T_{in}+T_w)/2$.   Also, viscous dissipation is neglected.   These assumptions are acceptable because the Mach number is less than 0.3, T_w–T_{in} is small, and the duct is relatively short so that the pressure drop is not high.   Analyses show the maximum density variation in the flow throughout the entire duct is less than 4% and the maximum error in transport properties is less than 1%.

2.3.1   Governing Equations

The governing equations used to describe the flow and heat transfer in the U-ducts are the Reynold-averaged continuity, momentum (Navier-Stokes), and thermal energy equations (RANS) for incompressible flow [36-25], and they are as follows:

$$\frac{\partial \overline{u}_j}{\partial x_j} = 0 \tag{1}$$

$$\frac{\partial \overline{u}_\iota}{\partial t} + \frac{\partial \overline{u}_j \overline{u}_\iota}{\partial x_j} = \nu \frac{\partial^2 \overline{u}_\iota}{\partial x_j^2} - \frac{1}{\rho}\frac{\partial \overline{p}}{\partial x_i} - \frac{\partial \tau_{ij}}{\partial x_j} \tag{2}$$

$$\frac{\partial \overline{T}}{\partial t} + \frac{\partial \overline{u}_\iota \overline{T}}{\partial x_i} = \frac{\partial}{\partial x_i}\left(\frac{k}{\rho C_p}\frac{\partial \overline{T}}{\partial x_i} - \overline{u_\iota' T'} \right) \tag{3}$$

where an overbar denotes a time-averaged quantity.   In this study, four models for the Reynolds stresses in the momentum equations, $\overline{u_i' u_j'}$, were examined: two eddy-viscosity models – the realizable k-ε model (k-ε) and the shear-stress transport (SST) model – and two Reynolds-stress models – Reynolds stress with linear pressure strain (RSM-LPS) and the stress-omega model (RSM-τω).   These models are described below.

2.3.2 Eddy-Viscosity Model

In eddy-viscosity model, the Reynolds stresses are given by

$$-\overline{u_i'u_j'} = 2\nu_T\left(S_{ij} - \frac{1}{3}\delta_{ij}S_{kk}\right) - \frac{2}{3}k\delta_{ij} \tag{4}$$

where $k = \overline{u_k'u_k'}/2$, $S_{ij} = \frac{1}{2}(\partial\overline{u}_i/\partial x_j + \partial\overline{u}_j/\partial x_i)$, and ν_T are the turbulent kinetic energy, mean strain-rate tensor, and the eddy viscosity, respectively. In the following, the two eddy-viscosity models evaluated are briefly described. They differ in how ν_T is modelled.

2.3.2.1 Realizable k-ε Model

For the realizable k-ε model, ν_T is modeled by

$$\nu_t = C_\mu \frac{k^2}{\varepsilon} \tag{5}$$

where

$$C_\mu = \frac{1}{A_0 + A_s \dfrac{k\tilde{S}}{\varepsilon}}$$

$$\tilde{S} = \sqrt{S_{ij}S_{ij}}, \quad S_{ij} = \frac{1}{2}\left(\frac{\partial u_j}{\partial x_i} + \frac{\partial u_i}{\partial x_j}\right)$$

The model constant $A_0 = 4.04$ and A_s are given by

$$A_s = \sqrt{6}\cos\phi$$

where

$$\phi = \frac{1}{3}\cos^{-1}(\sqrt{6}W), \ \ W = \frac{S_{ij}S_{jk}S_{ki}}{\widetilde{S}^3}$$

In the above equations, C_μ recovers the standard value of 0.09 in the fully turbulent region of the boundary layer. The turbulent kinetic energy, k, and its dissipation rate, ε, are obtained by the following transport equations:

$$\frac{\partial}{\partial t}(\rho k) + \frac{\partial}{\partial x_j}(\rho k u_j) = \frac{\partial}{\partial x_j}\left[\left(\mu + \frac{\mu_t}{\sigma_k}\right)\frac{\partial k}{\partial x_j}\right] + G_k - \rho\varepsilon \tag{6}$$

$$\frac{\partial}{\partial t}(\rho\varepsilon) + \frac{\partial}{\partial x_j}(\rho\varepsilon u_j) = \frac{\partial}{\partial x_j}\left[\left(\mu + \frac{\mu_t}{\sigma_\varepsilon}\right)\frac{\partial \varepsilon}{\partial x_j}\right] - \rho C_1 \frac{\varepsilon^2}{k + \sqrt{\nu\varepsilon}} \tag{7}$$

where G_k represents the generation of turbulent kinetic energy due to the mean velocity gradients. C_1 is constant. σ_k and σ_ε are the turbulent Prandtl numbers for k and ε, respectively.

2.3.2.2 SST Model

For the SST model, ν_T is modeled by

$$\mu_t = \frac{\rho k}{\omega}\frac{1}{\max\left[\frac{1}{\alpha^*}, \frac{SF_2}{a_1\omega}\right]} \tag{8}$$

where S is the strain rate magnitude and

$$F_2 = \tanh(\Phi_2^2)$$

$$\Phi_2 = \max\left[2\frac{\sqrt{k}}{0.09\omega y}, \frac{500\mu}{\rho y^2 \omega}\right]$$

$$\alpha^* = \alpha_\infty^*\left(\frac{\alpha_0^* + Re_t/R_k}{1 + Re_t/R_k}\right)$$

where

$$Re_t = \frac{\rho k}{\mu \omega}$$

The model constants $a_1 = 0.31\ R_k = 6,\ \alpha_0^* = 0.024$

The turbulent kinetic energy, k, and its dissipation rate, ε, are obtained by the following transport equations:

$$\frac{\partial}{\partial t}(\rho k) + \frac{\partial}{\partial x_i}(\rho k u_i) = \frac{\partial}{\partial x_j}\left[\left(\mu + \frac{\mu_t}{\sigma_k}\right)\frac{\partial k}{\partial x_j}\right] + \widetilde{G_k} - Y_k \tag{9}$$

$$\frac{\partial}{\partial t}(\rho \omega) + \frac{\partial}{\partial x_i}(\rho \omega u_i) = \frac{\partial}{\partial x_j}\left[\left(\mu + \frac{\mu_t}{\sigma_\omega}\right)\frac{\partial \omega}{\partial x_j}\right] + G_\omega - Y_\omega + D_\omega \tag{10}$$

In these equations, $\widetilde{G_k}$ represents the generation of turbulence kinetic energy due to mean velocity gradients. G_ω represents the generation of ω. σ_k and σ_ω are the turbulent Prandtl numbers for k and ω, respectively.

The k-ω model is substantially more accurate than k-ε in the near wall layers, and has therefore been successful for flows with moderate adverse pressure gradients, but fails for flows with pressure induced separation. In addition the ω-equation shows a strong sensitivity to the values of ω in the free-stream outside the boundary layer. The free-stream sensitivity has largely prevented the ω-equation from replacing the ε-equation as the standard scale-equation in turbulence modeling, despite its superior performance in the near wall region [32].

2.3.3 Reynolds Stress Model

The exact transport equation for the transport of the Reynolds stresses, τ_{ij}, may be written as follows:

$$\frac{\partial \tau_{ij}}{\partial t} + \underbrace{\bar{u}_k \frac{\partial \tau_{ij}}{\partial x_k}}_{Convection(C_{ij})}$$

$$= \underbrace{-\tau_{ik} \frac{\partial \bar{u}_j}{\partial x_k} - \tau_{jk} \frac{\partial \bar{u}_i}{\partial x_k}}_{Production(P_{ij})} + \underbrace{2\nu \overline{\frac{\partial u_i'}{\partial x_k} \frac{\partial u_j'}{\partial x_k}}}_{Dissipation\ (\epsilon_{ij})} + \underbrace{\overline{\frac{p'}{\rho}\left(\frac{\partial u_i'}{\partial x_j} + \frac{\partial u_j'}{\partial x_i}\right)}}_{Pressure-Strain\ (\Pi_{ij})}$$

$$+ \underbrace{\frac{\partial}{\partial x_k}\left(\underbrace{\nu\frac{\partial \tau_{ij}}{\partial x_k}}_{Viscous} + \underbrace{\overline{u_i'u_j'u_k'} + \overline{\frac{p'u_i'}{\rho}}\delta_{jk} + \overline{\frac{p'u_j'}{\rho}}\delta_{ik}}_{turbulent\ (D_{T,ij})}\right)}_{Transport\ by\ Diffusion}$$

Of all the various terms in these exact equations, convection, production, and viscous diffusion do not require any modeling. However, turbulent diffusion, pressure strain, and dissipation need to be modeled to close the equations. Beyond these three modeled terms, turbulent diffusion is modeled by the generalized gradient-diffusion model given by

$$D_{T,ij} = \frac{\partial}{\partial x_k}\left(\frac{\mu_t}{\sigma_k}\frac{\partial \overline{u_i'u_j'}}{\partial x_k}\right),$$

where the turbulent viscosity, μ_t, is computed similarly to the k-ε models, namely,

$$\mu_t = \rho C_\mu \frac{k^2}{\varepsilon}$$

with C_μ= 0.09 and ε is computed by using the ε transport equation. The dissipation tensor is modeled by

$$\varepsilon_{ij} = \frac{2}{3}\delta_{ij}\rho\varepsilon$$

For the pressure-strain rate, the classical approach uses the following decomposition:

$$\Pi_{ij} = \Pi_{ij,1} + \Pi_{ij,2} + \Pi_{ij,\omega}$$

$\Pi_{ij,1}$ is the slow pressure-strain term, $\Pi_{ij,2}$ is the rapid pressure-strain term, and $\Pi_{ij,\omega}$ is the wall reflection term.

Two models used in this study are described below.

2.3.3.1 RSM-LPS Model

In this model, the slow pressure-strain term is modeled as

$$\Pi_{ij,1} \equiv -C_1 \rho \frac{\varepsilon}{k} \left[\overline{u_i' u_j'} - \frac{2}{3} \delta_{ij} k \right]$$

where $C_1 = 1.8$.

The rapid pressure-strain term is modeled as

$$\Pi_{ij,2} \equiv -C_2 \left[\left(P_{ij} - \frac{2}{3} P_{kk} \right) - \left(C_{ij} - \frac{2}{3} C_{kk} \right) \right]$$

where $C_2 = 0.6$

The wall-reflection term is responsible for the redistribution of normal stresses near the wall. It tends to damp the normal stress perpendicular to the wall, while enhancing the stresses parallel to the wall. This term is modeled as

$$\Pi_{ij,\omega} \equiv C_1' \frac{\varepsilon}{k} \left(\overline{u_k' u_m'} n_k n_m \delta_{ij} - \frac{3}{2} \overline{u_i' u_k'} n_j n_k - \frac{3}{2} \overline{u_j' u_k'} n_i n_k \right) \frac{C_l k^{3/2}}{\varepsilon d}$$
$$+ C_2' \left(\Pi_{km,2} n_k n_m \delta_{ij} - \frac{3}{2} \Pi_{ik,2} n_j n_k - \frac{3}{2} \Pi_{jk,2} n_i n_k \right) \frac{C_l k^{3/2}}{\varepsilon d}$$

where $C_1' = 0.5$, $C_2' = 0.3$, n_k is the x_k component of the unit normal to the wall, d is the normal

distance to the wall, and $C_l = C_\mu^{3/4}/\kappa$, where $C_\mu = 0.09$, and κ is the von Kármán constant (=0.4187).

2.3.3.2   RSM-τω Model

This model is a stress-transport model that is based on the omega equation and LRR model. In this model, the wall reflections are excluded. The slow and rapid terms are shown below:

$$\Pi_{ij,1} \equiv -\beta_0^* f_{\beta^*} C_3 \omega \left[\overline{u_i' u_j'} - \frac{2}{3}\delta_{ij}k \right]$$

$$\Pi_{ij,2} \equiv -\hat{\alpha}\left(P_{ij} - \frac{2}{3}\delta_{ij}P_{kk} \right) - \hat{\beta}\left(D_{ij} - \frac{2}{3}\delta_{ij}P_{kk} \right) - \hat{\gamma}k\left(S_{ij} - \frac{1}{3}\delta_{ij}S_{kk} \right)$$

where, $\beta_0^* = 0.09$, $C_3 = 1.8$, $\hat{\alpha} = 0.774545$, $\hat{\beta} = 0.196364$, $\hat{\gamma} = 0.494545$, and

$$f_{\beta^*} = \begin{cases} 1 & \chi_k \leq 0 \\ \dfrac{1 + 640\chi_k^2}{1 + 400\chi_k^2} & \chi_k > 0 \end{cases}$$

$$\chi_k = \frac{1}{\omega^3}\frac{\partial k}{\partial x_j}\frac{\partial \omega}{\partial x_j}$$

$$P_{ij} = \tau_{im}\frac{\partial \bar{u}_j}{\partial x_m} + \tau_{jm}\frac{\partial \bar{u}_i}{\partial x_m}$$

$$D_{ij} = \tau_{im}\frac{\partial \overline{u_m}}{\partial x_j} + \tau_{jm}\frac{\partial \overline{u_m}}{\partial x_i}$$

$$S_{ij} = \frac{1}{2}\left(\frac{\partial \bar{u}_i}{\partial x_j} + \frac{\partial \bar{u}_j}{\partial x_i} \right)$$

2.3.4 Eddy Diffusivity Hypothesis (EDH)

The discussion so far only addressed how the Reynolds stresses are modeled in the momentum equations. In the energy equation, the correlation between velocity and temperature fluctuations, $\overline{u_i'T'}$, also needs to be modelled. In this study, that correlation is modeled by using the eddy-diffusivity concept given by

$$\overline{u_i'T'} = -\Gamma_t \frac{\partial T}{\partial x_i} \tag{11}$$

In the above equation, the bar denotes Reynolds averaging if RANS and spatially filtered if LES, and Γ_t is the eddy-diffusivity of heat. Reynolds analogy between heat and momentum transport suggests that Γ_t is closely related to the eddy or subgrid-scale viscosity μ_t so that

$$\Gamma_t = \frac{\mu_t}{Pr_t} \tag{12}$$

where Pr_t is the turbulent Prandtl number. In this study, Pr_t is taken to be 0.85.

2.4 Numerical Method

GAMBIT was used to generate the meshes, and version 16.2.0 of the Fluent UNS code [39] was used to generate all of the solutions. Since only steady-state solutions are sought, the SIMPLE algorithm is used as the solver. All equations are integrated over each cell. The fluxes for density, momentum, and energy at the cell faces are interpolated by using the second-order upwind scheme. Pressure was also computed by using second-order accuracy. For all simulations, iterations were continued until all residuals for all equations plateau to ensure convergence to steady-state has been achieved. At the convergence, it is always less than 10^{-5} for the three components of the velocity, less than 10^{-7} for the energy equation, less than 10^{-5} for turbulent kinetic energy, less than 10^{-4} for dissipation rate of turbulent kinetic energy, and less than 10^{-3} for the continuity equation.

2.4.1   Grid System of Smooth U-Duct

Figure 4 shows the three grids used for the smooth U-duct, and Fig. 5 shows the y^+ values of the first cell next to walls for those three grids. The coarse grid has 2,530,560 cells with the grid points nearly uniformly distributed. Since grid points were not clustered next to the wall, the y^+ values of the first grid points next to the walls range from 5 to 22. Thus, when the coarse grid is used, the "enhanced" wall functions was employed, which adjust points next to the wall to ensure that they are in the fully turbulent region of the inner boundary layer. The baseline grid has 3,694,080 cells, and the fine grid has 4,129,920 cells. For the baseline and fine grids, y^+ of the first grid point next to all walls is less than unity so that the integration for all turbulence models extends all the way to the wall. The grid spacing normal to all walls is constant for the first three cells next to all walls. Afterwards, the growth ratio of the grid spacing in the normal direction is 1.05.

2.4.2   Grid System of Pin-Finned U-Duct

Figure 6 shows the grid used for the "pin-finned" U-duct, which has 14,396,000 cells with grid points clustered to all walls. With this grid, Fig. 7 shows the y^+ values of the first grid points next to wall to be less than unity. Thus, the integration of all turbulence models extends to the wall. This grid was obtained based on the grid sensitivity study for the smooth U-duct (presented in the next section)

Coarse **Baseline** **Fine**

2,530,560 cells **3,694,080 cells** **4,129,920 cells**
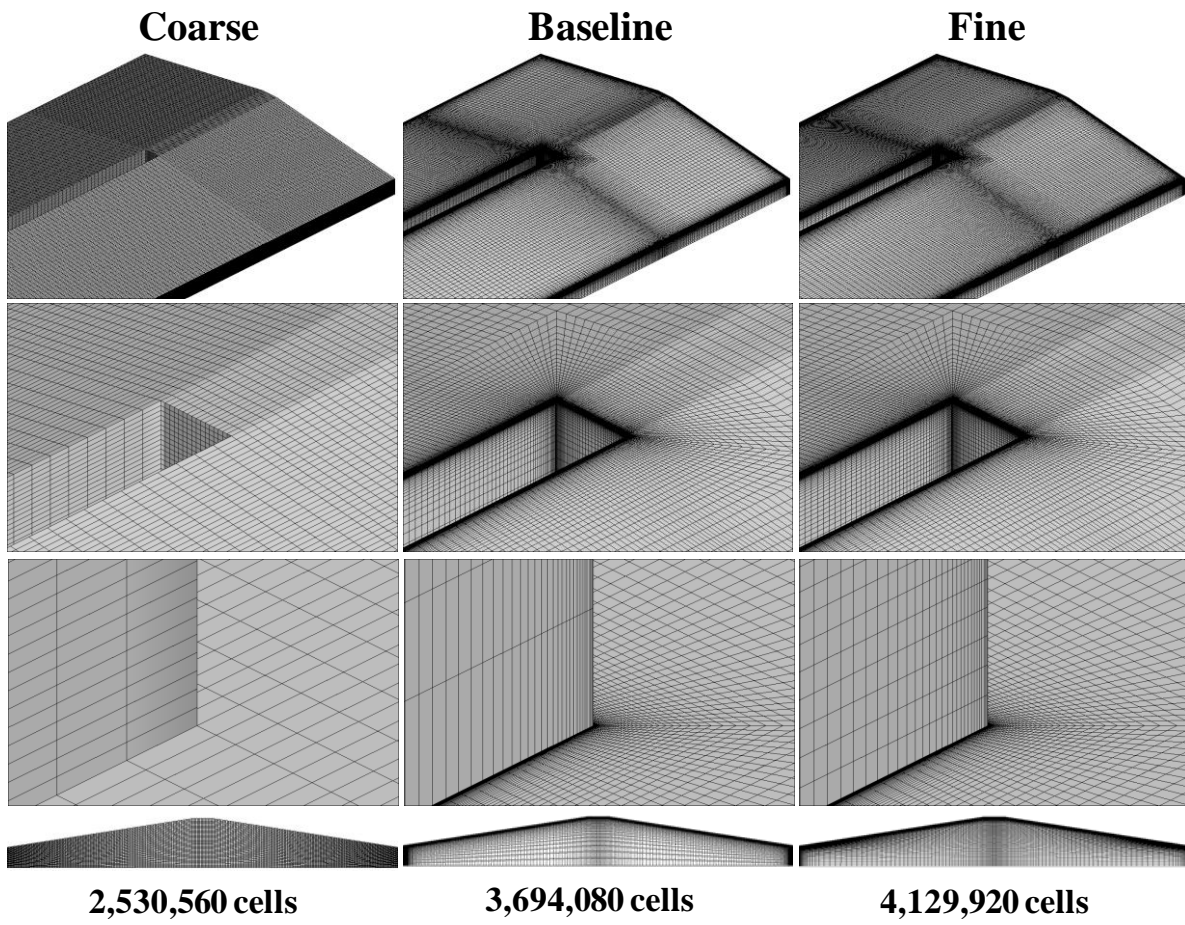
Figure 4. Grid systems used for the smooth U-duct problem.
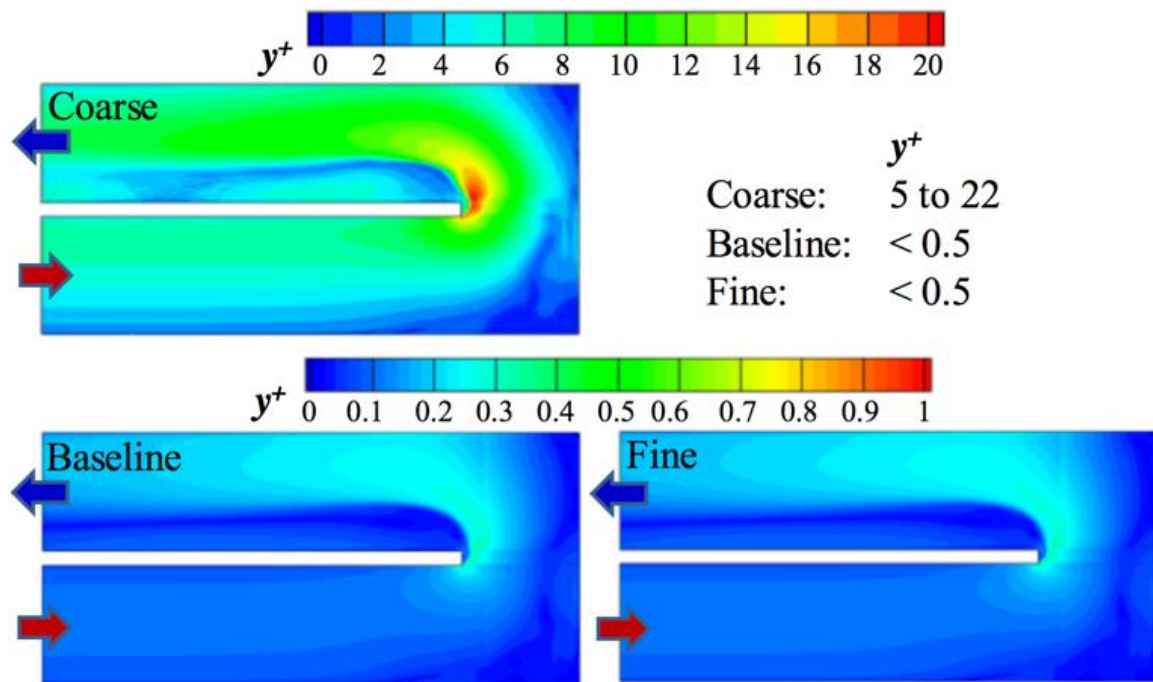
Figure 5. y^+ at one grid point away from walls for the smooth U-duct problem.
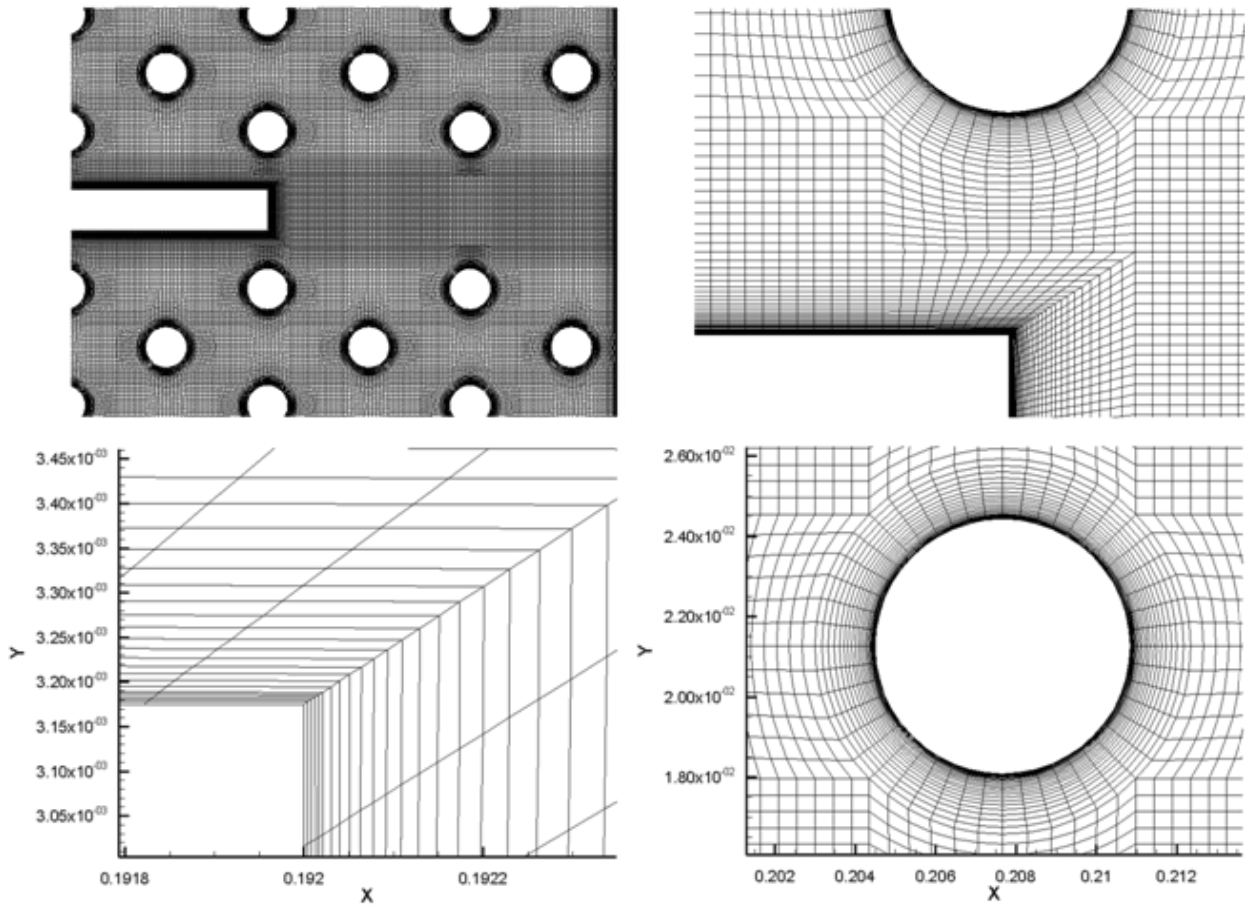
Figure 6. Grid systems used for the pin-finned U-duct problem.
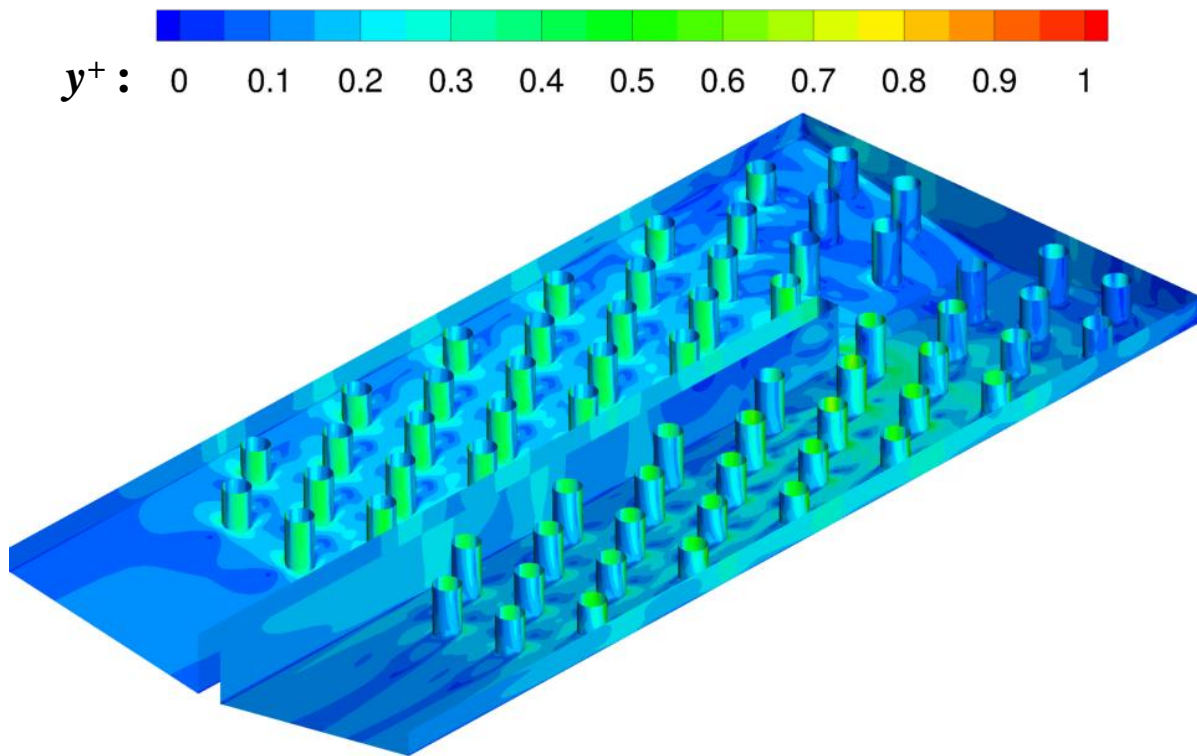
Figure 7. y^+ at one grid point away from walls for the pin-finned U-duct problem.

2.5   Results

    In this section, results on the grid sensitivity are first presented. Next, the experimental method used to obtain the heat-transfer coefficient (HTC) and the bulk temperature are described. Afterwards, results obtained by the four turbulence models examined – k-ε, SST, RSM-LPS, and RSM-τω – for the smooth the pin-finned U-ducts are described and compared with the measured HTC.

2.5.1   Grid-Independence Study

    To examine grid sensitivity, solutions were obtained on the three grids shown in Fig. 4. The solutions obtained by using the k-ε model are shown in Figs. 8 and 9. Figure 8 shows the average heat flux and heat-transfer rate on the top, inner, and outer walls of the smooth U-duct. Figure 9 shows the distribution of heat flux, velocity, and temperature along certain coordinates.

    From these figures, it can be seen that the solution obtained on the coarse grid differs considerably from those obtained on the baseline and fine grids. However, the solution obtained on the baseline grid is very similar to the solution obtained on the fine grid. The maximum relative error in the solution obtained on the baseline grid relative to the solution obtained on the fine grid is less than 2%. Thus, all solution reported in the remainder of this paper are obtained by using the baseline grid.

2.5.2   Experimental Data Used to Assess Turbulence Models

    The turbulence models examined in this study were assessed by comparing CFD predictions with experimentally measured HTC. The U-duct in the experiment is identical to the configuration shown in Fig. 3. The walls of the U-duct are made of Plexiglas of thickness 2.54 cm, and the pin fins are made of aluminum.

    The HTC on the surface of the U-duct exposed to the air flow is measured by using a transient method. Initially, the entire U-duct (Plexiglas walls for smooth U-Duct and Plexiglas walls plus aluminum pin fins for ribbed U-duct) and the air flow through the U-duct at Re = 20,000 are all at the same temperature (namely, the room temperature). Suddenly, at time t = 0, the temperature of air is raised to a higher temperature. With air having a higher temperature, the temperatures on all surfaces exposed to the hotter air change with time due to convective heat

transfer. These temperatures on the surface are measured by using thermochromic liquid crystals (TLCs), a thin film that is coated on those surfaces. The temperature measured at each point on the surface at time t, T(t), along with the measured Bulk temperature (to be explained) are inputted into the exact solution for 1-D unsteady conduction into a semi-infinite solid to get the HTC at that point on the surface. The Plexiglas wall can be approximated as a semi-infinite solid because the duration of the transient is short so that the temperature penetration into the Plexiglas is only a small fraction of the Plexiglas wall thickness. The details of the exact solution used and the experimental procedure as well as the error analyses are given in Refs. [40] and [41].

The HTC obtained by the experimental method just described is strongly dependent on how the bulk temperature is measured and defined throughout the U-duct. In the experiment, the bulk temperature is measured at six locations as shown in Fig. 10. The bulk temperatures along the up-leg and down-leg are interpolated from these measurements and are given by

$$T_{b,up-leg} = \frac{T_{TC1}(-x + 0.1666) + T_{turn}(x - 0.01429)}{0.15231}$$

$$T_{b,down-leg} = \frac{T_{TC6}(-x + 0.1666) + T_{turn}(x - 0.01429)}{0.15231}$$

where

$$T_{turn} = (T_{TC2} + T_{TC3} + T_{TC4} + T_{TC5})/4$$

With the bulk temperature defined, the heat transfer coefficient is calculated by

$$h = q_w''/(T_b - T_w)$$

where q_w'' is the local heat flux from the wall, and T_w is the wall temperature. When the CFD data is compared with the experiments, the CFD computed temperatures at those six thermocouple locations are used in the interpolation formulas for the bulk temperature.
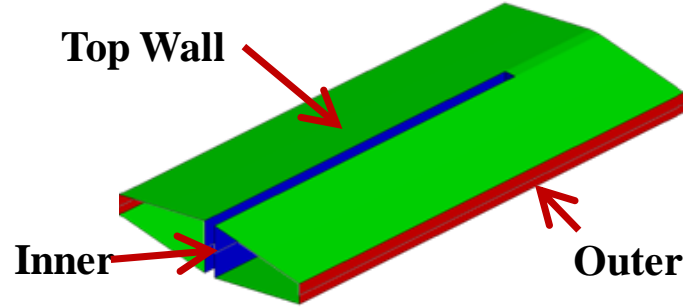
	coarse	baseline	fine
Inner	984	539	537
Outer	735	711	707
Top Wall	1005	940	938
Average	972	855	852
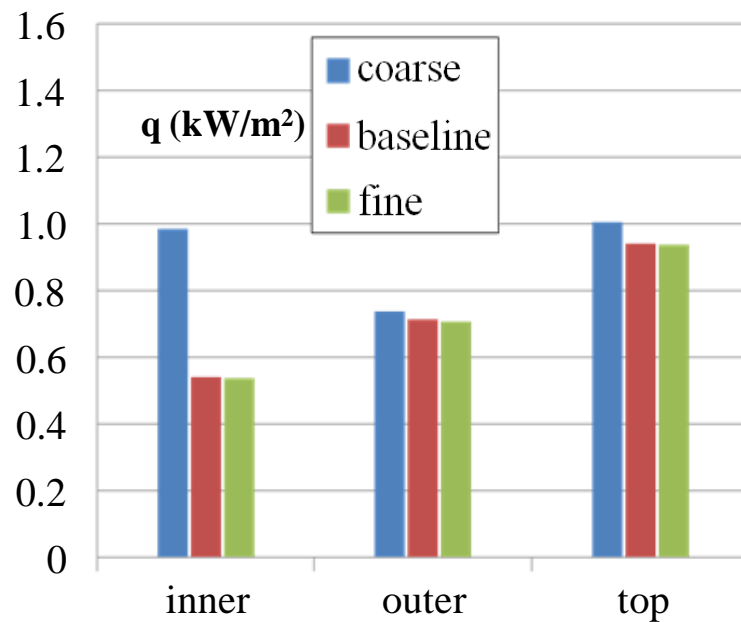
Figure 8. Predicted surface averaged heat flux on the walls of the smooth U-duct at Re = 20,000, generated on the grids shown in Fig. 4
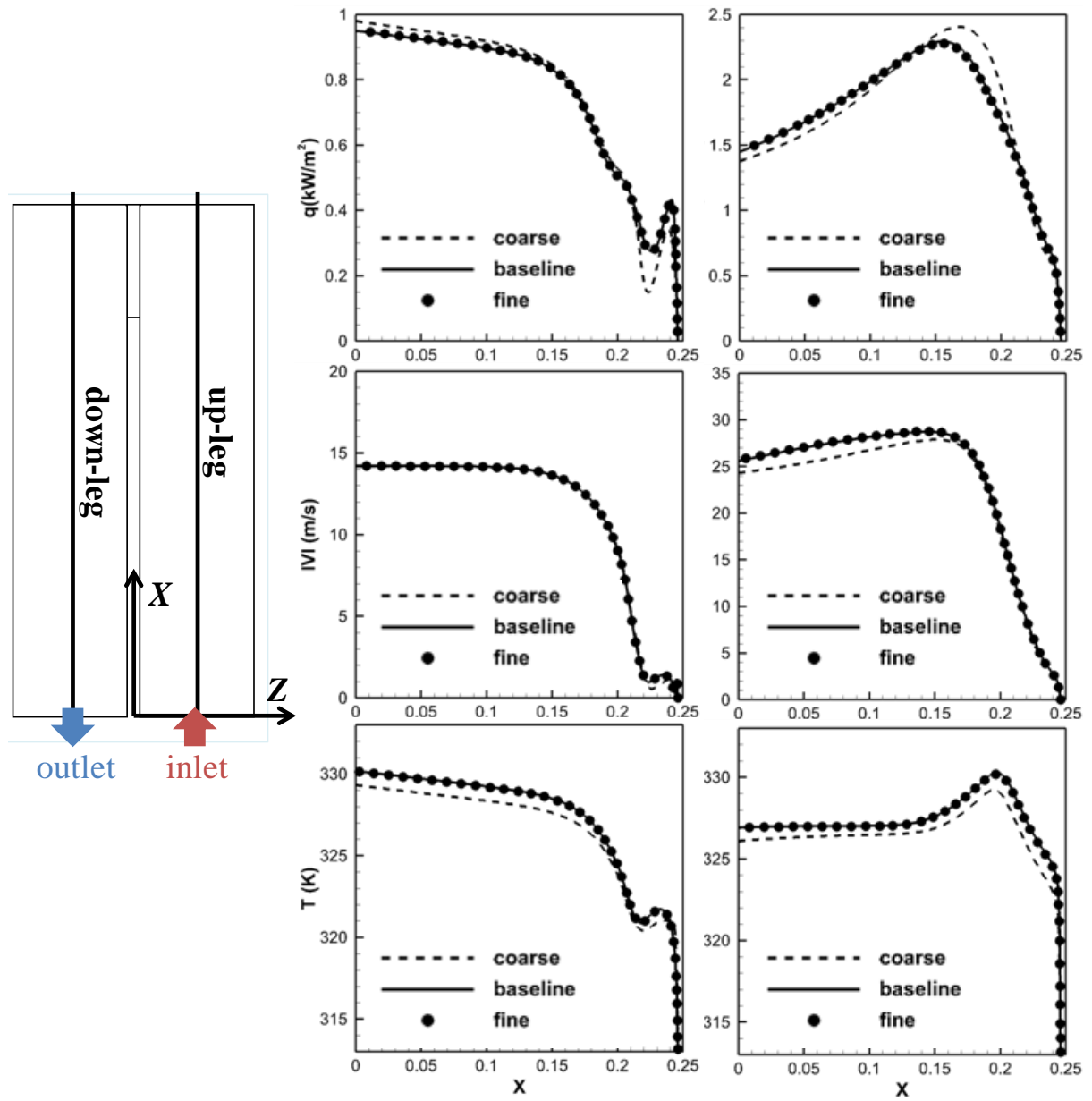
Figure 9. |V| and T along the center of the up- and down-leg duct obtained by the coarse, baseline, and fine grids.

Figure 10. The (x, y, z) coordinates of the six thermocouples to measure bulk temperature (all units are in meters).
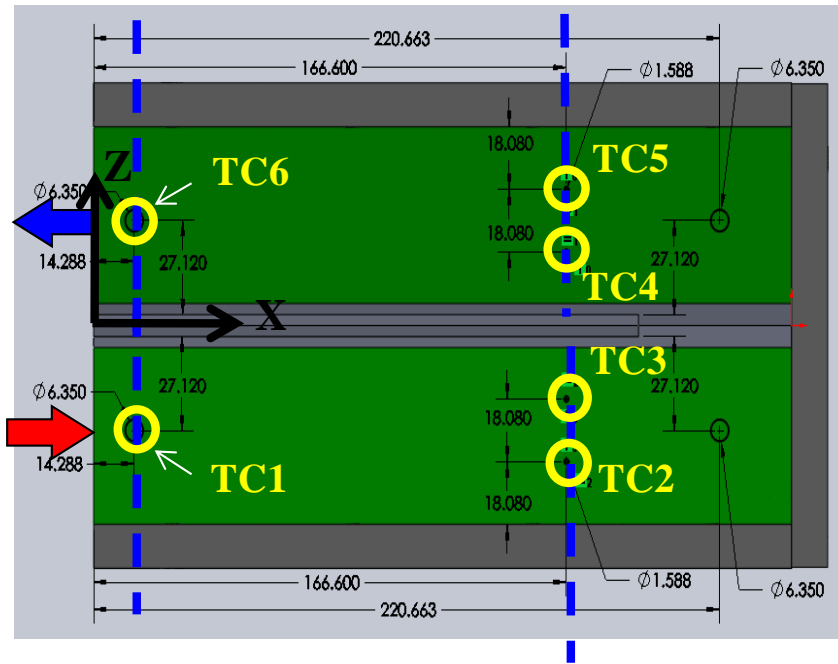
TC1: (0.01429, 0.005025, 0.030295)

TC2: (0.1666, 0.004367, 0.039335)
TC3: (0.1666, 0.005723, 0.021255)
TC4: (0.1666, 0.005723, -0.021255)
TC5: (0.1666, 0.004367, -0.039335)

TC6: (0.01429, 0.005025, -0.030295)

2.5.3   Results for the Smooth U-Duct

Since HTC is the only experimental data available for comparison, results for the HTC are presented first and compared with measurements. Afterwards, results for the flow are given.

2.5.3.1   Heat Transfer

Figure 11 show the computed and measured averaged HTC (h_{avg}) normalized by the HTC (h_0) calculated by Dittus-Boelter equation in four zones along the U-duct. From these figures, it can be seen that the predictions by SST and RSM-$\tau\omega$ are better than those by k-ε and RSM-LPS. However, all models yielded similar HTCs in the up-leg part, and the predicted regionally-averaged HTCs matched well with measurements. The maximum relative error is 2.5% for k-ε, SST, and RSM-$\tau\omega$ and 9% for RSM-LPS. In the turn region, where the largest discrepancies occur between computed and measured HTC, RSM-$\tau\omega$ predicts better than the other models. In the turn region, RSM-$\tau\omega$ provided the best predictions of the HTC. The maximum relative error is 14.5% for RSM-$\tau\omega$, 29% for SST, and 50% for k-ε and RSM-LPS. In the down-leg part after the turn region, SST gave the best predictions with maximum relative error less than 10%. The ability to correctly predict the secondary flow in the turn region and the separated flow downstream of the turn region dominated in how well the models predict the HTC. Though RSM-LPS is considerably more sophisticated and capable than k-ε, both predicted similar normalized averaged HTCs. This is because both models used the same one-equation model in the near-wall region. Thus, modeling of turbulence in the near-wall region plays a dominant role.

Figure 12 shows the total heat transfer rate in each of the four zones shown in Fig. 11. From this figure, it can be seen that all four turbulence models predict the total heat transfer rate similarly in zone 1. SST and RSM-$\tau\omega$ models predicted much higher total heat transfer rate in zones 2, 3, and 4 than those predicted by k-ε and RSM-LPS.

Comparing with RSM-$\tau\omega$ shows SST to predict higher total heat transfer rate in zones 3 and 4 and lower in zone 2. From Fig. 12, it can also be seen that the top surface provided the most heat-transfer rate in all four zones. However, the inner surface can contribute up to 20% in zone 1, and the tip-turn also can contribute up to 20% in zone 2. In zone 3, the contribution from the top surface dominates. In zone 4, the contribution from the outer surface varies from 10% to

14%, it is larger because there is jet-impingement heat transfer on this surface. Figure 13 shows the surface averaged heat transfer coefficient in zone 1, 2, 3, 4 and their sub-zones. From this figure, it can be seen that the inner surface (Inner-Up-Leg) has h_{avg} as large as that of the top surface, which means its contribution cannot be neglected; tip wall of zone 2 has higher h_{avg} than the top surface (more obvious for SST and RSM-$\tau\omega$); the outer region in zones 3 and 4 has very high h_{avg} caused by jet impingement on that surface; and the inner wall region in zone 4 has very low h_{avg} because there is a separation bubble formed on that surface.

The Nusselt numbers predicted by k-ε, SST, and RSM-$\tau\omega$ along with experimentally measured values are shown in Figs. 14 and 15. Results for RSM-LPS are not presented because they are similar to those obtained by k-ε (within 2% difference) due to the usage of the same one-equation model in the near-wall region by both k-ε and RSM-LPS. Though SST and RSM-$\tau\omega$ predicted better averaged HTC (or the averaged Nusselt number) than k-ε, when compared to the experimentally measured values, the local HTC or Nusselt number contours do not show this superiority in that they all appear quite different from the measured contours except in the up-leg part of the duct and the high Nusselt numbers near the tip wall predicted by SST and RSM-$\tau\omega$ but not by k-ε.

Most troubling is that measurements show the Nusselt number to be high next to the inner wall in the down-leg duct, but all models predicted very low values there. In the down-leg region, all RANS models over-predicted Nusselt number near the outer-wall and under-predicted it near the inner-wall. One reason is that all RANS models predicted a large separation bubble around the bend next to the inner surface, whereas measurements do not show such a separated region. Thus, being able to match the averaged HTC or Nusselt numbers is inadequate in assessing the predictive capabilities of turbulence models. It is important to examine the detailed distributions of the HTC or Nusselt number.

Use Dittus-Boelter equation to get reference h_0:

$$Nu_D = 0.023 \times Re^{0.8} \times Pr^{0.3}$$
$$= 57$$
$$h_0 = Nu_D * k / D_h = 55.6 (W/m2\text{-}K)$$

Zone 1: Top-Up-Leg
Zone 2: Top-Up-Turn
Zone 3: Top-Down-Turn
Zone 4: Top-Down-Leg

h_{avg}/h_0	Zone1	Zone2	Zone3	Zone4
k-ε	0.88	0.56	1.25	1.51
SST	0.88	0.78	2.06	2.06
RSM-LPS	0.94	0.58	1.29	1.55
RSM-$\tau\omega$	0.88	0.94	1.87	1.86
EXP	0.86	1.10	1.64	2.05
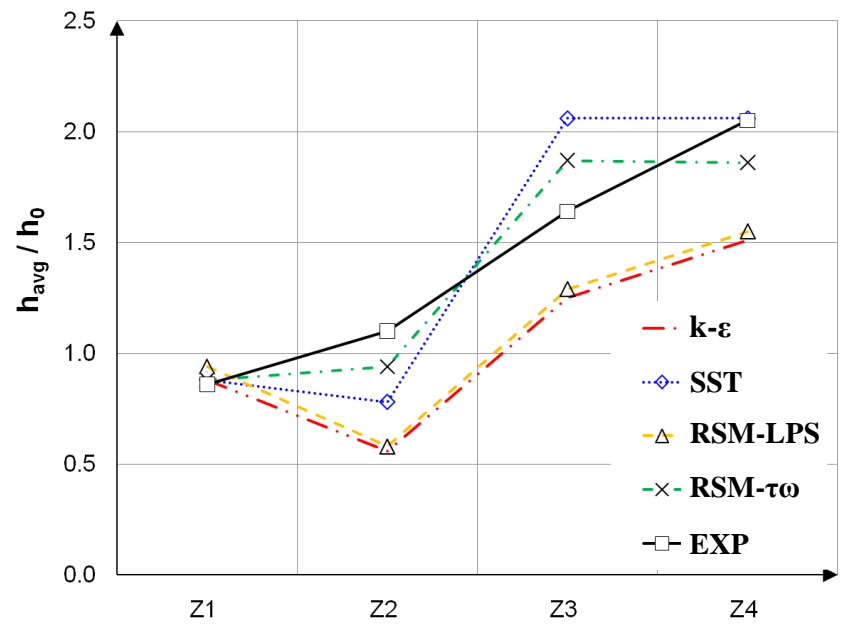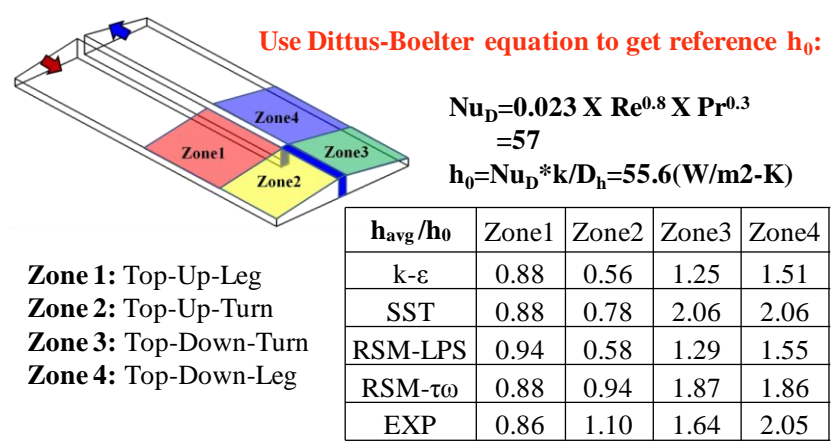
Figure 11. Computed and measured h_{avg}/h_0 in each zone

ZONE 1

	k-ε	SST	RSM-LPS	RSM-τω
■ Inner-Up-Leg	0.77	0.78	0.8	0.84
■ Outer-Up-Leg	0.14	0.11	0.16	0.16
■ Top-Up-Leg	2.97	2.97	3.01	2.93

ZONE 2

	k-ε	SST	RSM-LPS	RSM-τω
■ Tip-Up-Turn	0.21	0.51	0.24	0.68
■ Outer-Up-Turn	0.05	0.05	0.04	0.08
■ Top-Up-Turn	1.46	1.83	1.42	2.15

ZONE 3

	k-ε	SST	RSM-LPS	RSM-τω
■ Tip-Down-Turn	0.27	0.54	0.34	0.59
■ Outer-Down-Turn	0.25	0.57	0.27	0.54
■ Top-Down-Turn	3.11	4.81	3	4.33

ZONE 4

	k-ε	SST	RSM-LPS	RSM-τω
■ Inner-Down-Leg	0.27	0.35	0.29	0.38
■ Outer-Down-Leg	0.64	1.02	0.65	0.99
■ Top-Down-Leg	4.8	6.26	4.76	5.69

Figure 12. Total heat transfer rate, Q(W), in each zone.

ZONE 1

	k-ε	SST	RSM-LPS	RSM-τω
■ Top-Up-Leg	50.7	51.3	54.1	50.1
■ Outer-Up-Leg	22.8	18.5	27.2	25.1
■ Inner-Up-Leg	52.2	52.3	55.2	55.3
■ Zone1 Average	48.8	48.9	52.2	49.1

ZONE 2

	k-ε	SST	RSM-LPS	RSM-τω
■ Top-Up-Turn	34.1	42.9	34.6	50.2
■ Outer-Up-Turn	10.5	10.8	10.1	16.4
■ Tip-Up-Turn	27	65.5	31.1	86.3
■ Zone2 Average	31.1	43.4	32	52.5

ZONE 3

	k-ε	SST	RSM-LPS	RSM-τω
■ Top-Down-Turn	76.7	120.3	76.9	106.8
■ Outer-Down-Turn	60.5	137.3	65.9	127.1
■ Tip-Down-Turn	35.8	71.8	46.6	77.2
■ Zone3 Average	69.6	114.8	71.6	104.2

ZONE 4

	k-ε	SST	RSM-LPS	RSM-τω
■ Top-Down-Leg	96.3	128.4	98.3	114.2
■ Outer-Down-Leg	121.2	196.9	125.6	186.1
■ Inner-Down-Leg	21.1	27.8	23.3	29.1
■ Zone4 Average	84	114.7	86.2	103.6

Figure 13. Averaged HTC (W/m^2-K) in each zone.
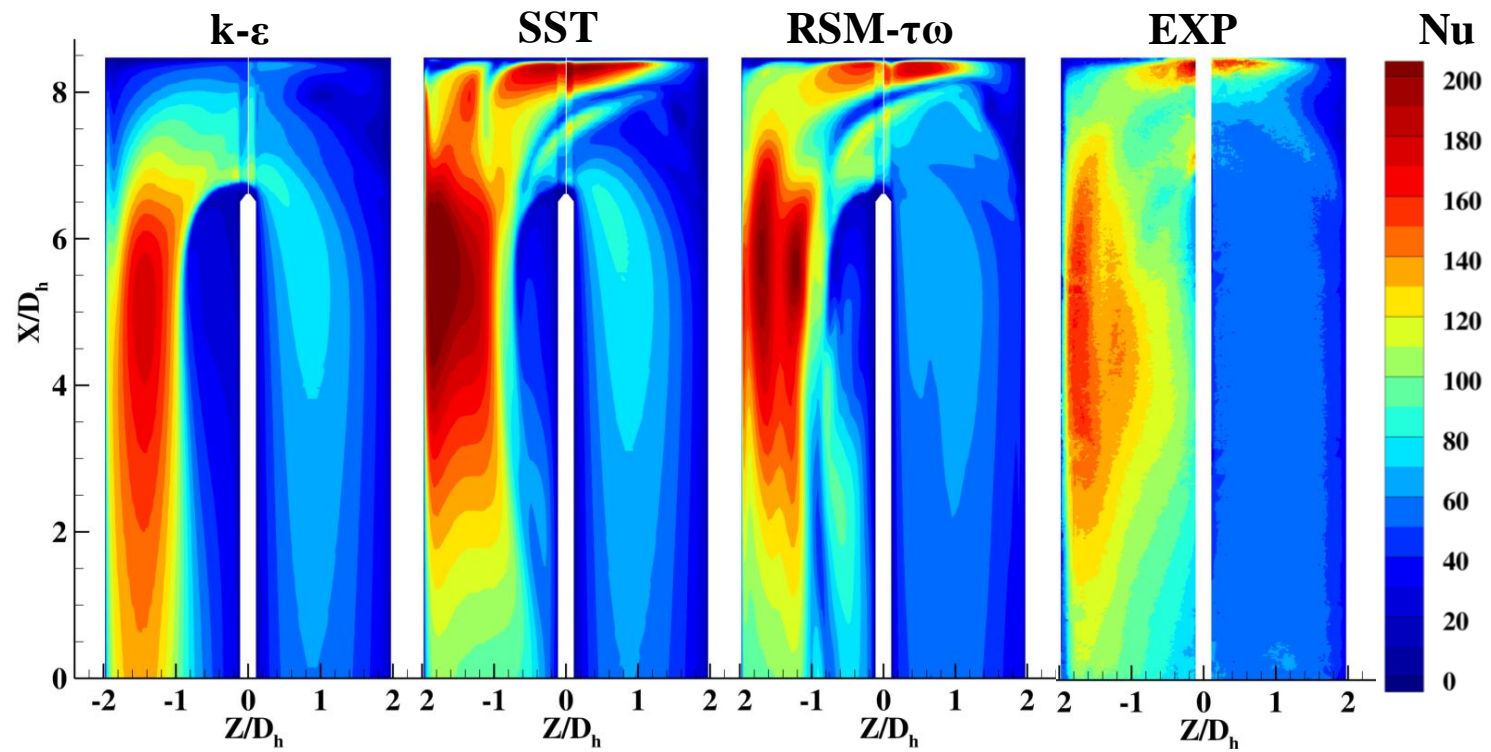
Figure 14. Nusselt number contours: RANS vs. EXP.
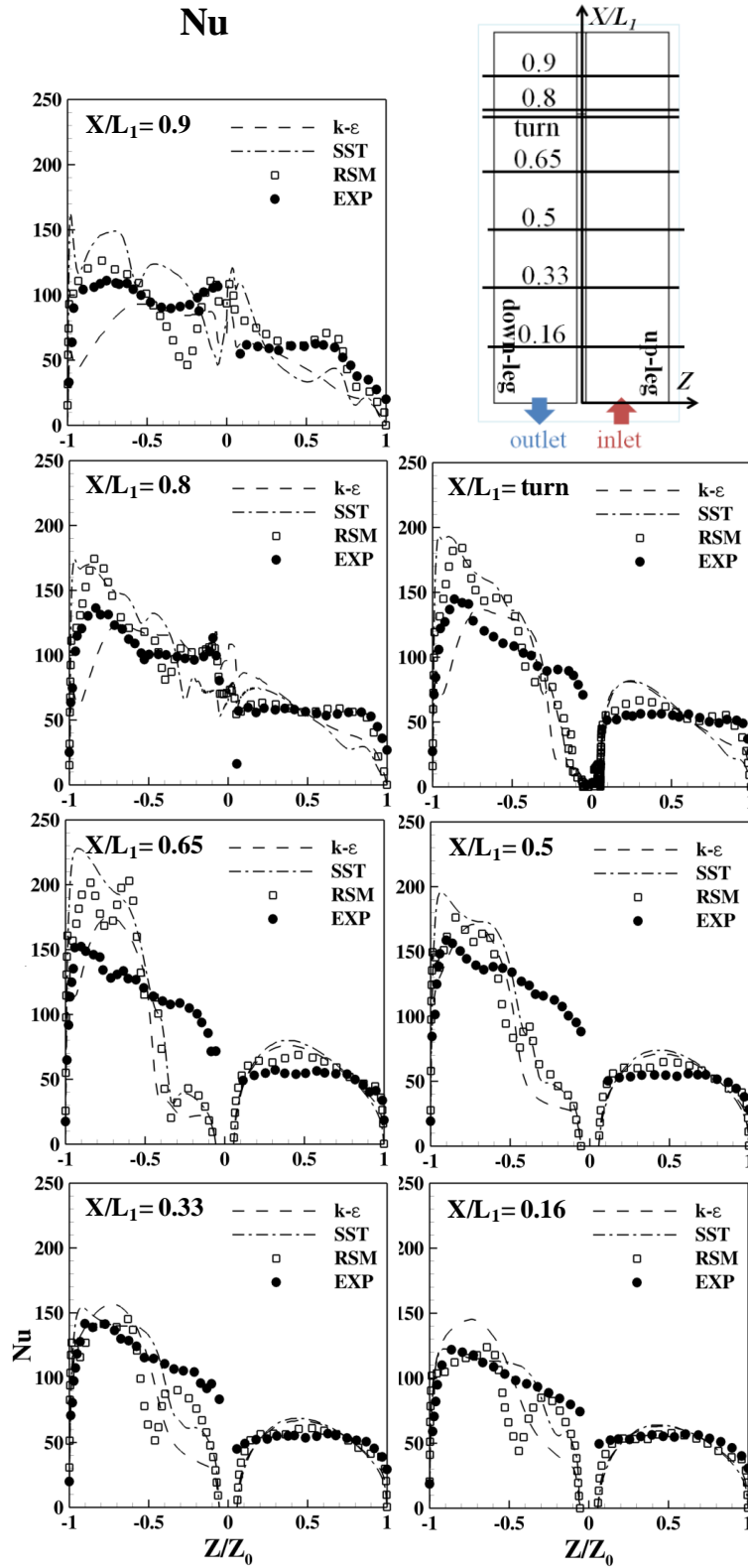
Figure 15. Nusselt number cat selected lines: RANS vs. EXP.

2.5.3.2   Flow Field

Figure 16 and 17 show the temperature contours and flow patterns predicted by the four turbulence models at selected planes. Observations made are as follows:

A.   In the up-leg duct, both Reynolds stress models are able to predict the corner vortices, while eddy-viscosity models are not due to the isotropy of Boussinesq assumption. However, these secondary flows vanish when the flow reaches the turn region. Despite this, all models predicted similar flow patterns at the beginning of the turn as shown in plane 2 in Fig. 16.

B.   Generally speaking, the flow patterns predicted by k-ε and RSM-LPS are more similar to each, and those predicted by SST and RSM-τω are more similar to each other. This is because k-ε and RSM-LPS use the same one-equation model of Chen and Patel in the near-wall region, and the SST and RSM-τω share the same ω-transport equation.

C.   The flow pattern predicted by k-ε and RSM-LPS differs from those predicted by SST and RSM-τω considerably, especially in the tip-turn region, where flow first impinges on the tip wall and then on the top wall.

D.   In the symmetry plane (plane I in Fig. 17), the temperature contours and flow patterns predicted by SST and both of the Reynolds stress models show similar results. But, as the planes approach the top wall, predictions by RSM-LPS approach those from k-ε.

E.   There are two main flow streams around the U-turn – one that flows around the tip of separator and another that impinges on the outer wall and then turns, which transports the cooler fluid to the top wall. This is why there are multiple areas of high heat transfer on the top wall, which are also observed in the measurement as shown in Fig. 14. These flows can be seen in plane 5 of Fig. 16 and in planes II and III of Fig. 17. These flows were predicted by SST and RSM-τω, but not by k-ε and RSM-LPS.
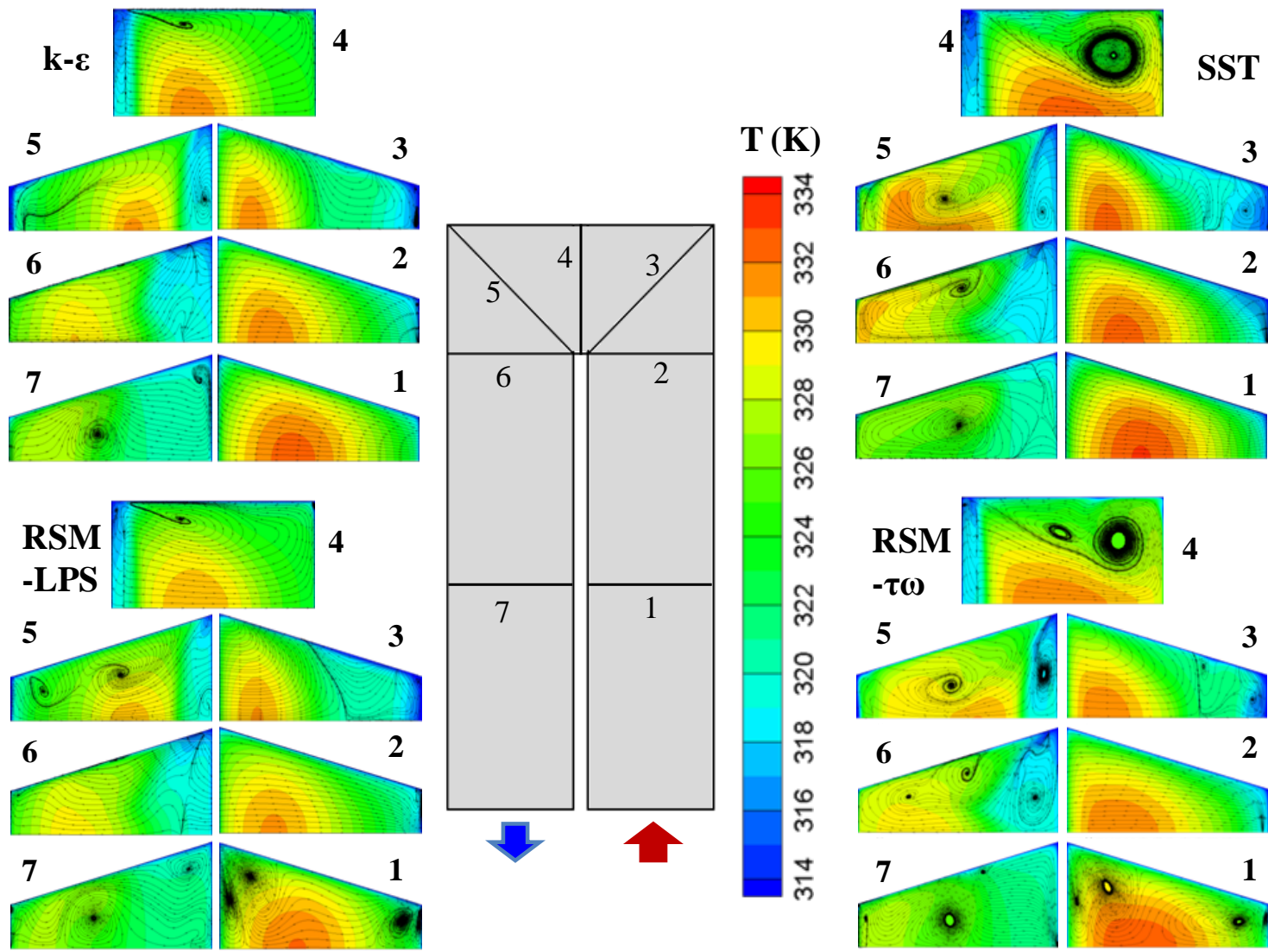
Figure 16. Streamlines colored by temperature at selected cutting planes.
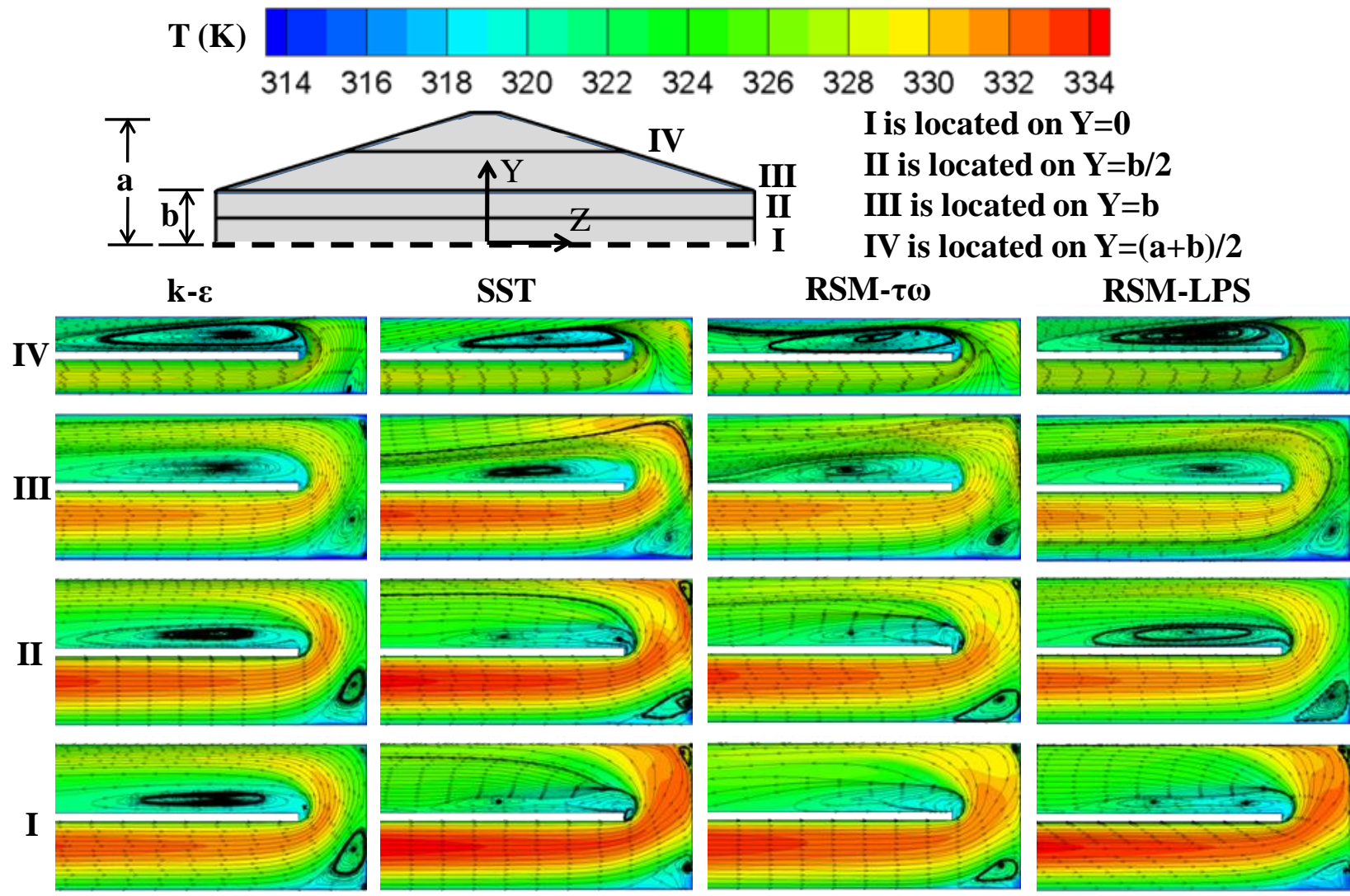
Figure 17. Streamlines colored by temperature at selected planes.

2.5.4   Results for the Pin-Finned U-Duct

In this section, results obtained for the pin-finned U-duct are described, and the HTC predicted are compared with measured values. Again, results for the RSM-LPS are not included because they are similar to those obtained by k-ε.

Figure 18 shows the contours of the HTC predicted by k-ε, SST, and RSM-τω, and those measured experimentally.   Generally speaking, the results obtained by all models match measurement reasonably well.   One reason is that with pin fins, there are no large separated regions in and after the turn region. On specifics, all models predicted high HTC at the leading edge of each pin fin and around the base of each pin fins on the top and bottom walls about its leading edge. Also, all models predicted lower HTC in the wake region. However, all RANS models predicted HTCs that were considerably lower than those measured. This may be caused by unsteadiness of the flow in the wake region because of shedding that was not captured by steady RANS. Figure 18 also shows SST and RSM-τω to predict very similar results.

To compare quantitatively, the top wall of the U-Duct was divided into six zones as shown in Fig. 19. The HTC in each zone was averaged. From Fig. 19, it can be seen that all models predicted lower HTC than measurements.   Again, the reason is the mean flow is inherently unsteady because of the shedding behind each pin fin, and this CFD study used steady RANS instead of unsteady RANS. Of the models examined, k-ε predicted the worst. SST predicted as well as RSM-τω in zone 1, 2, 3 and 5 and better in zone 4 and 6. Thus, SST is the best model for predicting HTC in the pin-finned U-duct.

Figure 20 shows the enhancement in the HTC enable by the array of pin fins, where the enhancement is defined by

$$G_{h,avg,i}^{pin-fins} = \frac{h_{avg,i}^{pin-fins} - h_{avg,i}^{smooth}}{h_{avg,i}^{smooth}}$$

where the superscript denotes the types of the U-duct (i.e., smooth duct or pin-finned duct), and the subscript denotes the zones. Based on this definition, positive indicates enhancement. From Fig. 20, it can be seen that there is appreciable enhancement in Z2 and Z3.   In Z4, there is actually negative enhancement, and only slight positive enhancement in Z5.

However, this discussion only considered enhancement of the HTC on the top wall and excluded heat transfer through the pin fins. The heat transfer through the pin fins is appreciable. Thus, adding pin fins greatly enhances heat transfer in the U-duct because of the unsteadiness created by the shedding and by the increased surface area.

Figure 21 shows the streamlines colored by temperature in the symmetry plane. From this figure, it can be seen that the pin fins in the turn region to behave like guiding vanes in turning the flow around the bend. Thus, the pin fins prevented the impingement that occurred around the tip wall region in the case of smooth walls, resulting in lower heat transfer on the tip wall. Figure 21 also shows the pin fins to prevent the formation of a large separated region after the bend by behaving like guide vanes in the turn region. Without the separated region, all RANS models were able to predict HTCs that qualitatively compared well with measurements in the down-leg duct.
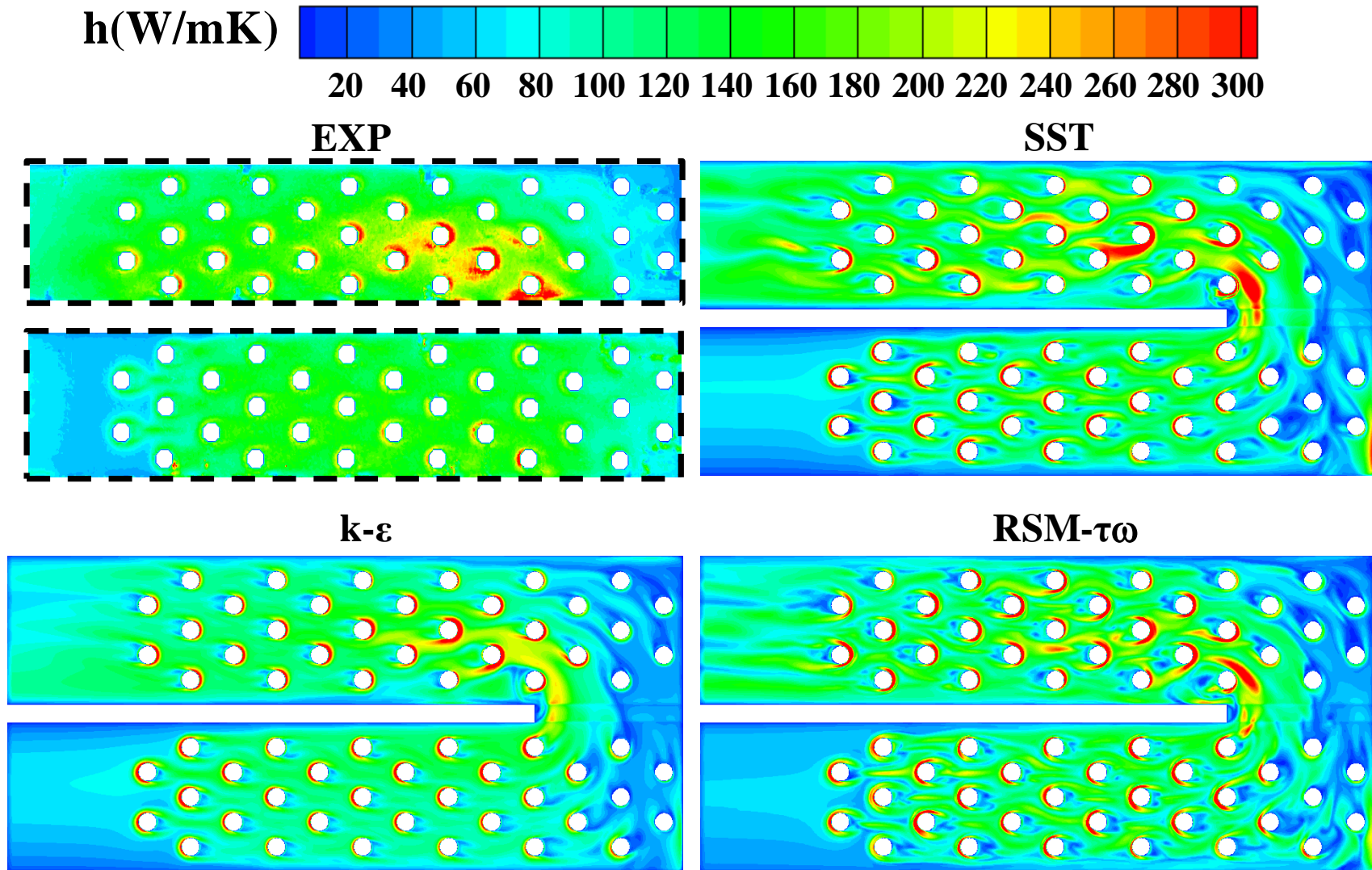
Figure 18. Computed and measured HTC on the top wall for pin-finned U-duct.
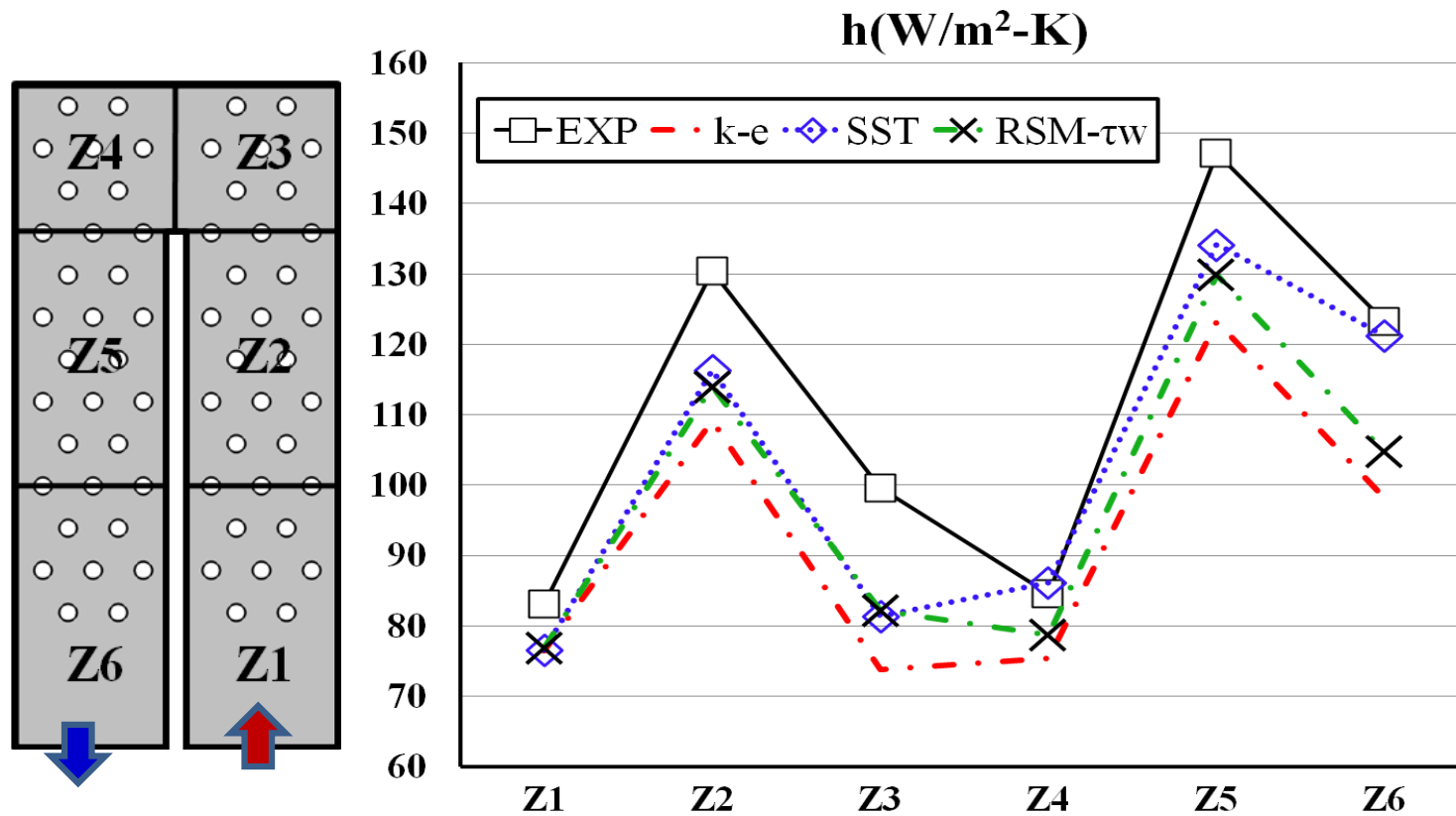
Figure 19. Computed and measured averaged HTC in each zone for pin-finned U-duct.
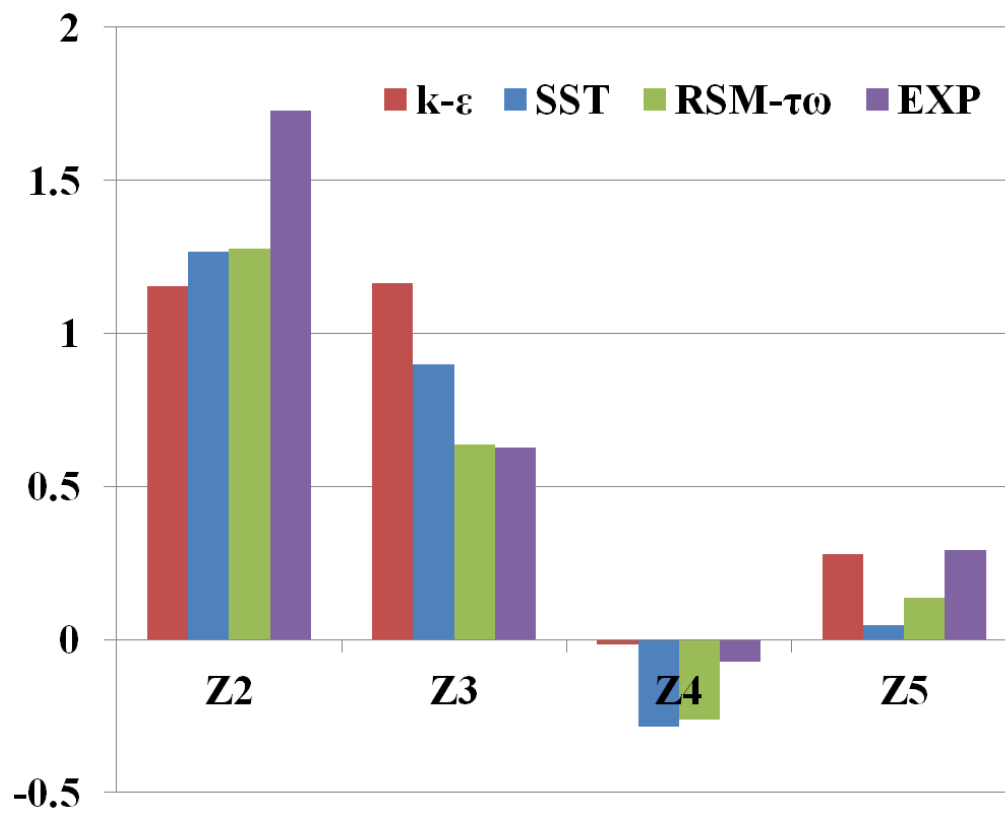
Figure 20. Heat transfer enhancement enabled by pin fins.
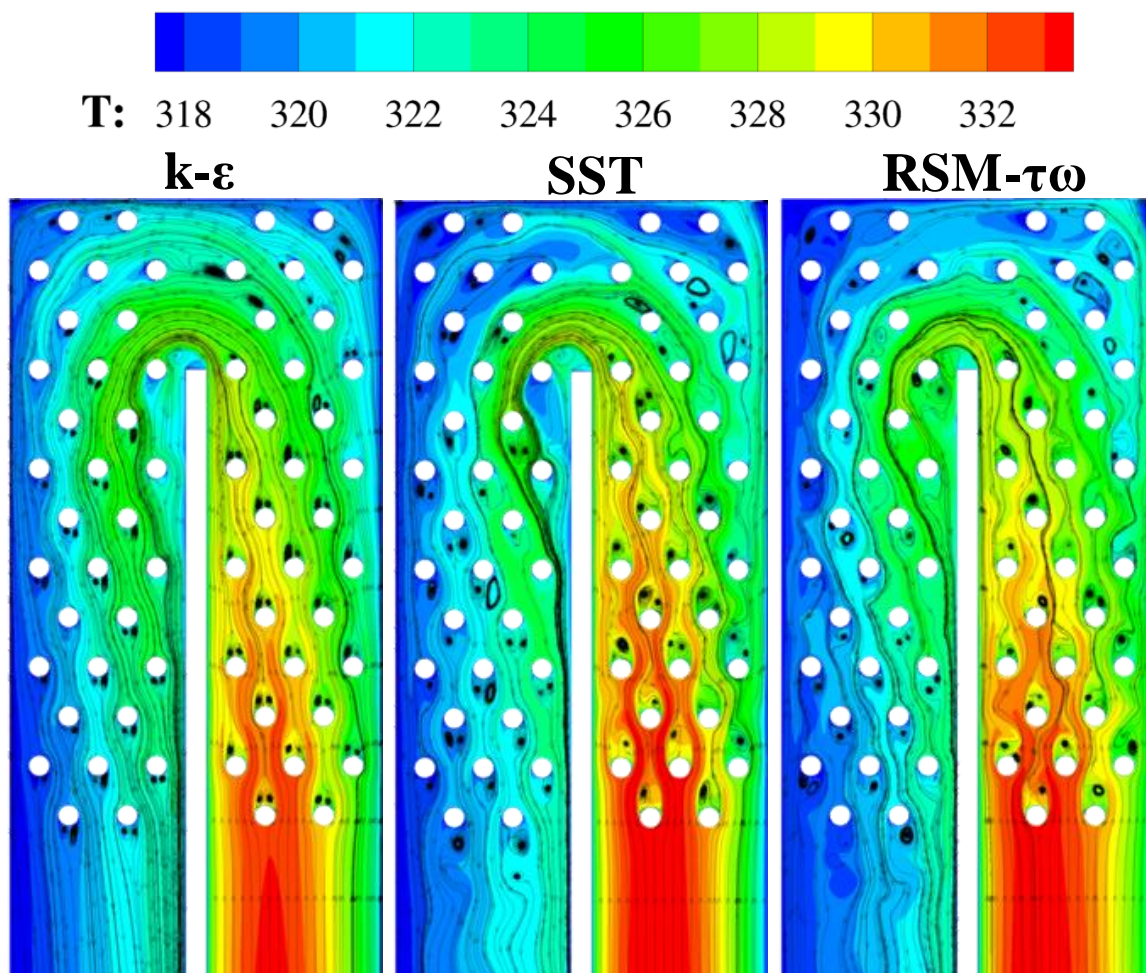
Figure 21. Streamlines in the symmetry plane colored by temperature for pin-finned U-duct.

2.6   Summary

Steady RANS were performed to examine four turbulence models – realizable k-ε, SST, RSM-LPS, and RSM-τω – on their ability to predict the flow and heat transfer in a U-duct with a trapezoidal cross section, where the walls are either smooth or lined with a staggered array of pin fins. The key findings are as follows.   For the smooth U-duct, all RANS models provided similar results in the up-leg duct. However, only RSM-τω and RSM-LPS could capture the pair of vortices in the corners because they can account for anisotropic effects of turbulence. But these vortices are relatively weak and disappear once the flow approaches the turn region. In the turn region and beyond, realizable k-ε and RSM-LPS yielded similar predictions because both of these models used the same one-equation model in the near-wall region. Similarly, SST and RSM-τω give similar results because both of these models used the ω-equation in the near-wall region. This showed the importance of the modelling in the near-wall region for the smooth U-duct. In the turn region, a jet-like flow impinges on the U-duct's tip, which enhances heat transfer on the tip wall as well as on the top and bottom walls. Around the bend in the down-leg, all models predicted a large separated region, which greatly reduced the heat transfer there but increased it in region outside of the separated region, where the flow is accelerated and where Dean-type secondary flows created in the turn region transported cooler fluid from the core of the U-duct to the walls. Based on the averaged HTC predicted, the SST model is preferred because of its accuracy and its ease of use.

For the pin-finned U-duct, all models gave similar results in up-leg. Also, all models predicted HTCs that are lower than measured values with k-ε giving the worst results and SST the best. All models examined provided lower HTCs because the pin fins induce unsteadiness, and this computational study is based on steady RANS. When there are pin fins, heat transfer was found to be highest on the leading edge of each pin fin where the flow impinges on it. On the top and bottom walls where pin fins are mounted, heat flux is highest in the region about the horseshoe vortex that wraps around each pin fin and lowest in the wake region. The pin fins behaved like guide vanes in the turn region. The pin fins reduced the size of the separation bubbles in the corners near the tip and around the bend. The pin fins transfer considerably more heat when compare to those on the top and bottom walls.

CHAPTER 3.   LES OF FLOW AND HEAT TRANSFER IN STRAIGHT DUCTS AND TRAPEZOIDAL U-DUCT

An earlier version of this chapter was published as 'Kenny S.-Y. Hu and Tom I-P. Shih, "Large-Eddy and RANS Simulations of and Heat Transfer in a U-Duct with a High Aspect Ratio Trapezoidal Cross Section," GT-2018-75535, Proceeding of ASME TurboExpo 2018, Turbomachinery Technical Conference & Exposition, June 2018, Oslo, Norway'.

3.1   Objective

The objective of this chapter is twofold.

The first is to generate a reliable LES data for a trapezoidal U-duct. The WALE subgrid-scale model was employed, and its inflow boundary condition was provided by a concurrent LES of incompressible fully-developed flow in a straight duct with the same cross section and flow conditions as the U-duct. The grid resolution required to obtain meaningful LES solution were obtained via a grid sensitivity study of incompressible fully-developed turbulent flow in a straight duct of square cross section, where data from DNS and experiments are available to validate and guide the simulation. The grid used is also examined by satisfying Celik's criterion, and resolving the Kolmogorov's -5/3 law.

The second is to use LES to understand how the turbulent flow affects heat transfer in a U-duct with a trapezoidal cross section. The data generated is also used to evaluate the capabilities of the RANS models used in CHAPTER 2 in predicting the details of the flow and heat transfer in this U-duct.

This chapter is organized as the follows: First, the three problems studied are described. Next, the governing equations for the LES models are given. Afterwards, the algorithms and mesh systems used for LES are presented. This is followed by the presentation of the results of this study. This chapter concludes with a summary of the key findings.

3.2   Problem Description

In the section, the U-duct problem studied is described. Also described are two other configurations connected to this study of the U-duct. The first is a straight duct of square cross section with numerical and experimental data that can be used to determine the required grid

resolution to get meaningful results. The second is a straight duct with the same cross section as the U-duct that is used to generate the boundary condition needed by LES at U-duct's inlet.

3.2.1 Straight Duct with Square Cross Section

Figure 22 shows a schematic of the straight duct with a square cross section used to determine the grid resolution needed by LES. The geometry and parameters were chosen to match the DNS study by Huser [19], Gavrilakis [20], and Joung [21], where the turbulent Reynolds number based on the friction velocity is $Re_\tau = 300$ & 600. To achieve these two turbulent Reynolds numbers, the following parameters were used: $D_h = 0.01$ m, $\nu = 7.55 \times 10^{-6}$ and 1.51×10^{-5} m^2/s, and $u_B = 7.79$ m/s & 15.58 m/s, which give rise to $u_\tau = 0.472$ & 0.913 m/s, respectively. The flow through this duct is assumed to be incompressible and fully developed so periodicity can be assumed. The length of this duct is $L = 6.4$ D_h. Since the length must be sufficiently long to capture all relevant length scales, it will be assessed.

3.2.2 Straight Duct with Trapezoidal Cross Section

Figure 23 shows a schematic of the straight duct with a trapezoidal cross section used to generate the inflow boundary condition for the LES of the U-duct. Thus, this duct must have the same trapezoidal cross section as the U-duct as well as the same flow and heat transfer conditions. The length of this duct is also $L = 6.4$ D_h, and its adequacy to capture all key length scales will be examined. Though all flow and heat transfer conditions of this duct is the same as U-duct (to be described), the upstream temperature of this duct is adjusted to be $T_{b,in} = 327.654$ K which match the temperature sought at the middle of the duct which will be explained in a later section.
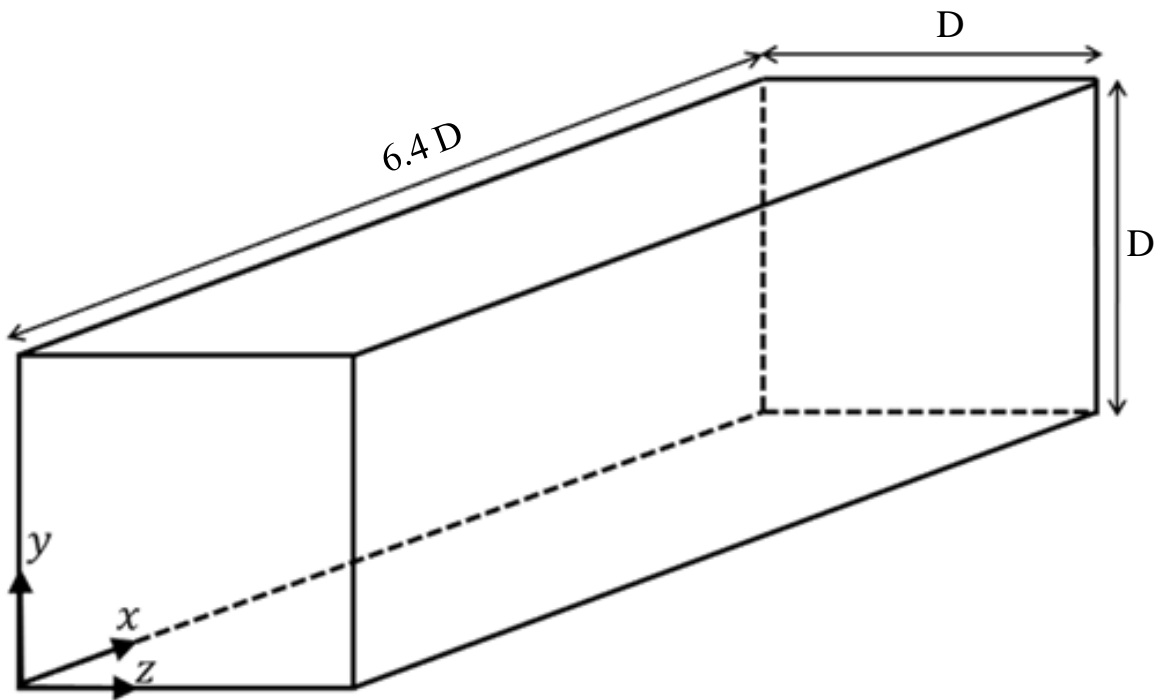
Figure 22. Schematic of straight duct with square cross section.

Unit: mm
$D_h = 29.04$
$W = 54.24$
$H_1 = 11.72$
$H_2 = 28.48$
$T_{b,in} = 327.654$
$T_w = 313.15$
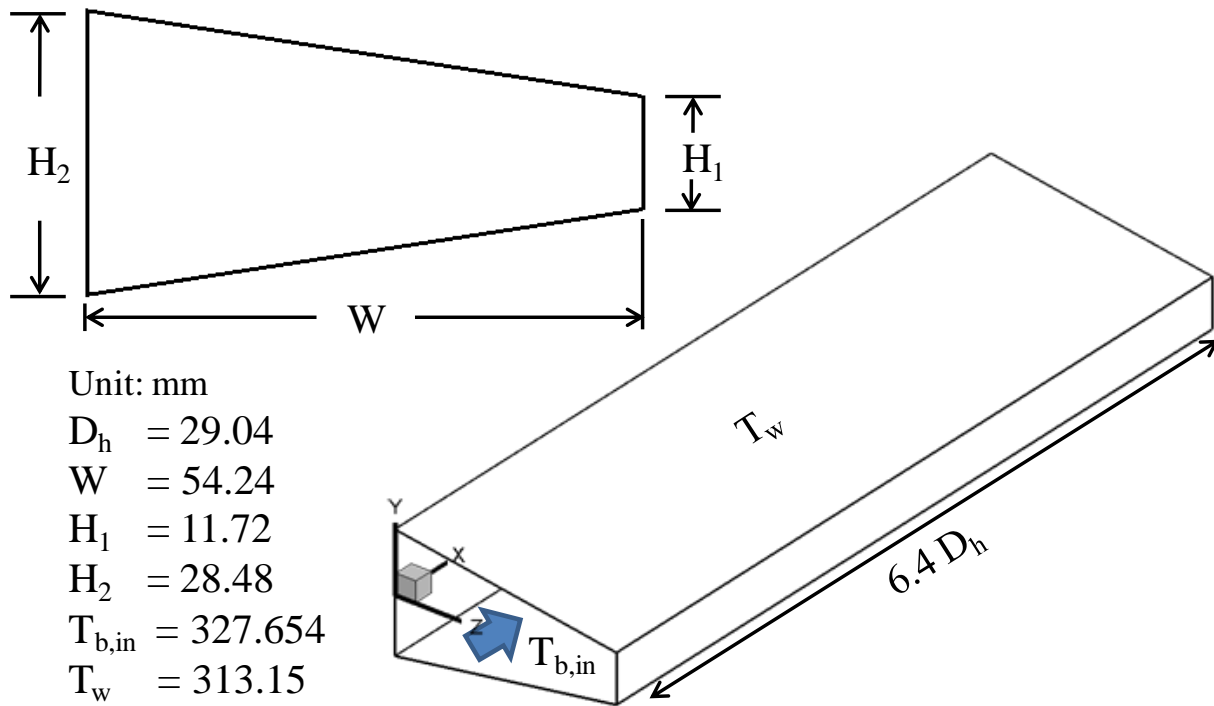
Figure 23. Schematic of straight duct with trapezoidal cross section.

3.2.3   U-Duct with Trapezoidal Cross Section

As mentioned in 2.2.1, Figure 2 shows a schematic of the U-duct studied. It has a trapezoidal cross section characterized by $H_1 = 11.72$ mm, $H_2 = 28.48$ mm, $W_1 = 54.24$ mm, $W_2 = 114.83$ mm, $L_1 = 246$ mm, $L_2 = 192$ mm, and $d = 6.35$ mm. The hydraulic diameter of this duct is $D_h = 29.04$ mm.

In the experimental study, this U-duct is fed by a long duct upstream of it so that the flow entering the U-duct is "fully" developed. To simulate the experimental study as closely as possible, the U-duct along with its upstream duct is modeled via two configurations as shown in Fig. 24. Figure 24(a) shows the configuration of the U-duct for simulations based on RANS. In this configuration, the upstream duct that is appended to the up-leg of the U-duct is modeled as a straight duct of length $40D_h$ with the same cross section as the U-duct so that the flow will be fully develop upon reaching the inlet of U-duct. To ensure that there is no reverse flow at the exit of the U-duct, another straight duct of length $L_E = 384$ mm with the same cross section as the U-duct was appended to the down-leg of the U-duct. For this U-duct with its appended ducts, air enters with uniform velocity $V_{in} = 12.65$ m/s and uniform temperature $T_{in} = 343.15$ K. All wall temperatures were maintained at $T_w = 313.15$ K, and the static pressure at the duct's exit is maintained at $P_{exit} = 1$ atm. This gives rise to a Reynolds number of 20,000 based on the U-duct's hydraulic radius and properties evaluated at $(T_w + T_{in})/2$. Figure 24(b) shows the configuration used for the LES. For this configuration, the up-leg portion of the U-duct was shortened by 96 mm to reduce computational cost. The inlet of the resulting U-duct is still sufficiently upstream of the bend to be relatively unaffected by the turn region. For LES, the boundary conditions imposed at the inlet is a challenge because it must contain all of the unsteadiness and scales associated with a fully-developed turbulent flow in the trapezoidal duct. One widely used approach is the vortex method. However, numerical experiments show that a very long duct needs to be appended to the up-leg of the U-duct to generate the turbulent structure of a fully-developed turbulent flow at the Reynolds number required, which adds considerable cost. In this study, the boundary condition at the inlet was provided by a concurrent LES of incompressible fully-developed flow in a relatively short straight duct with the same cross section and flow conditions as the U-duct (Fig. 23). For this straight duct, the temperature at its inlet is adjusted so that the bulk temperature at its middle is $T_{b,in} = 327.654$ K.

(a)RANS:


Unit: mm
D_h = 29.04
d = 6.35
L_1 = 246
L_2 = 192
L_3 = 96
W_1 = 54.24
W_2 = 114.83
H_1 = 11.72
H_2 = 28.48
L_i = $40D_h$
L_E = 384
L_A = $6.6\,D_h$

Re = **20,000**
V_{in} = 12.65 m/s
T_{in} = 343.15 K
T_{wall} = 313.15 K
P_{exit} = 101325 Pa
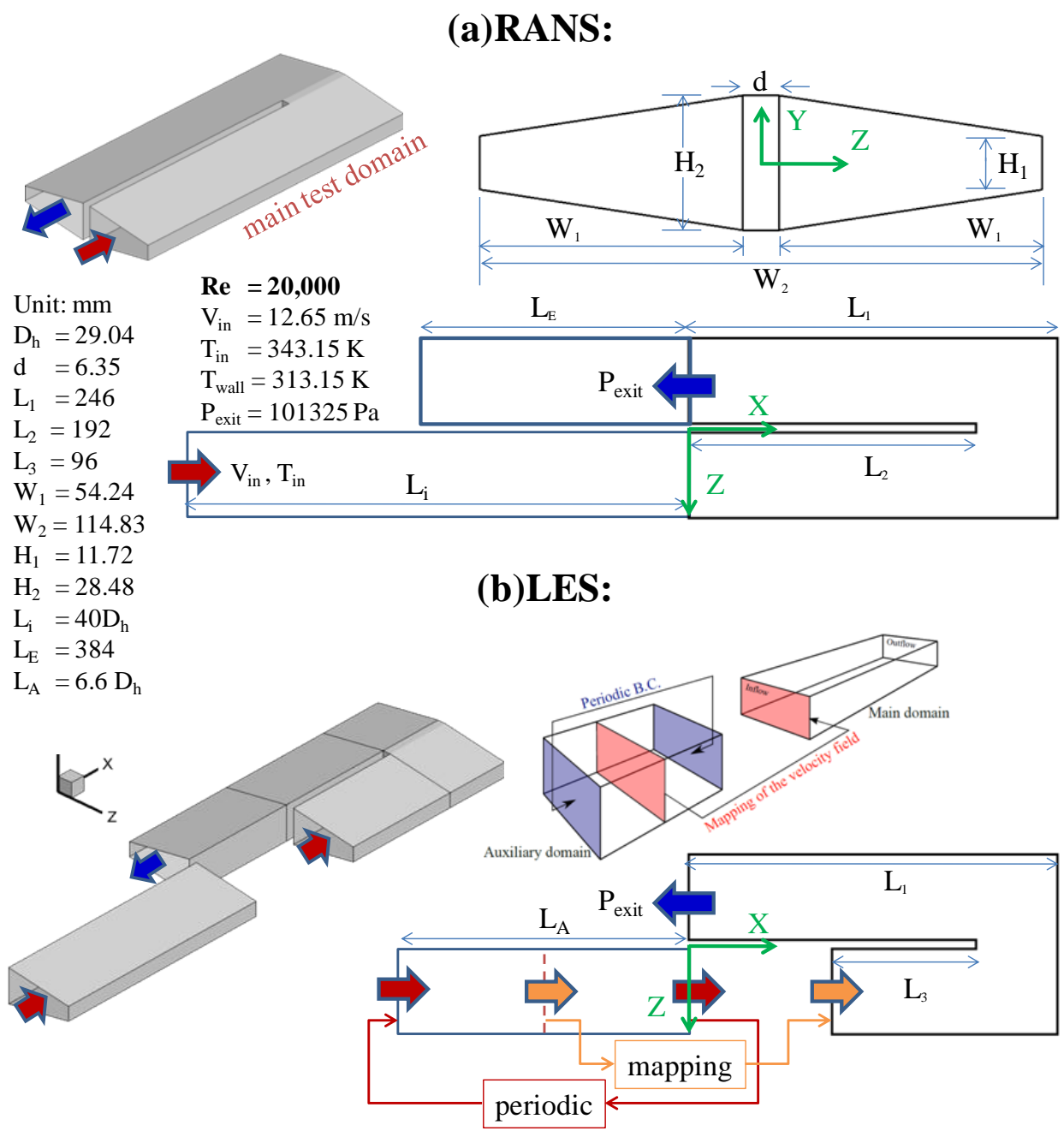
(b)LES:

Figure 24. U-duct studied: (a) RANS, (b) LES.

3.3   Formulations

For the U-duct and the two straight-duct configurations described in the previous section, the flow is assumed to be incompressible with constant properties, and viscous dissipation is neglected. These assumptions are acceptable because the Mach number is much less than 0.3, T_w–T_{in} is small, and the duct is not long so that the pressure drop is not significant. All thermodynamics and transport properties were evaluated at T= (T_{in}+T_w)/2.

3.3.1   Governing Equations for Large-Eddy Simulation

For the LES, large scales of the turbulent flow – which depend strongly on the geometry and boundary conditions imposed – are simulated, and the smaller scales – which have more universal properties – are modelled in terms of the resolved larger scales. This is accomplished by applying a spatial filter to the unsteady, three-dimensional form of continuity, momentum (incompressible Navier-Stokes), and thermal equations to yield:

$$\frac{\partial \hat{u}_j}{\partial x_j} = 0 \tag{13}$$

$$\frac{\partial \hat{u}_i}{\partial t} + \frac{\partial}{\partial x_j}\left(\hat{u}_i \hat{u}_j\right) = -\frac{1}{\rho}\frac{\partial \hat{p}}{\partial x_i} - \frac{\partial \tilde{\tau}_{ij}}{\partial x_j} + v\frac{\partial^2 \hat{u}_i}{\partial x_j \partial x_j} \tag{14}$$

$$\frac{\partial \hat{T}}{\partial t} + \frac{\partial \hat{u}_i \hat{T}}{\partial x_i} = \frac{k}{\rho C_p}\frac{\partial^2 \hat{T}}{\partial x_i^2} - \frac{\partial \widehat{u_i' T'}}{\partial x_i} \tag{15}$$

In the above equations, $\tilde{\tau}_{ij}$ is the subgrid-scale stress, and the hat represents a filtered variable. To close the filtered equation, $\tilde{\tau}_{ij}$ must be modeled, and the eddy viscosity model given below is used:

$$\tilde{\tau}_{ij} = -2v_{sgs}\hat{S}_{ij} + \frac{1}{3}\tilde{\tau}_{kk}\delta_{ij} \tag{16}$$

where ν_{sgs} is the sub-grid scale turbulent viscosity.

Many models have been proposed for ν_{sgs}. One model found to be particularly suited for wall-bounded flows is the Wall Adapting Local Eddy viscosity model (WALE) formulated by Nicoud and Ducros [42], and is given by

$$\nu_{sgs} = (C_w \Delta)^2 \frac{\left(S_{ij}^d S_{ij}^d\right)^{3/2}}{\left(\hat{S}_{ij}\hat{S}_{ij}\right)^{5/2} - \left(S_{ij}^d S_{ij}^d\right)^{5/4}} \tag{17}$$

where

$$S_{ij}^d = \hat{S}_{ik}\hat{S}_{kj} + \hat{\Omega}_{ik}\hat{\Omega}_{kj} - \frac{1}{3}\left(\hat{S}_{mn}\hat{S}_{mn} - \hat{\Omega}_{mn}\hat{\Omega}_{mn}\right)\delta_{ij} \tag{18}$$

$C_w = 0.325$ is a model constant, and Δ is the cutoff width. One strength of this model is that it does not require damping functions near the wall. It naturally goes to zero, and can reproduce the proper scaling at the wall of $\nu_{sgs} \sim y^3$ and is sensitive to both strain and rotation rate of the small structures. While this model should work well for this case, it is still necessary that the grid be fine enough to resolve the relevant turbulent scales. This is important because the resolved (filtered) velocities and pressure should represent the Reynolds stresses.

3.3.2 Eddy Diffusivity Hypothesis (EDH)

The discussion so far only addressed how the subgrid-scale stresses are modeled in the momentum equations. In the energy equation, the correlation between velocity and temperature fluctuations, $\overline{u_i'T'}$, also needs to be modelled. In this study, that correlation is modeled by using the eddy-diffusivity concept given by

$$\overline{u_i'T'} = -\Gamma_t \frac{\partial T}{\partial x_i} \tag{19}$$

In the above equation, the bar denotes spatially filtered operation in LES, and Γ_t is the eddy-diffusivity of heat. Reynolds analogy between heat and momentum transport suggests that Γ_t is closely related to the subgrid-scale viscosity μ_t so that

$$\Gamma_t = \frac{\mu_t}{Pr_t} \tag{20}$$

where Pr_t is the turbulent Prandtl number. In this study, Pr_t is taken to be 0.85 for LES.

3.4   Numerical Method

Version 16.2.0 of the Fluent UNS code [39] was used to generate all solutions. For all simulations, absolute velocity formulation and pressure-based SIMPLE algorithm were used as the solver.

For RANS simulations, the fluxes for momentum, turbulence quantities, and energy at the cell faces are interpolated by using the second-order upwind scheme, and pressure is computed by using second-order accuracy. The scaled residual is always less than 10^{-5} for the three components of the velocity, less than 10^{-7} for the energy equation, less than 10^{-4} for turbulent quantities, and less than 10^{-3} for the continuity equation. Iterations were continued until all residuals for all equations plateau to ensure convergence to steady-state has been reached.

For LES, the momentum fluxes are computed by using second-order central differencing, and pressure interpolation employs the pressure-staggering option (PRESTO) scheme. The choice of PRESTO and central over bounded central was guided by Lampitella [43]. His study showed the excellent turbulence and energy spectra characteristics of those schemes for LES of 2-D channel flow. The time derivatives are approximated by the bounded second-order implicit scheme. The time step was chosen based on CFL ≤ 1 with ten sub-iterations per time step, which was found to be sufficient for the flow field to converge at each time step.

3.4.1   Grid System of LES of "Square" Straight Duct

Figure 25 and 26 show the four grids used for the LES of the straight duct with square cross section. Two types of grid structures were examined: O-grid and H-grids with similar

resolution in the wall normal direction but differ in their growth ratios as well as resolutions along the perimeter of the wall. The spacings between grid points along the walls are $x^+ = 40$, $y^+ = 0.6$, and $15 < z^+ < 40$ for coarse-O grid, $x^+ = 30$, $y^+ = 0.6$, and $1 < z^+ < 20$ for coarse-H grid, $x^+ = 30$, $y^+ = 0.6$, and $8 < z^+ < 15$ for fine-O grid, $x^+ = 25$, $y^+ = 0.6$, and $1 < z^+ < 15$ for fine-H grid. The coarse-O grid has 618,640 cells, the coarse-H grid has 2,109,989 cells, the fine-O grid has 2,440,620 cells, and the fine-H grid has 4,241,884 cells.

As shown later in this paper, results obtained on these grids show the coarse-H and fine-O grids to generate solutions that agree better with the DNS results from Gavrilakis [20] and Joung [21]. However, since O-grid has a smaller variation in the cell spacings, and cell spacings are used as the filter width in LES, the O-grid with wall wrapped-around O-grid is used for the trapezoidal straight and U-ducts.

3.4.2   Grid System of Trapezoidal Straight Duct for LES

Based on the findings from the LES of the "square" straight duct, the grid system used for LES of the trapezoidal straight duct also uses the O grid structure with similar distribution of grid points as shown in Fig. 27. The total number of cells is 2,452,500, which is similar to the square duct case that was obtained by a grid-sensitivity study.

3.4.3   Grid System of Trapezoidal U-Duct for LES

Figure 28 shows the two kinds of grids used for the U-duct with trapezoidal cross section, one with a partial O-grid where a part of the U-duct wall is not wrapped and another with a full O-grid. Figure 28 also shows the velocity magnitude and temperature in the middle plane, and the heat transfer on the wall obtained by using these two types of grids. From this figure, it can be seen that although velocity and temperature in the middle plane are not affected by the difference in the grids, heat transfer on the wall is strongly affected. This is because heat transfer is calculated by the gradient of temperature, and so it is important to keep the grid spacing next to walls fine enough to ensure the accuracy of heat transfer calculation. Figure 29 shows the details of the mesh of the trapezoidal U-duct for both RANS and LES, and both has grids clustered next to all walls via a wrap-around O-type of the grid.
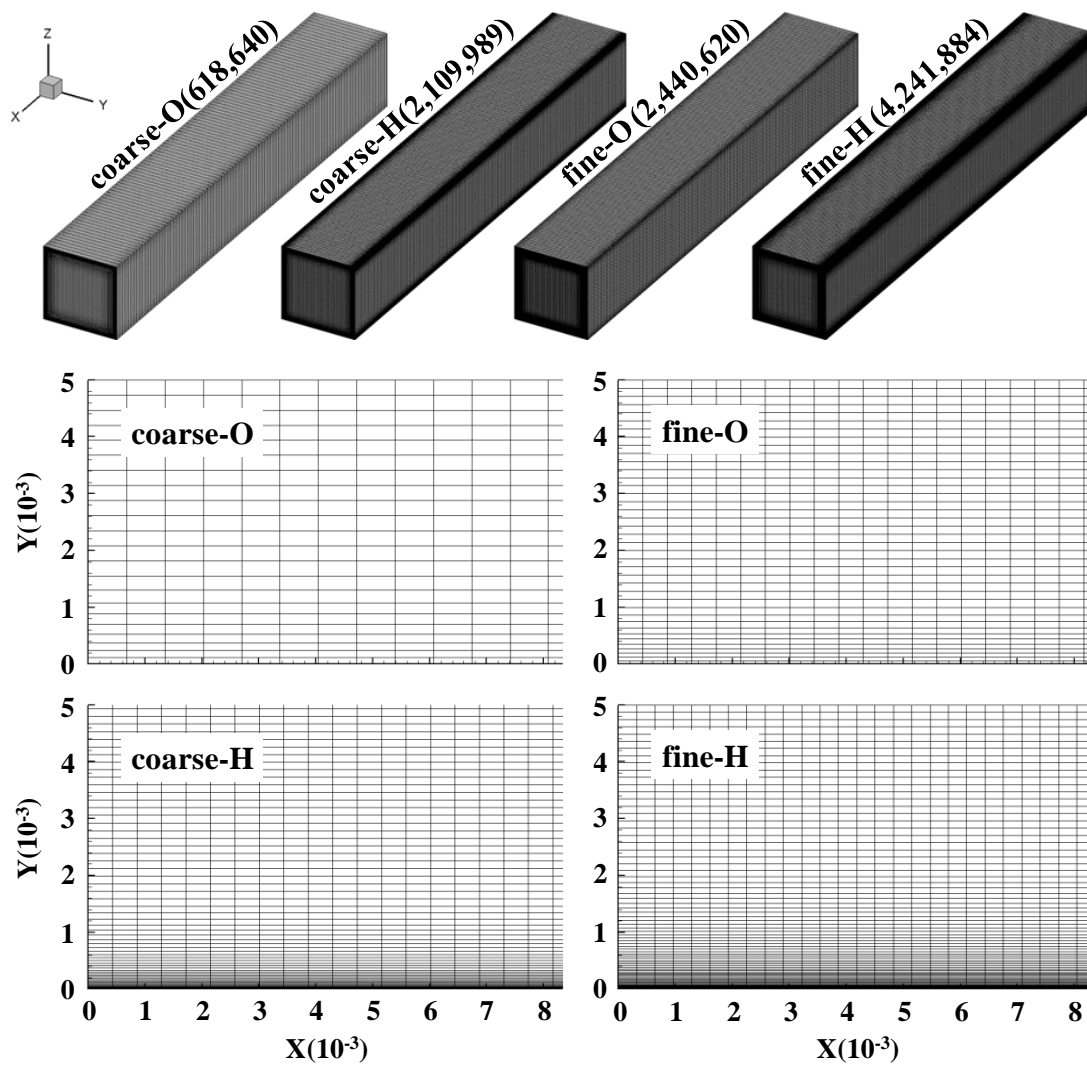
Figure 25. Grid used in x-z plane for LES of "square" duct.
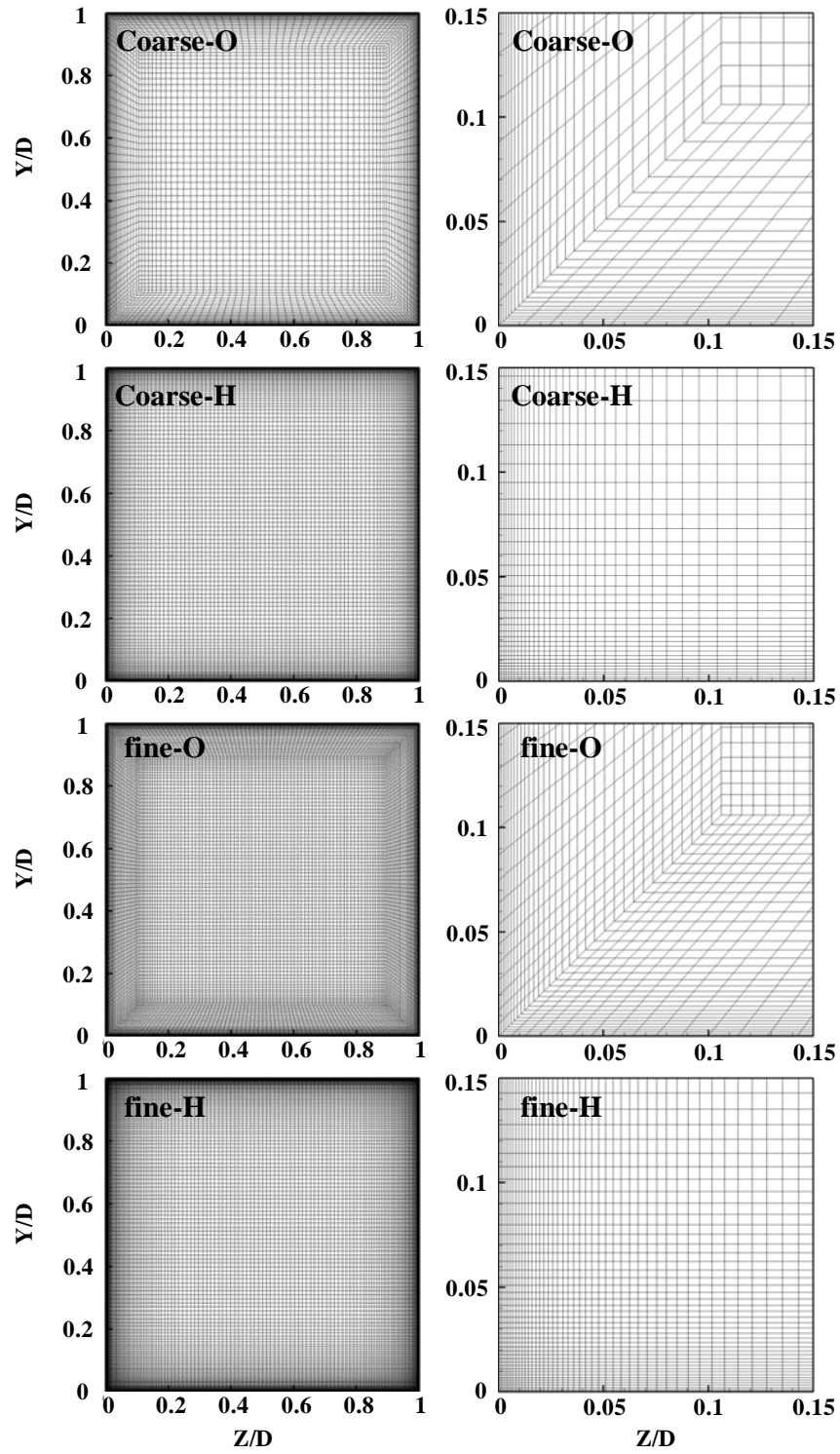
Figure 26. Grid used in y-z plane for LES of "square" duct.

2,452,500 cells
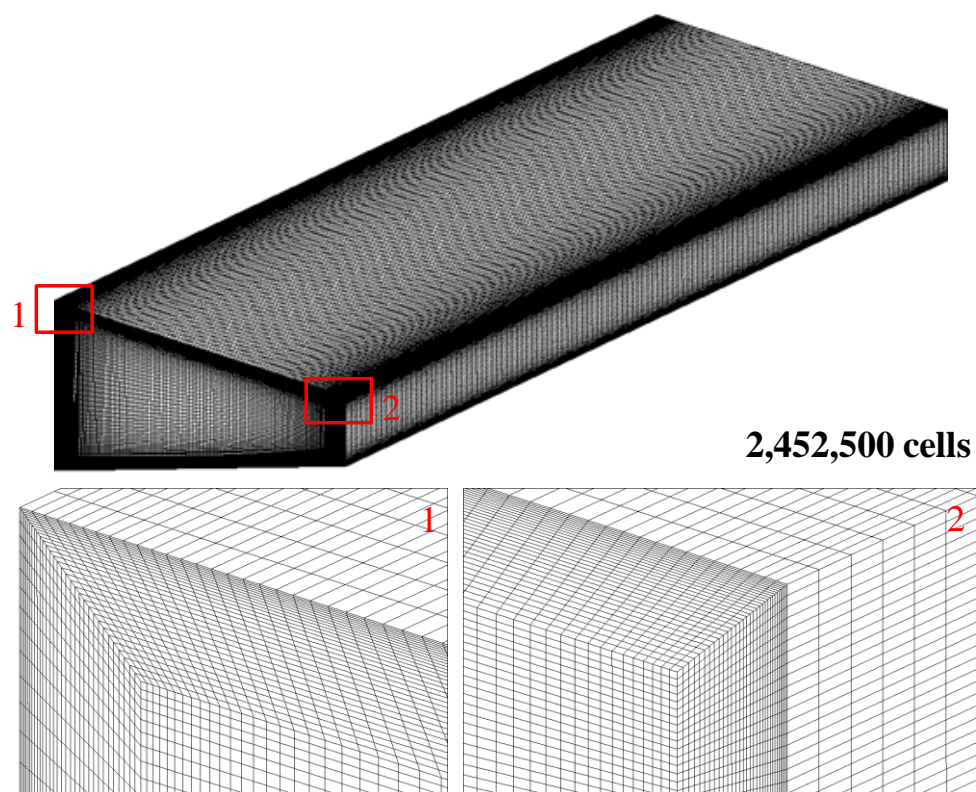
Figure 27. Grid system for LES of straight trapezoidal duct.
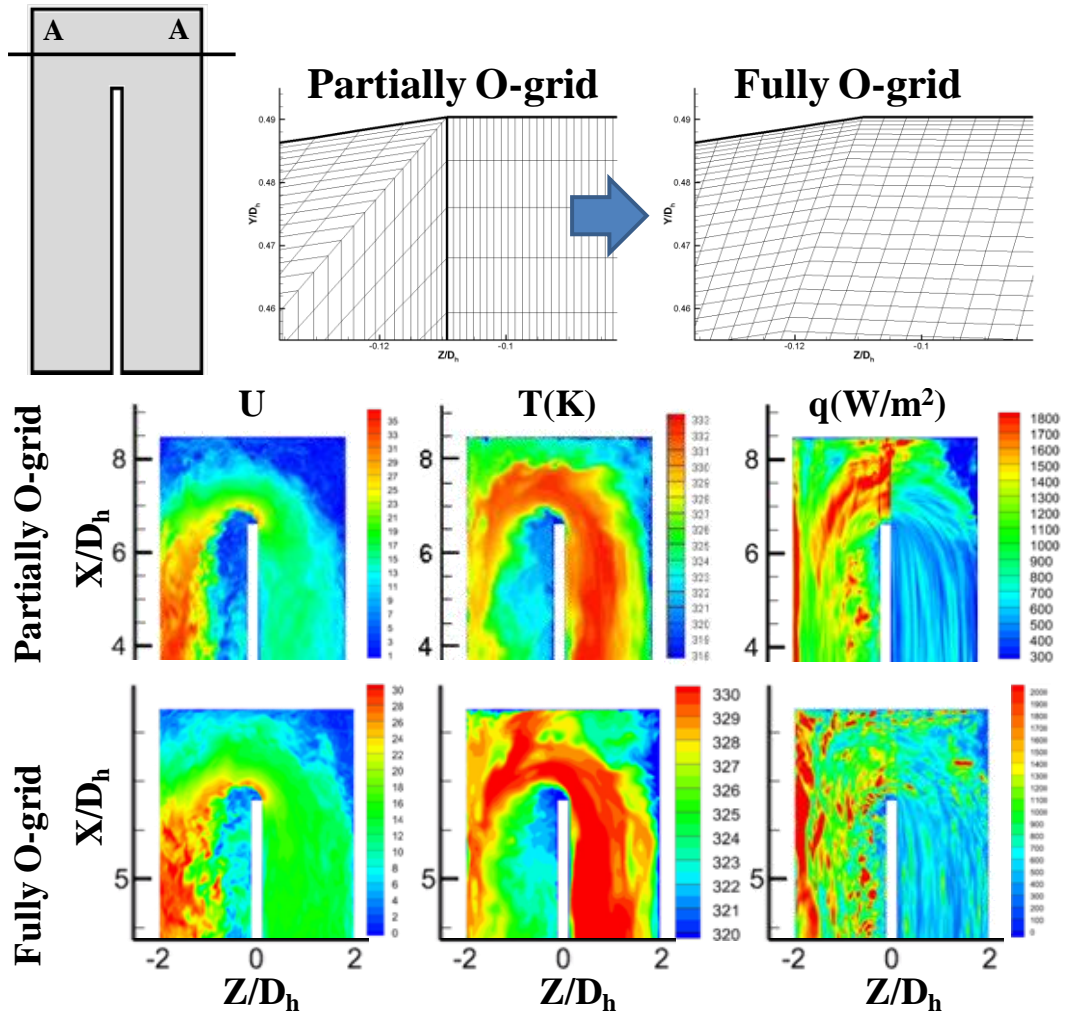
Figure 28. Partial O-grid vs. Full O-grid: the velocity magnitude (U) and the temperature (T) on the symmetry plane, and the heat flux (q) on the wall.

RANS

O-grid wrap around INNER wall

4,129,920 cells
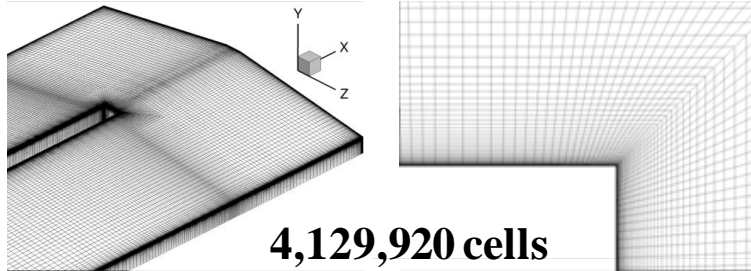
LES

O-grid wrap around ALL the walls

16,110,000 cells
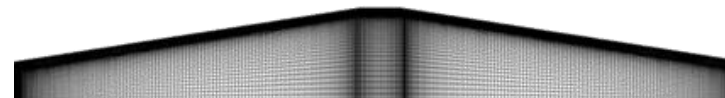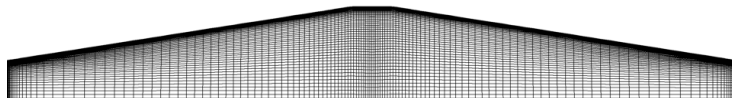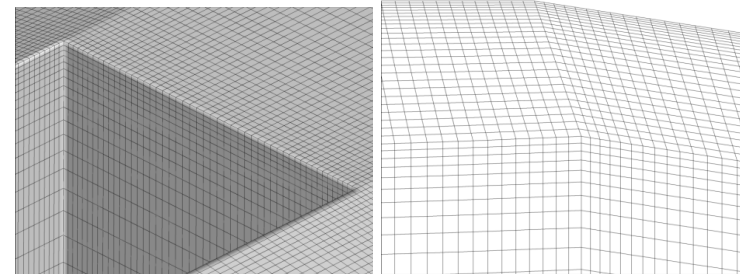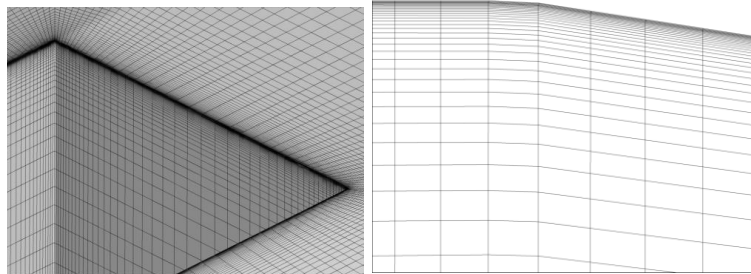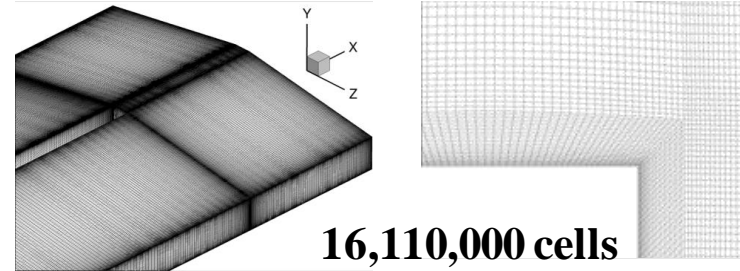
Figure 29. Grid systems for U-duct problem: LES vs. RANS.

3.5   Results

        In this section, results of the grid-sensitivity study for the LES are first presented. Then,
the experimental method used to obtain the heat-transfer coefficient to validate this
computational study is outlined. Afterwards results obtained for the U-duct by LES and RANS
are described.

3.5.1   Verification & Validation: LES of Square Straight Duct

        To ensure that the grid is fine enough, LES solutions were obtained to assess the
dissipation characteristics through the 1-D energy spectra. Figure 30 shows the energy spectrum
obtained by the following equation:

$$E(k) = \ C_1 \varepsilon^{2/3} k^{-5/3} \tag{21}$$

        From this figure, it can be seen that the energy spectrum to follow Kolmogorov's -5/3
law for a range of wave numbers before falling steeply. There is a small buildup of energy at the
small scales, but since this occurs after the energy drops seven orders of magnitude, the baseline
grid is deemed acceptable. The smallest wavelength (largest wave number) resolved in this
study is marked with a solid line. As a further examination on the adequacy of the grid
resolution, a method proposed by Celik et al. [44] was used. In this method, adequacy of the grid
is assessed by an indicator based on the eddy viscosity ratio at the subgrid scale given by

$$LES\_IQ = \frac{1}{1 + 0.05\left(\frac{\upsilon_{t,eff}}{\upsilon}\right)^{0.53}} \tag{22}$$

where $\upsilon_{t,eff}$ denotes the effective subgrid viscosity and υ denotes the laminar viscosity. Celik et
al. proposes that the value of LES_IQ should be greater than 0.8 for good LES predictions. In
other words, the subgrid viscosity must be sufficiently small when compared to the laminar
viscosity in order to ignore the fluctuations in the subscales. Figure 31 showed the results
obtained from equation (22). From this figure, the LES quality indexes for all four grids used are

greater than 0.9 everywhere in the square duct. Therefore, all the grids used in this study satisfy the Celik criterion.

To examine if the duct with length 6.4D_h is long enough, it is necessary to ensure that velocities are uncorrelated over that distance. Figure 32 shows the longitudinal two-point correlation calculated by the following equation:

$$R_{uu} = \frac{\overline{u'(0,t)u'(X/D,t)}}{\overline{u'^2(0,t)}} \tag{23}$$

For fully developed flow in the square straight duct, the Taylor's "frozen turbulence" hypothesis [45] was employed to compute the two-point correlation in eq. (23). In Taylor's hypothesis, the turbulent eddies are assumed to be frozen as they advect past a fixed point and thus the local change within each eddy is negligible. This assumption works well as long as the local turbulence intensity is less than $10 - 20\%$ [46]. Invoking this hypothesis for this problem is acceptable because the turbulence intensity is only 3% at the channel center (z/D = 0.51), and only 7% near the wall (z/D = 0.055).

From this figure, the velocities about the channel center (z/D =0.51) can be seen to be correlated up to x/D = 1. Near the wall (z/D = 0.055), the correlation can extend to about x/D = 3. Thus, a duct length of 6.4D is should be sufficiently long for the conditions of this study.
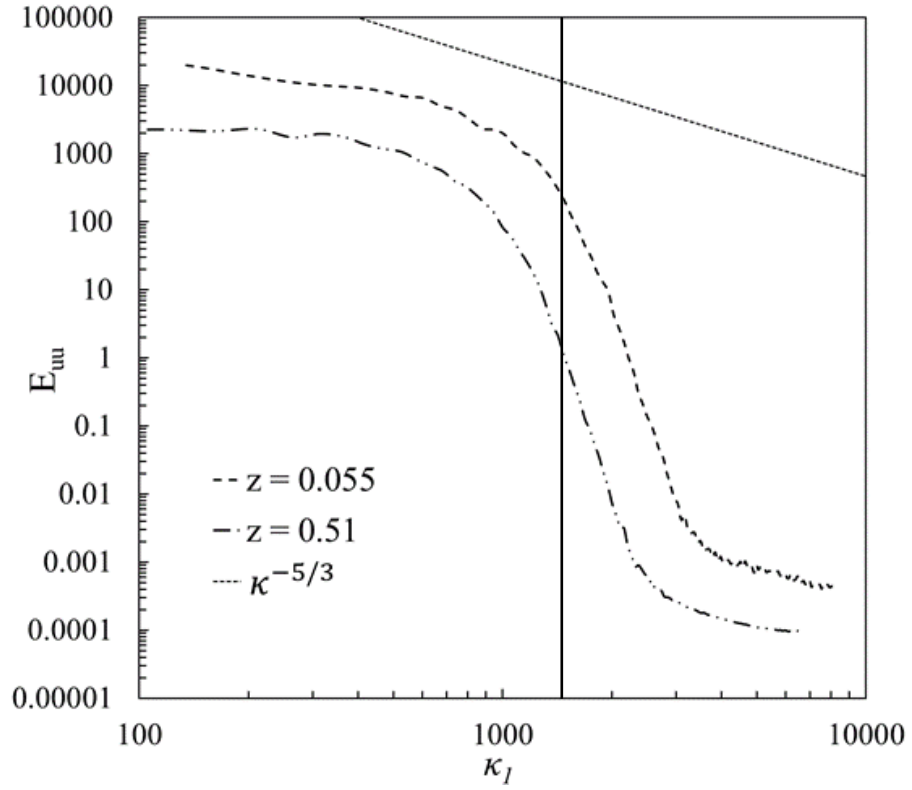
Figure 30. The energy spectra (κ_l denotes the wavenumber) obtained from LES of straight duct with square cross section on baseline grid at y/D = 0.5.
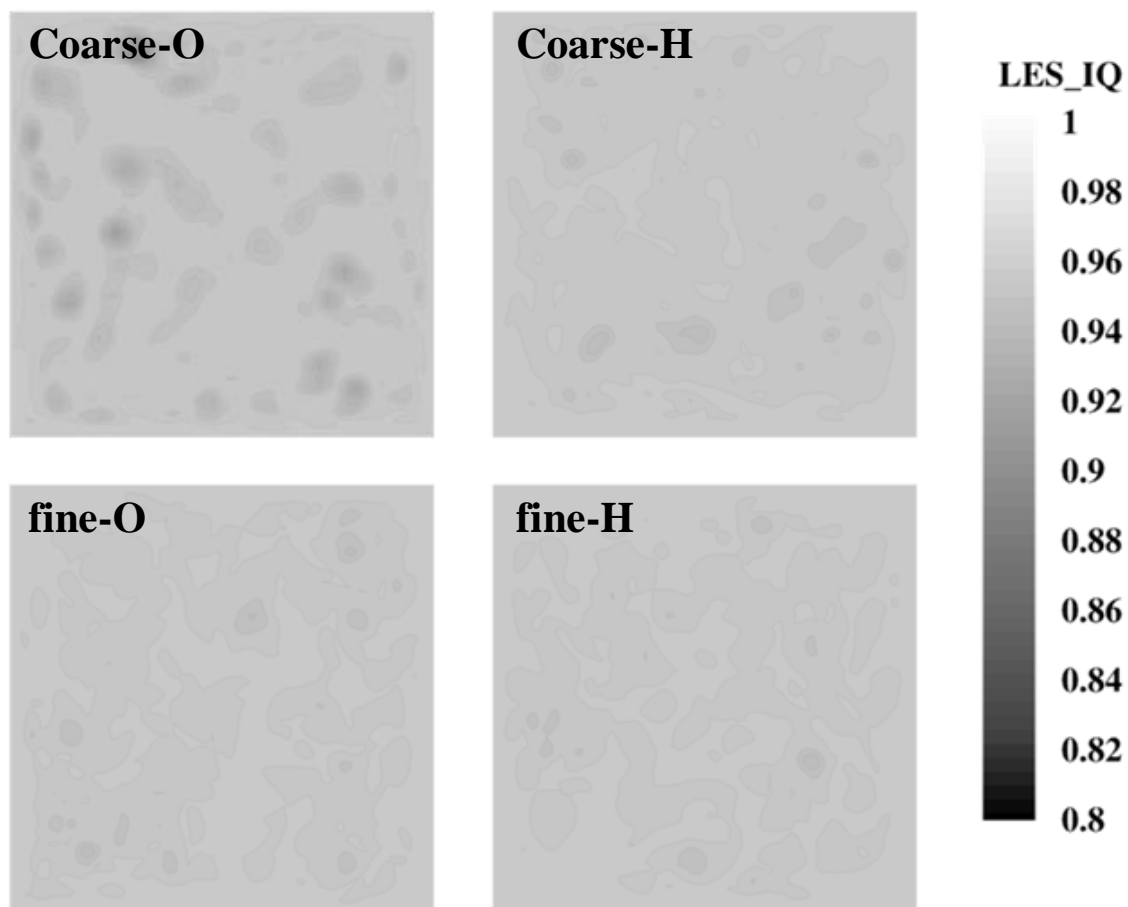
Figure 31. The Celik criterion obtained from LES of straight duct with square cross section.
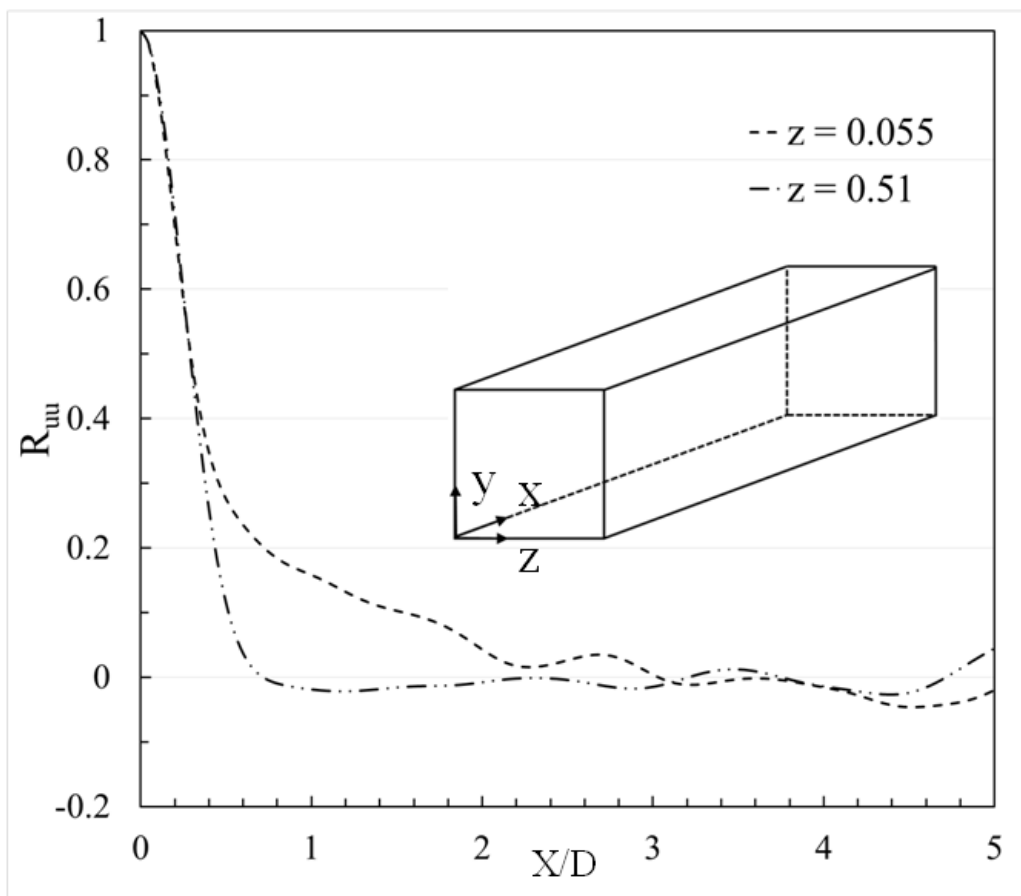
Figure 32. The longitudinal two-point correlation obtained from LES of straight duct with square cross section on baseline grid at y/D = 0.5.

A comparison of square straight duct turbulent flow with turbulent Reynolds number of $Re_\tau = 300$, based on wall shear stress, for four meshes mentioned before is shown in Fig. 33. In this figure, it can be seen that none of the DNS or LES data are able to match the experimental data [47-51]. When comparing DNS and LES data, the two DNS data provided similar results, and LES data obtained on the coarse-H and fine-O grid show better agreement to DNS. Between coarse-H and fine-O, a further comparison of turbulence quantities is shown in Fig. 34. LES on the fine-O grid is able to predict the experiment data on u_{rms}/u_τ better than results from coarse-H. For v_{rms}/u_τ, the DNS data from Joung has a constant value between z/D = 0.05~0.15. In this range, the experimental data from Niederschults, DNS data from Gavrilakis and Huser, and LES results from fine-O showed an increasing trend. LES results from coarse meshes showed a decreasing trend. LES results from fine-H showed a slightly decreasing trend. Hence, the grid resolution and the configuration of fine-O grid, including grid spacing on the walls and the growth ratio, are used to determine the grid for trapezoidal ducts.

3.5.2 Verification: LES of Trapezoidal Straight Duct

Figure 35 shows the energy spectrum acquired from six probes in the trapezoidal straight duct. The energy density associated with the high wavenumber is at least five orders lower than the energy density corresponding to low wavenumbers in the inertial sub-range. Thus, the grid resolution is adequate for this duct. The results also show that the velocity at the two ends of the duct's periodic sections (i.e., x = 0 and x = L) are not correlated. Thus, the length, L = 6.4 D_h, is sufficiently long to implement periodic boundary conditions for the incompressible fully developed turbulent flow.

In Fig. 36, the longitudinal two-point correlations acquired from six probes show that they fall off to zero values less than half of the duct length(it is necessary because the domain has a periodic boundary condition along the stream-wise direction), which means the velocities are uncorrelated over this distance, indicating that the length of the computational domain is sufficient.
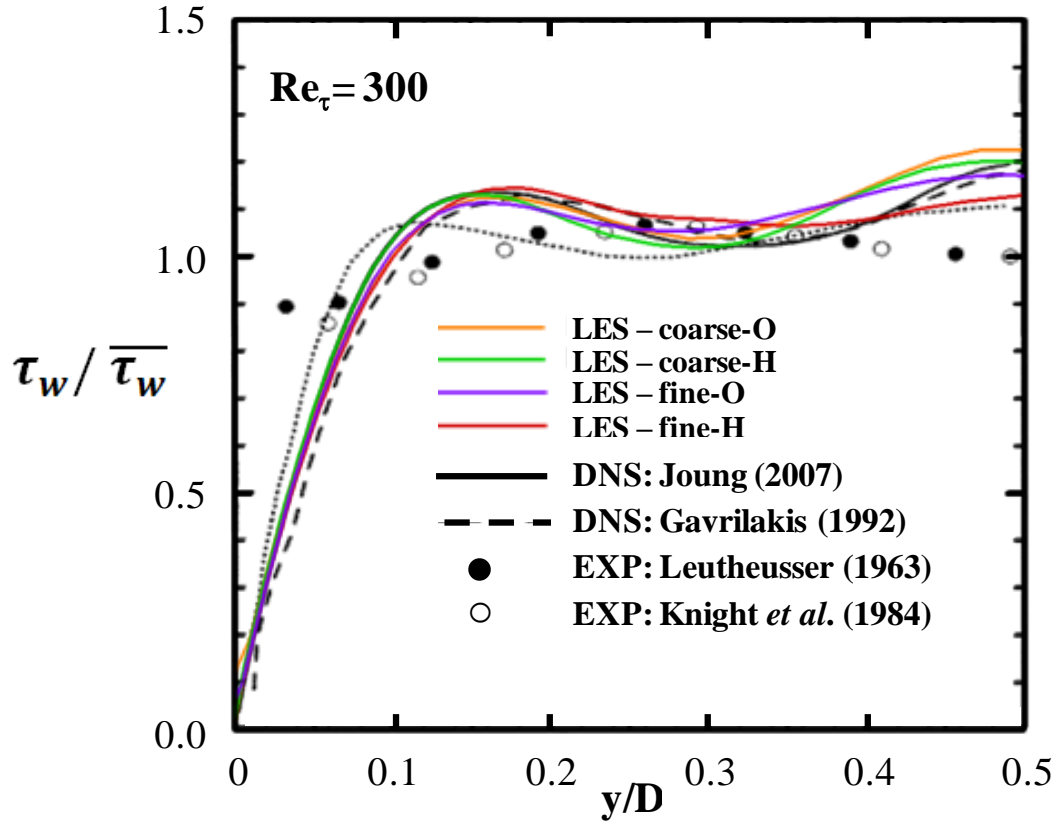
Figure 33. LES of square straight duct: wall shear stress, normalized by the area-weighted averaged values.
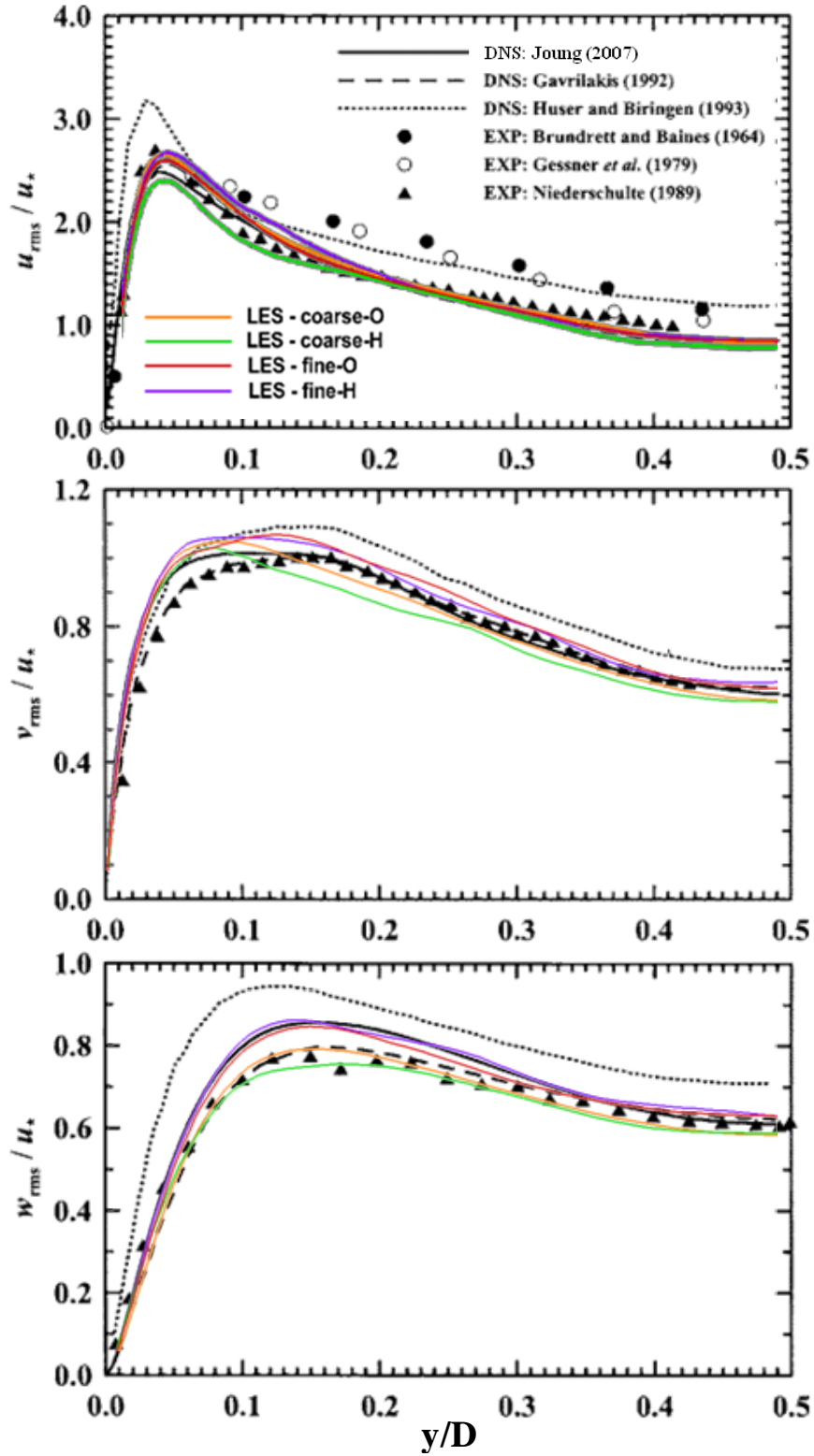
Figure 34. LES: root mean square of the u, v, and w normalized by the area-weighted averaged friction velocity.
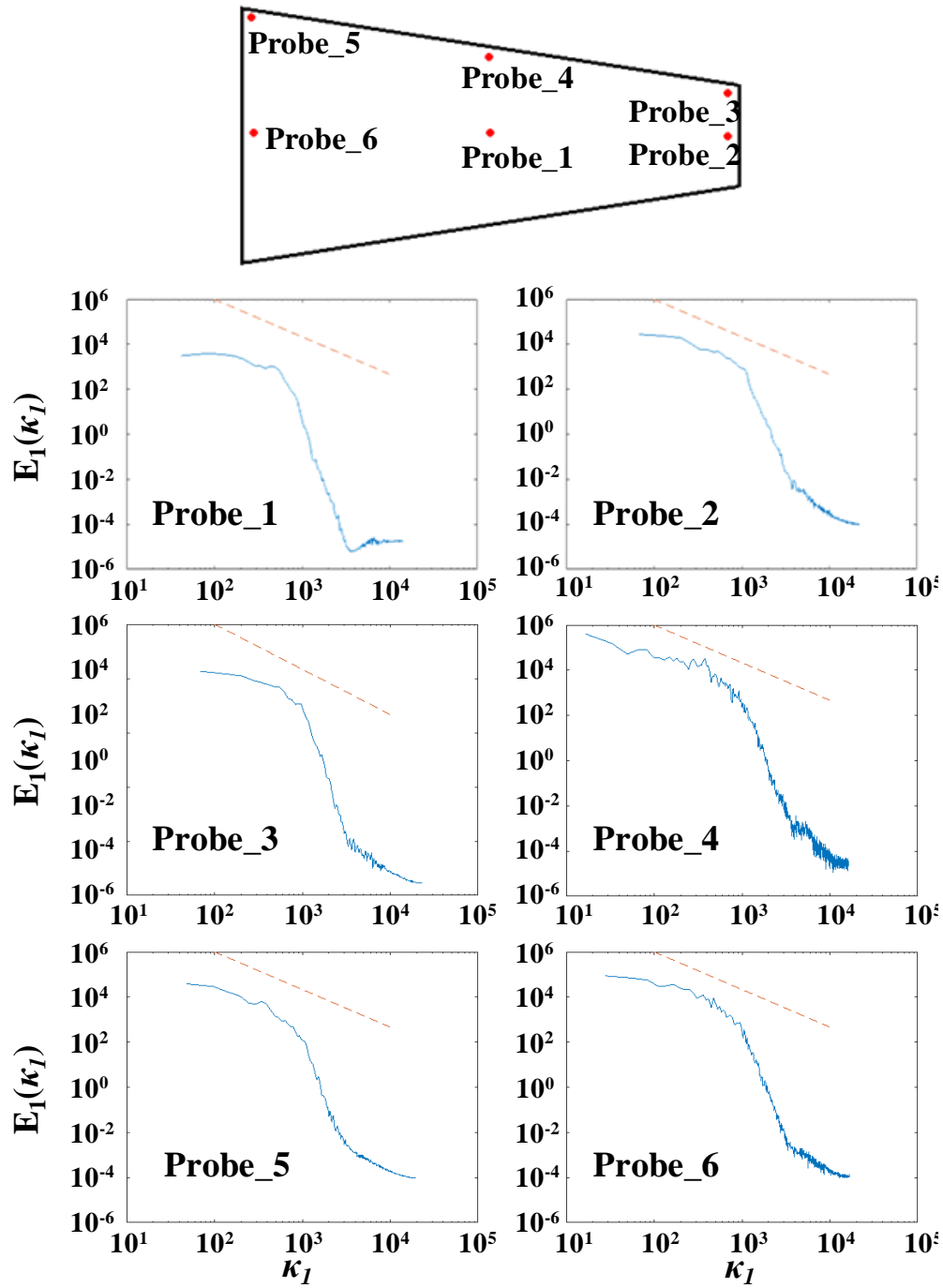
Figure 35. Verification of LES (trapezoidal straight duct): energy spectrum on six probes located at the middle of the straight duct. Probe_1 is at the center of the duct. All other probes are 1 mm away from the walls.
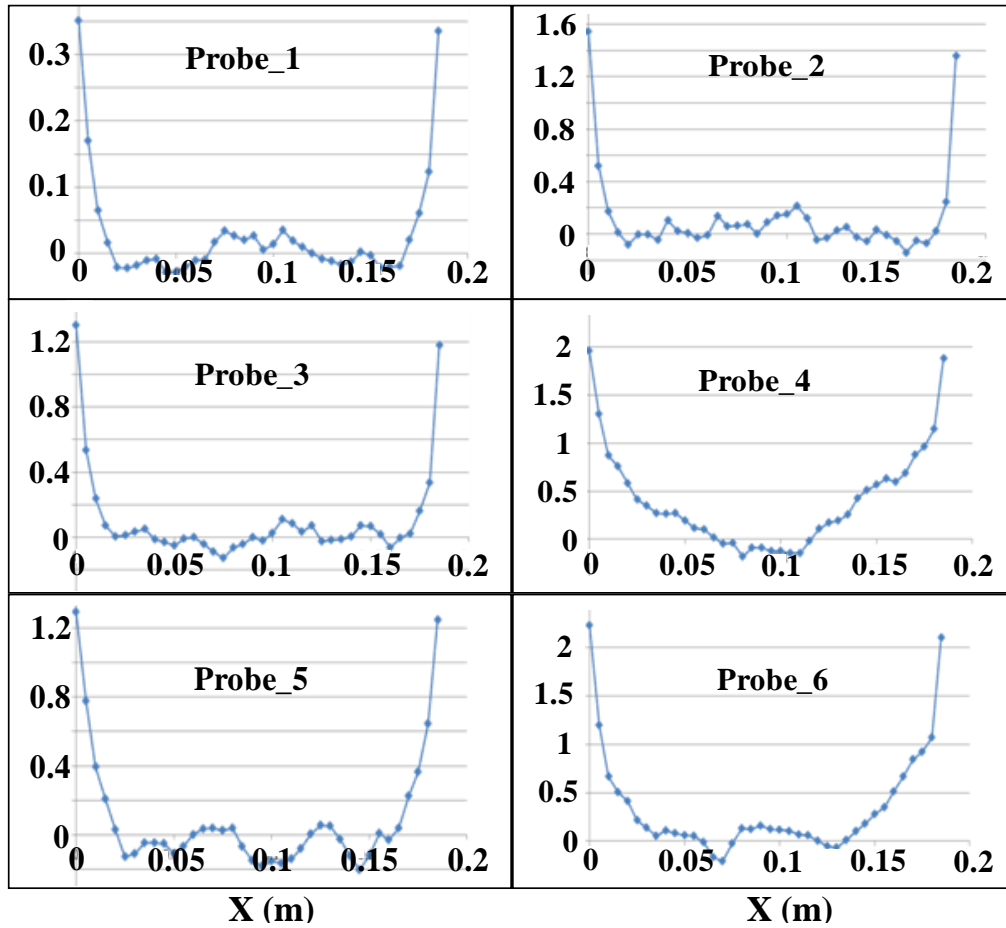
Figure 36. LES of trapezoidal straight duct: longitudinal two-point correlations on the six probes shown in Figure 35.

3.5.3   Results for Trapezoidal U-Duct

In this section, the heat transfer coefficients obtained for the trapezoidal U-duct by the RANS models (2.5.3) and by LES (this chapter) are compared with the experimental measurements (2.5.2). The CPU time is 300,000 core hours to obtain the reasonable averaged LES results. It required 1.69 GB of memory for the case and about 20 GB depends on the data needed for further budget terms analyses for LES. For RANS simulations, the CPU time is around 300 and 450 hours for eddy-viscosity models and Reynolds Stress models. The memory requirements are 1.2 GB for eddy-viscosity models and 1.45 GB for Reynolds Stress models.

3.5.3.1   Heat Transfer

Figure 37 shows the heat transfer coefficient obtained by RANS, LES, and experimental measurements (EXP). From Fig. 37, the following observations can be made:

A.   All RANS models predict a region of low HTC around the bend in the down-leg of the U-duct. This is because all RANS models predicted a large separated region around the bend that starts at the tip of the wall that separates the up-leg and the down-leg of the U-duct. Such a low region of HTC was not observed in the experimental measurements (EXP). LES, however, was able to predict the experimentally measured HTC correctly by showing the separation at the tip of the separator to be unsteady with the separation bubble shedding constantly.

B.   Because of incorrectly predicting the large separated region around the bend so that the flow around the separated region is greatly accelerated, all RANS models over predicted the HTC next to the outer wall in the down-leg of the U-duct, whereas LES slightly under predicts HTC in that region.

C.   All RANS models over predict the upstream influence of the turn region on the HTC in the up-leg, whereas LES predicts slightly lower HTC in the up-leg.

D.   LES and all RANS models except $k\text{-}\varepsilon$ correctly predict a region of high HTC next to the tip of the U-duct. This increased HTC in that region is caused by jet impingement of the cooling fluid on the tip wall of the U-duct. From this figure, it can be seen that SST and RSM over-predict the magnitude of the HTC and LES slightly under predicts that magnitude.

E.   Only LES is able to predict the HTC contours that match the experimentally measured ones (EXP). This is especially evident in the HTC predicted in the turn region and in the down-leg of the U-duct.

Once this physical phenomenon was understood, unsteady RANS (URANS) was performed where perturbations were introduced at and about the separator tip to induce unsteadiness. In all cases, once the perturbations were no longer applied, unsteady separation could not be sustained by URANS, and the flow becomes steady and identical to those predicted by steady RANS. Thus, the unsteady separations that occur at the tip of the separator is induced by unsteadiness in the turbulent flow field and not by asymmetry in geometry or boundary conditions such as the unsteady separations that take place for flows past blunt objects such as cylinders and cubes.

Figure 38 shows a more quantitative comparison of the predicted HTC with measure values at several X/L_1 locations, where the HTC is normalized by the maximum value on the walls. At locations upstream of $X/L_1=0.65$ in the up-leg, only LES can match more closely experimentally measured values, while all RANS models predict a parabolic-like curve with its peak closer to the inner wall. In the turn region, the mixing dilutes the difference between RANS and LES results, but LES still predicted better. The biggest difference between RANS and LES occurs in the down-leg because all RANS models predicted a large separated region after the bend. Locally, RANS under predicts from 50% to 80% of the experimentally measured values. Though none of the RANS model was able to predict the HTC distributions, the results from CHAPTER 2 showed the SST and RSM models to predict averaged HTC reasonably well. Thus, if only averages are needed, then SST and RSM may be adequate.

Here, it is noted that in CHAPTER 2, it is found that RANS based on SST and RSM to give reasonably accurate predictions of the HTC if the HTC was averaged. This shows that RANS based on SST and RSM may be adequate if only regionally-averaged HTC are of interest. However, if detailed distributions of the HTC are needed (e.g., to understand thermal stress distribution), then LES is needed, and RANS based on SST and RSM are inadequate for this U-duct with a trapezoidal cross section. In addition, LES was able to show why RANS was unable to predict the HTC correctly in the down-leg because it could not predict unsteady separation. Thus, LES shows its usefulness for this U-duct problem.
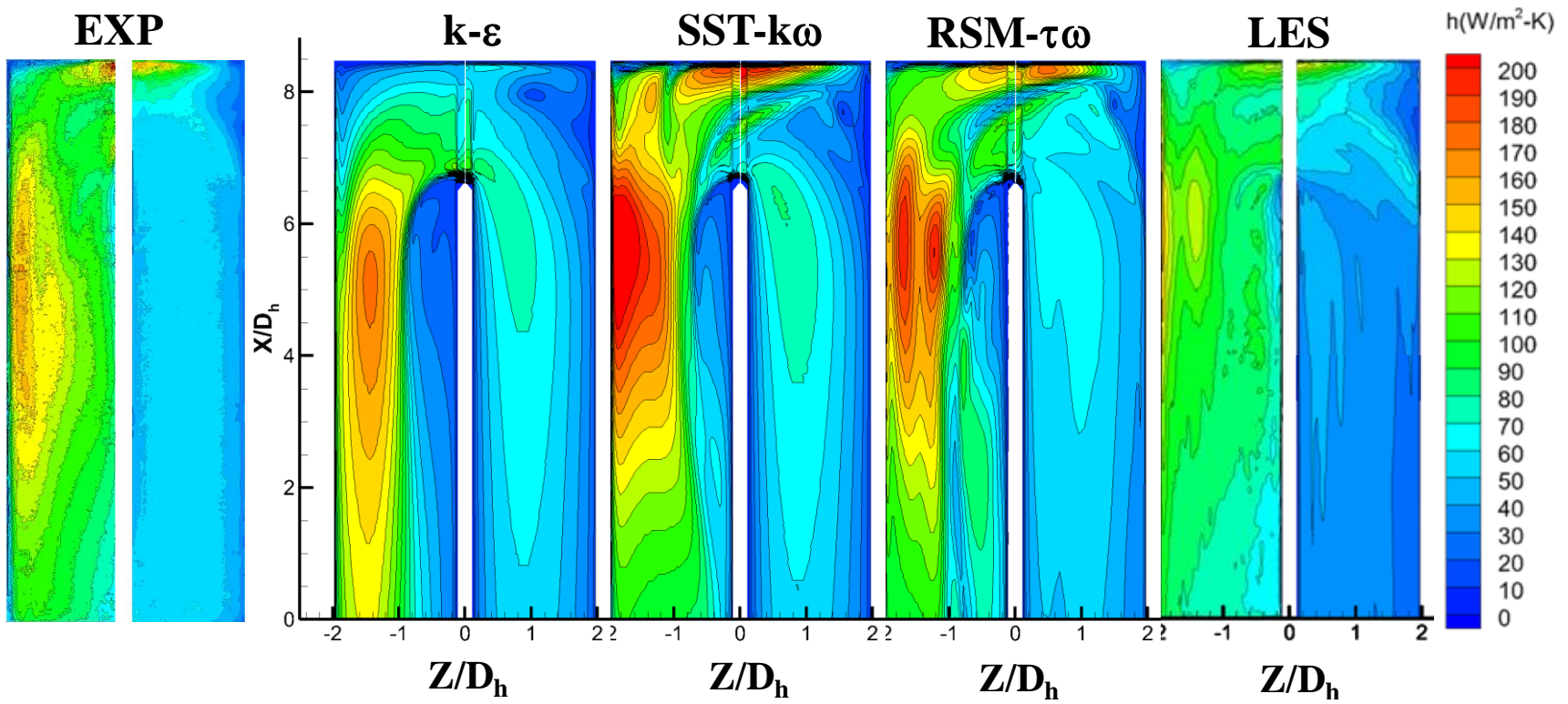
Figure 37. HTC obtained from RANS, LES, and EXP.
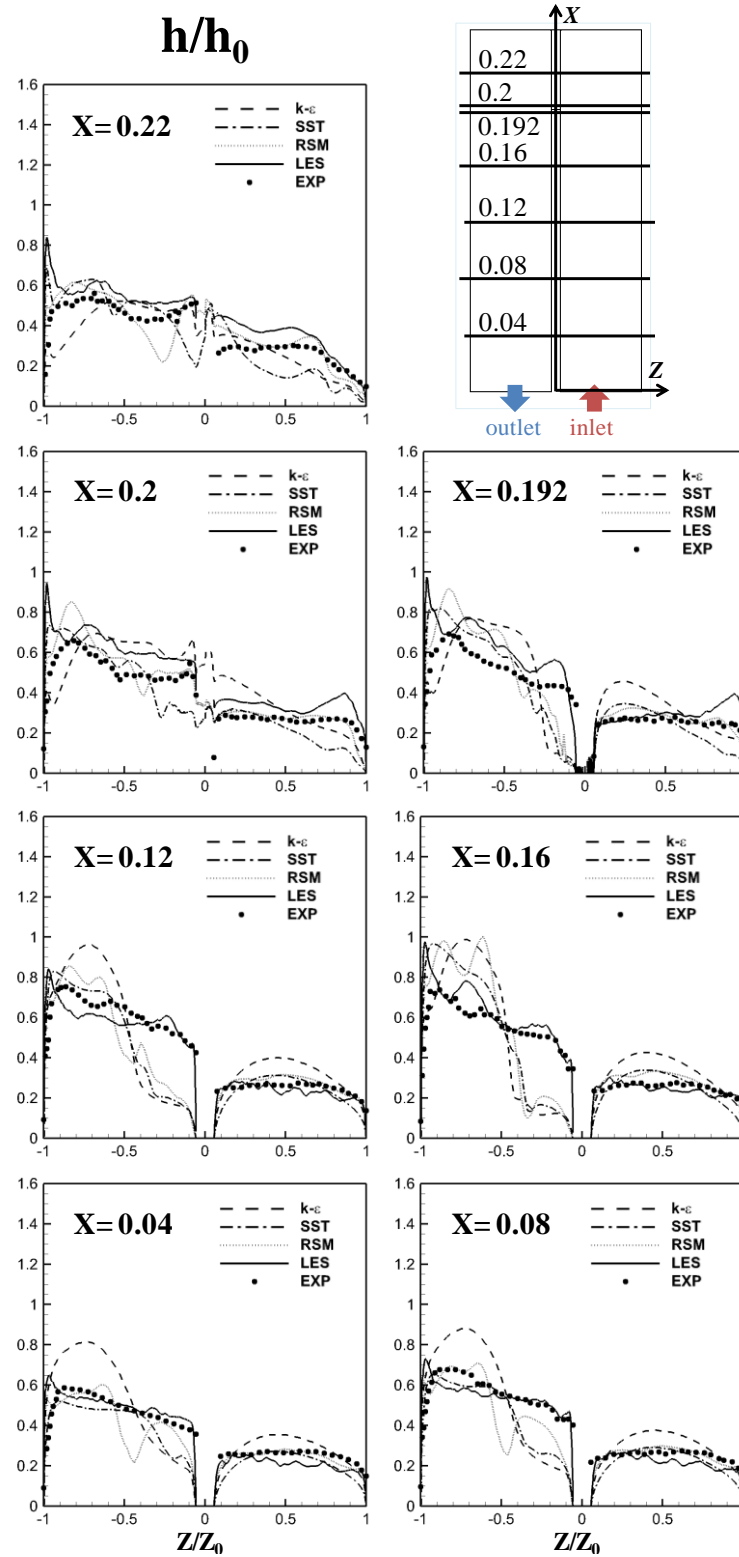
Figure 38. HTC normalized by the maximum value h0 from RANS, LES, and EXP. Z0 denotes the maximum Z of the domain.

3.5.3.2   Flow Field

LES predicted an unsteady separation in the down-leg of the U-duct. This separation starts at the leading edge of the wall that separates the up-leg and down-leg of the U-duct and then sheds. The magnitude of the instantaneous velocity in the symmetry plane is shown in the top of Fig. 39. To examine the frequencies of the shedding, a probe marked as $\oplus$ is inserted about the separation to record the x-velocity. A common operation in analyzing this kind of data is to find the discrete Fourier transform (or spectrum), which converts the time domain to the frequency domain. The transformed frequency domain of the marked probe is shown in the bottom of Fig. 39. In this figure, the peak values in the low frequencies (2.86 Hz, 7.14 Hz, and 12.86 Hz) are occurred by the shedding due to the separation and some other phenomena induced in the turn region. The peak value on 40 Hz frequency indicated the frequency of the dominant energy carrying turbulent vortices because it has the largest amplitude on the frequency domain. Based on the frequency of 40 Hz and the total averaging time of the calculation, about 28 vortices are passed by during the simulation (Appendix A).

In the RANS simulations, the separated region never sheds, is stable, and quite large. One way to assess separation is examine shear stress on the surface. Figure 40 shows the time-averaged shear stress on the surface of the wall where flow separates in the down-leg computed by LES and the three RANS models. The bottom of Fig. 40 shows contours of the shear stress on that entire surface, whereas the top of that figure shows the shear stress along the centerline of that surface. From Fig. 40, it can be seen that LES predicts reattachment of the separation bubble on at around X = 0.09 m, whereas it is X = 0.062m for RSM, and X = 0.01m for SST. For the k-ε model, the separation bubble never reattaches within the U-duct. It is because of this reason that an extension duct was appended to the exit of the U-duct when doing RANS simulations. Note that smaller values of X imply a larger separated region since X is measured from the U-ducts inlet and exit.
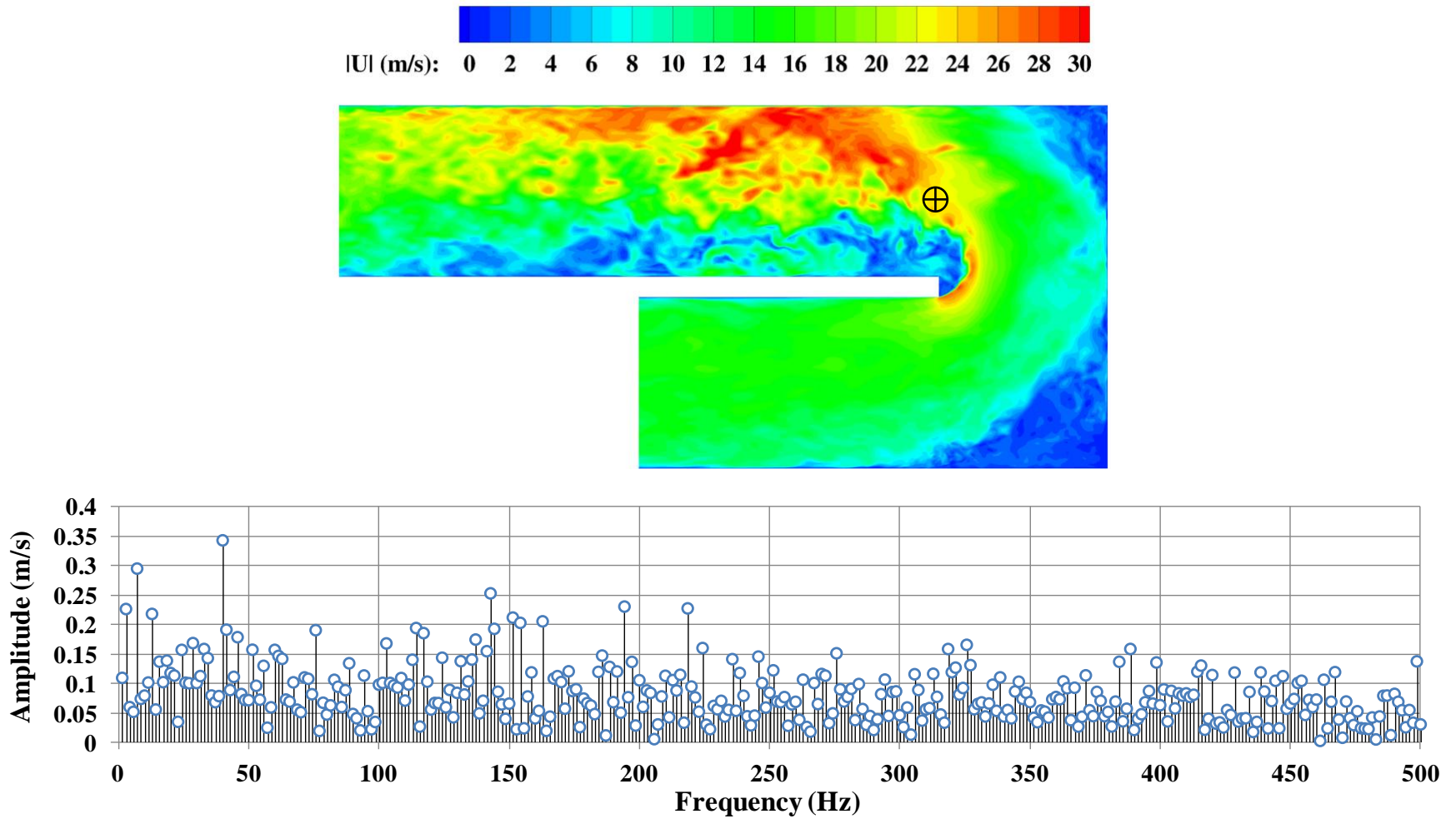
Figure 39. Instantaneous velocity magnitude contour (top) on the symmetry plane and the frequency domain (bottom) on the marked probe.
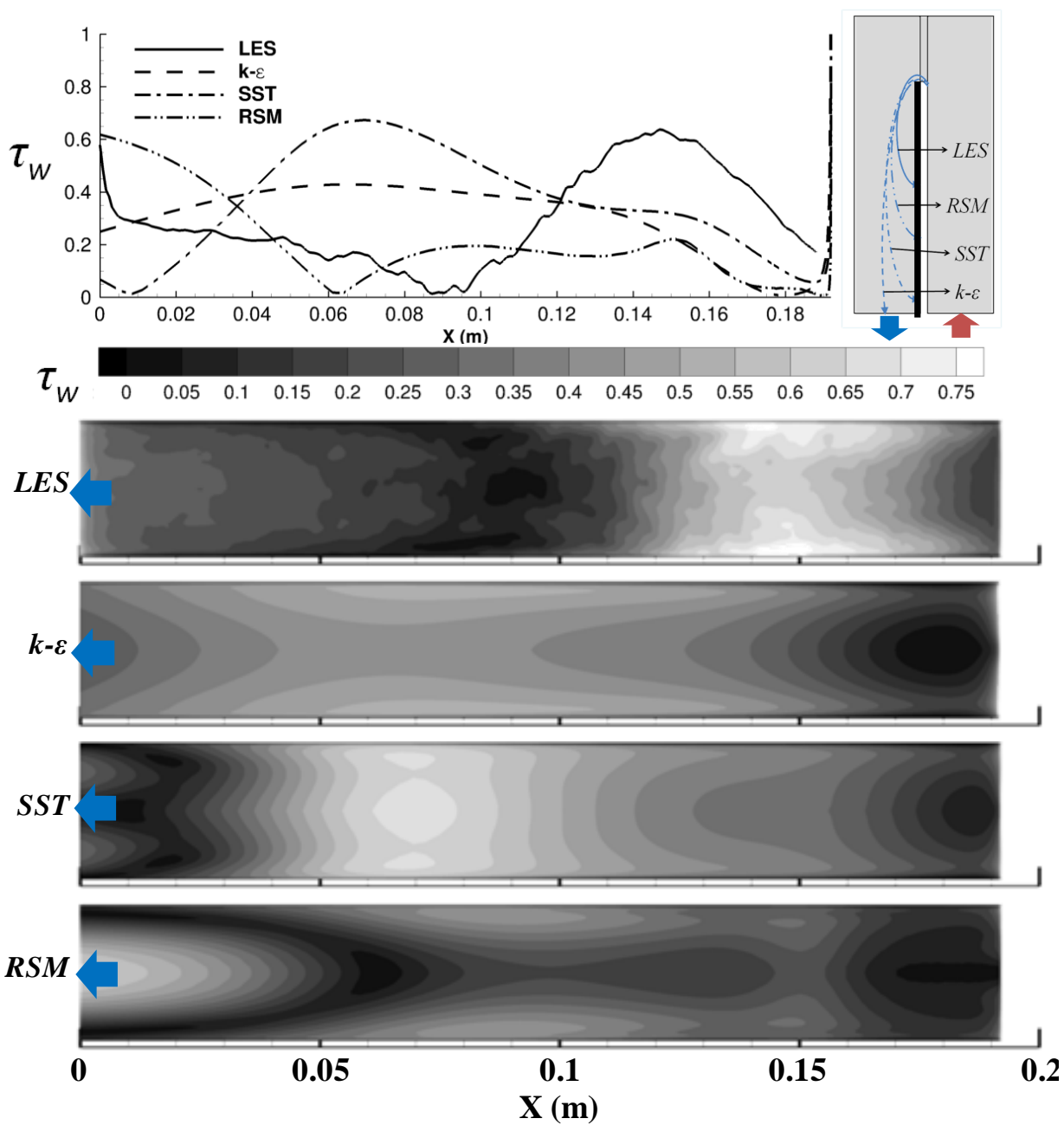
Figure 40. RANS vs. LES: wall shear stress along the down-leg inner wall centerline (top) and the contours of the wall shear stress on the down-leg inner wall (bottom).

3.6   Summary

LES and RANS simulations were performed to study the flow and heat transfer in a U-duct with a high-aspect ratio trapezoidal cross section. On RANS, results were obtained from three widely used RANS models – the realizable k-ε with the two-layer model in the near-wall region, the shear-stress transport (SST) model, and the stress-omega full Reynolds stress model (RSM).

On LES, this study showed wrap-around O-grid next to all walls is better than using H-grids that cluster to all walls because the filter width in LES is typically linked to grid spacing and is assumed to be constant. H-grids produce huge changes in grid spacing about the four corners of the trapezoidal cross section, but O-grids do not. Also, having a concurrent LES of incompressible fully-developed flow in a straight duct with the same cross section and flow conditions as the U-duct produced correct inflow boundary conditions at reasonable cost.

On the RANS simulations, SST and RSM could predict the zonal averaged heat-transfer coefficients (HTCs) with reasonable accuracy as noted in CHAPTER 2. However, this chapter showed that all three RANS models to predict poorly in the down-leg part of the U-duct if the local HTC distribution is of interest. In the down-leg, relative errors in the predicted HTC can be as high 80%.

The LES performed showed the flow mechanism that affected the heat transfer in the down-leg that RANS could not predict. RANS predicted a large and stable separated region in the down-leg from the leading edge of the wall that separates the up-leg and the down-leg in the U-duct, which is incorrect. LES showed that this separation from the leading edge sheds so that the separation is highly unsteady. With unsteady separation, the nature of the flow in the down-leg changes greatly. Thus, this study showed the limitations of three widely used RANS models for a U-duct with high-aspect ratio trapezoidal cross section and why LES is need for this class of flow passages.

CHAPTER 4.   LES VS RANS IN PREDICTING FLOW AND HEAT TRANSFER IN A TRAPEZOIDAL U-DUCT

An earlier version of this chapter was published as 'Kenny S.-Y. Hu and Tom I-P. Shih, "Large-Eddy vs. RANS Simulations in Predicting Flow and Heat Transfer in a U-Duct with a Trapezoidal Cross Section," AIAA paper 2018-4432, 2018 Joint Propulsion Conference. AIAA Propulsion and Energy forum, July 2018, Cincinnati, Ohio, https://doi.org/10.2514/6.2018-4432'.

4.1   Objective

In the previous chapter, the heat-transfer coefficients obtained by RANS and LES are compared with experimentally measured values. In order to assess and guide the development of RANS models, it is important to investigate the source of the discrepancy. In this chapter, the turbulent kinetic energy and Reynolds stresses predicted by the RANS models and LES are compared. Then, pressure-strain rate, pressure diffusion, and turbulent transport obtained by the full Reynolds stress model are compared with those predicted LES. This is followed by an assessment of the predictive capability of models for the velocity-temperature correlations.

The objective of this chapter is twofold. First, provide benchmark LES data that include not only the mean flow and Reynolds stresses but also the pressure-strain rate, turbulent diffusion, turbulent transport, and velocity-temperature correlations. Second, use the data generated to assess and guide the development of widely used RANS models that been discussed in the previous chapters.

4.2   Turbulent Kinetic Energy (TKE): RANS vs. LES

Figure 41 shows the TKE predicted by RANS and LES in planes located at $X/L_1 = 0.16$, 0.33, 0.5, 0.65, turn, 0.8, and 0.9. From this figure, it can be seen that all RANS models are able to predict TKE in the up-leg, but significantly under predict TKE in the turn region and in the down-leg. Since RANS predicted a large separated region in the down-leg, RANS under predicted TKE in the separated region and over predicted TKE for the flow constricted and hence accelerated by the separated region. LES showed high TKE next to the separator because of the unsteady separation at its tip and the passage of separated vortices over its surface.
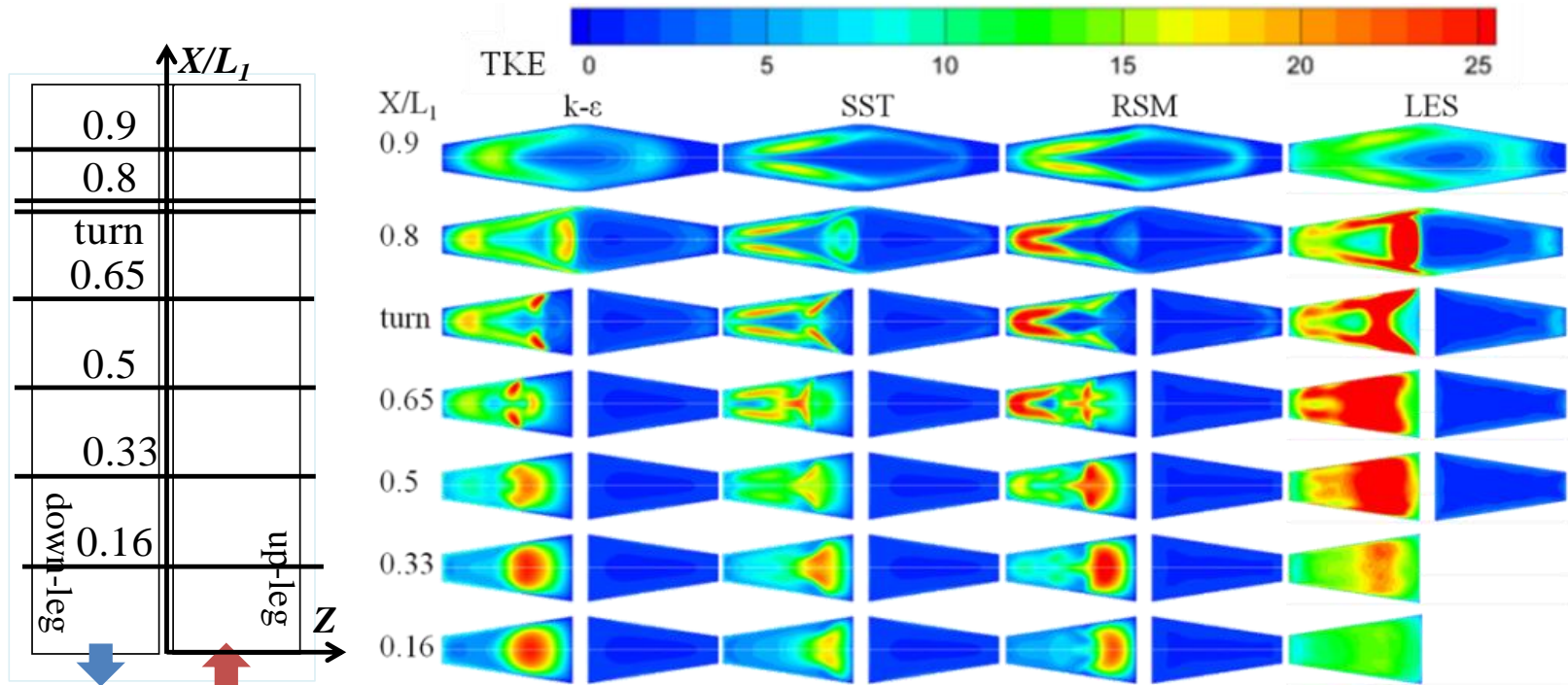
Figure 41. Turbulent kinetic energy (TKE).

4.3   Reynolds Stresses: RANS vs. LES

Figure 42 shows the six components of the TKE and they are normalized by the mean friction velocity on several cutting planes. Since the domain in the RANS simulations only included a symmetric half of the U-duct, the other half plotted in these figures is mirrored without any correction to the sign of the values. For the normal components of the Reynolds stresses, predictions by RANS models show that $\overline{v'v'}$ has about 50% more effectiveness than the other two normal components when the peak values of all three normal components are all at the similar locations in each cutting plane. For LES predictions, all three normal components share the same amount of effect in the sharp corner near the tip of the separator (X/L$_1$= turn). In the down-leg, $\overline{u'u'}$ dominates the shear layer between the main flow and the separation bubble, while $\overline{v'v'}$ dominates the core of the main flow, and $\overline{w'w'}$ dominates the near wall region. Also, despite of the locations, the peak values of three normal components are comparable.

For the shear components of the Reynolds stresses, $\overline{w'v'}$ dominates in the turn region (X/L1= 0.9) for both eddy-viscosity models, while three shear components have equal values for RSM, and $\overline{u'w'}$ dominates for LES at the same location. In the sharp corner near the separator tip (X/L1= turn), similar as the normal components, radical values are obtained by LES, while lower peak values and a shifted location far away from the separator tip are obtained by RANS models. The contours of X/L1= 0.65 can be considered as the continuation of the contours of X/L1= turn. At X/L1= 0.33, a high value area of $\overline{u'v'}$ near the inner wall is obtained by RSM, which does not exist in LES prediction. $\overline{u'w'}$ on the other hand, RSM is the only RANS models that is not able to predict LES results.
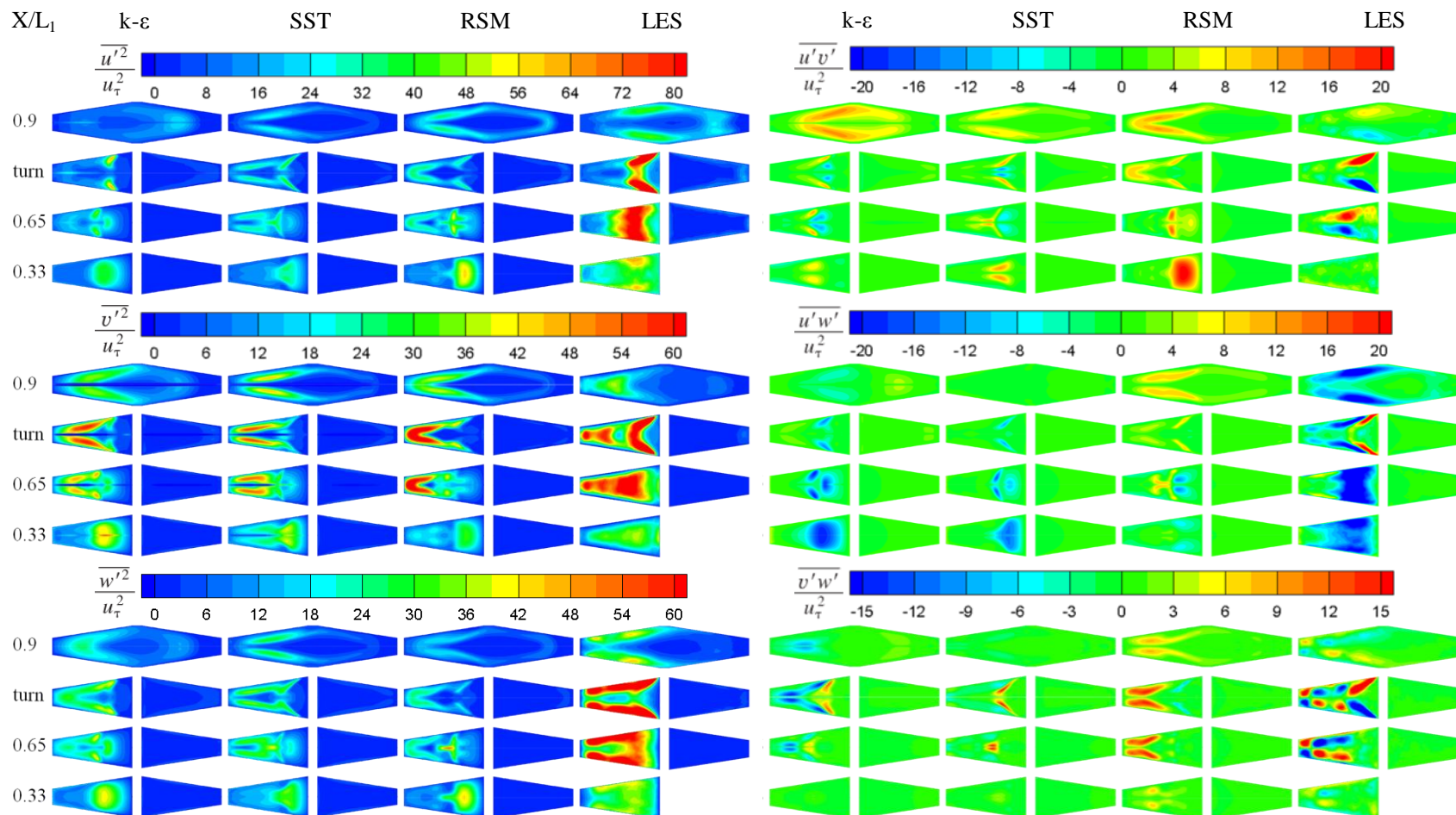
Figure 42. Reynolds stresses (RANS vs. LES).

4.4   Budget Terms Modeling Assessment: RSM vs. LES

For the RSM-$\tau\omega$ model, the most two most challenging terms are pressure-strain rate, pressure diffusion, and turbulent transport. Thus, it is of interest to understand if LES could provide some guidance on the modeling of these terms for this U-duct problem. In this section, pressure-strain rate, pressure diffusion, and turbulent transport based on the exact equations and their models are compared by using data from RSM-$\tau\omega$ and from LES at the locations shown in Fig. 43 to understand where model improvements are needed. This section also compares pressure diffusion to turbulent transport and pressure diffusion to pressure-strain rate based on their exact equations by using LES data to understand their relative importance.

4.4.1   Assessing Modeling of Pressure-Strain Rate

Figure 44 shows the six components of the pressure-strain rate in the turn region at X/L_1= turn, where the flow is the most complicated. For each of these six components, three values are given. Two are based RSM-$\tau\omega$ model, one with RSM-$\tau\omega$ data (denoted as RSM(RSM data)) and one with LES data (denoted as RSM(LES data)). The third value is based on the exact definitions of the pressure-strain rate with LES data (denoted as Exact (LES data)).

Comparing RSM(LES data) and Exact(LES data) shows the RSM model for pressure-strain rate is excellent since the maximum relative error is mostly less than 20%. However, when RSM(RSM data) is compared with RSM(LES data), the relative error is quite large. This indicates that the RSM-$\tau\omega$ has errors, but the error is not from modeling of the pressure-strain rate.

From Fig. 44, the following observations can be made. Pressure-strain rate is significantly under-predicted by using the data from RSM-$\tau\omega$. If LES data is used, then the modeled pressure-strain tensors are higher near the sharp corners and near the top and bottom walls. By comparing RSM(LES data) with Exact(LES data), the shear components can be seen to compare well except Π_{23} in the region near the top and bottom wall but away from the inner wall. However, the normal components are less accurately predicted. This is because the normal components involve TKE, which was under predicted, which in turn causes incorrect prediction of the pressure strain in a circuitous manner.

Comparing RSM (RSM data), RSM (LES data), and Exact (LES data) shows the pressure-strain model proposed by Launder [52] and Wilcox [31] to be quite reasonable qualitatively. Quantitatively, some adjustments are still needed, especially for the normal components in connection with TKE.

4.4.2 Assessing Modeling of Pressure Diffusion and Turbulent Transport

The pressure diffusion term is usually modeled together with the turbulent transport term and collectively called turbulent diffusion budget [31]. And, turbulent diffusion is typically modeled via gradient diffusion – a very simple model for a very complex process. Figure 45 shows the turbulent diffusion tensors calculated by RSM (RSM data) and RSM (LES data) in the middle of three cutting planes: X/L_1 = 0.65, 0.8, and 0.9. According to these figures, results from RSM data follow the trend of LES data in most of the domain, except around the second corner of the separator (Z/W_1 ~ 0 at X/L_1 = 0.8). Only the trend of $D_{T,12}$ is well predicted by RSM data at that location.

Even so, the value of turbulent diffusion predicted by RSM data is about 0.5% of the LES data. If it is compared to the turbulent diffusion calculated by LES data with the exact definition as shown in Fig. 46, the error is quite larger. The modeled turbulent diffusion predicted by RSM data is 10^5 smaller than the exact values, and none of the six components can predict the trend in any location.

To understand the contribution of pressure diffusion (D_p) and turbulent transport (T_T) in turbulent diffusion, D_p and T_T were calculated by using the exact definition with LES data and compared with each other at different locations as shown in Figs. 47 to 49. The validation and verification of the pressure-diffusion calculation are given in Appendix B. From these figures, it can be seen that D_p and T_T can differ in sign, magnitude, and trend. On magnitude, pressure diffusion is at least 10^4 times higher than turbulent transport at all the locations examined. This indicates pressure diffusion dominate in the modeling of turbulent diffusion. Thus, when modeling turbulent diffusion, one only needs to model pressure diffusion. By comparing Figs. 45 and 46 with Figs. 47-49, it can be seen that existing models for turbulent diffusion is orders of magnitude smaller than what they should. This is because the existing model is only modeling the turbulent transport when it should be modeling pressure diffusion.
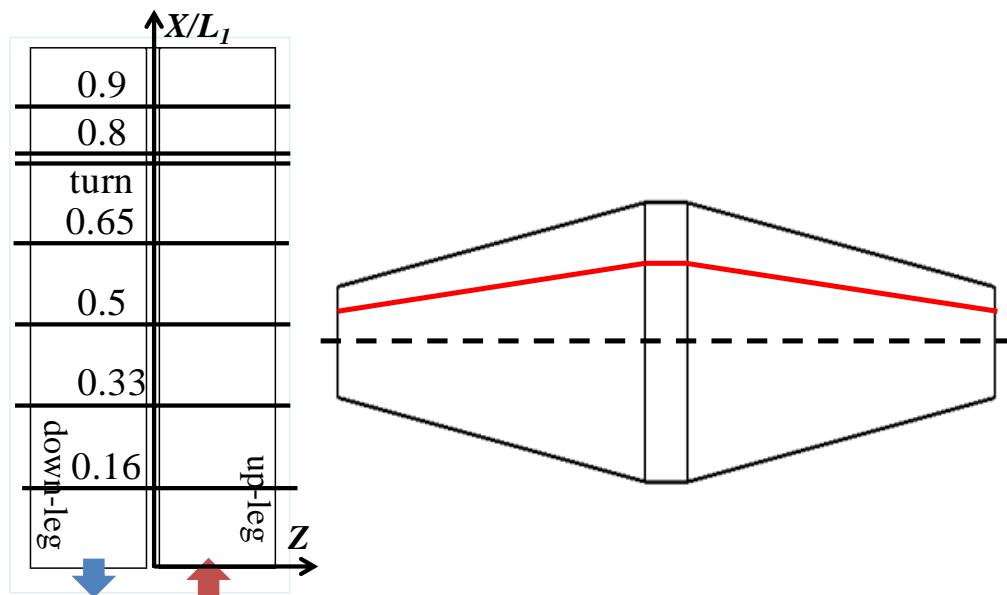
Figure 43. Location where data is extracted.
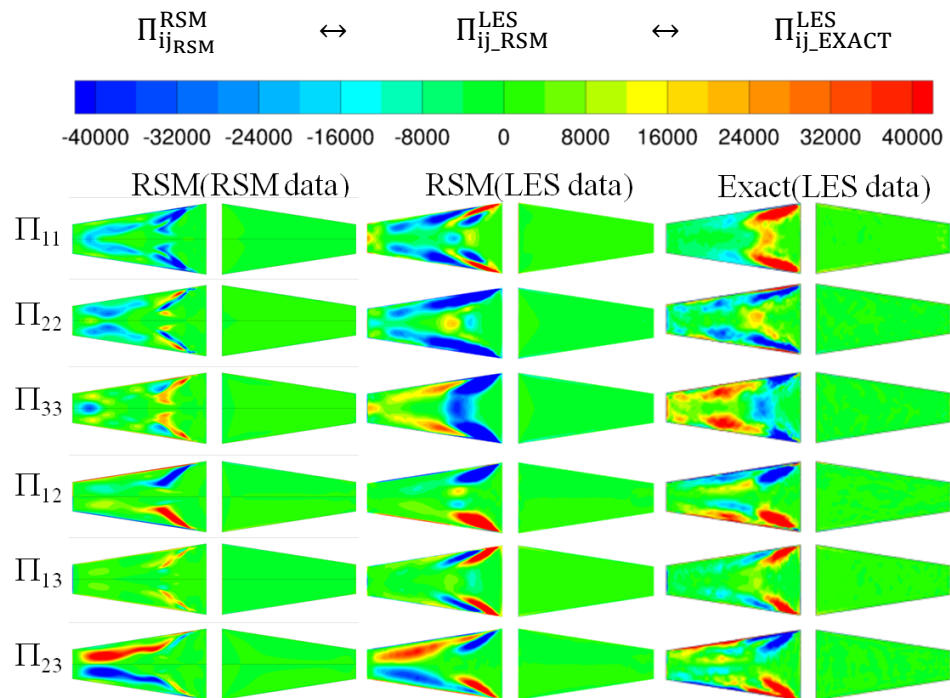
Figure 44. Pressure-strain rate at X/L_1 = turn: RSM-$\tau\omega$ models using RSM data (left) vs. LES data (middle) vs. Exact definition using LES data (right).
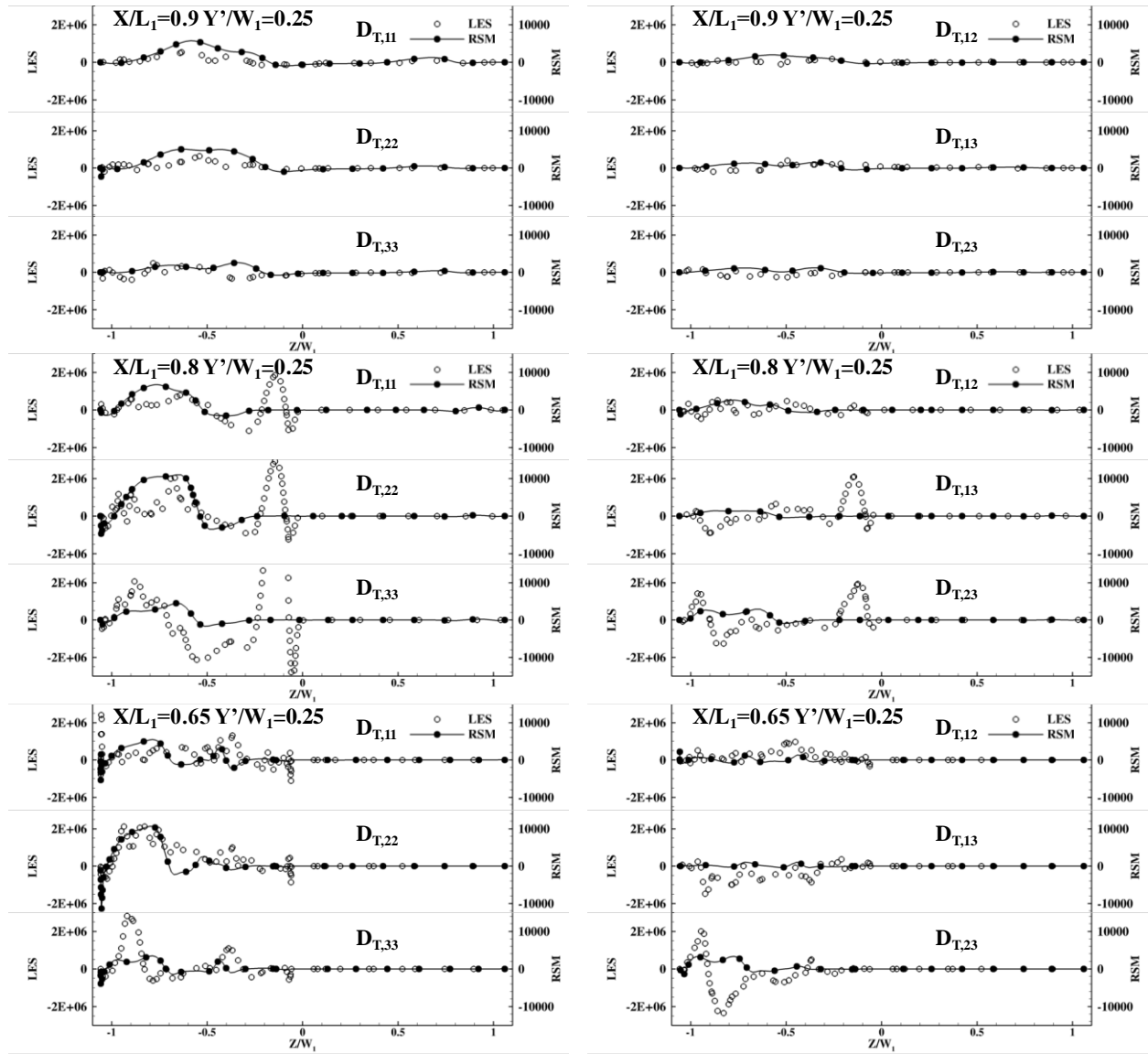
Figure 45. Comparison of turbulent diffusion in RSM calculated by RSM and LES data.
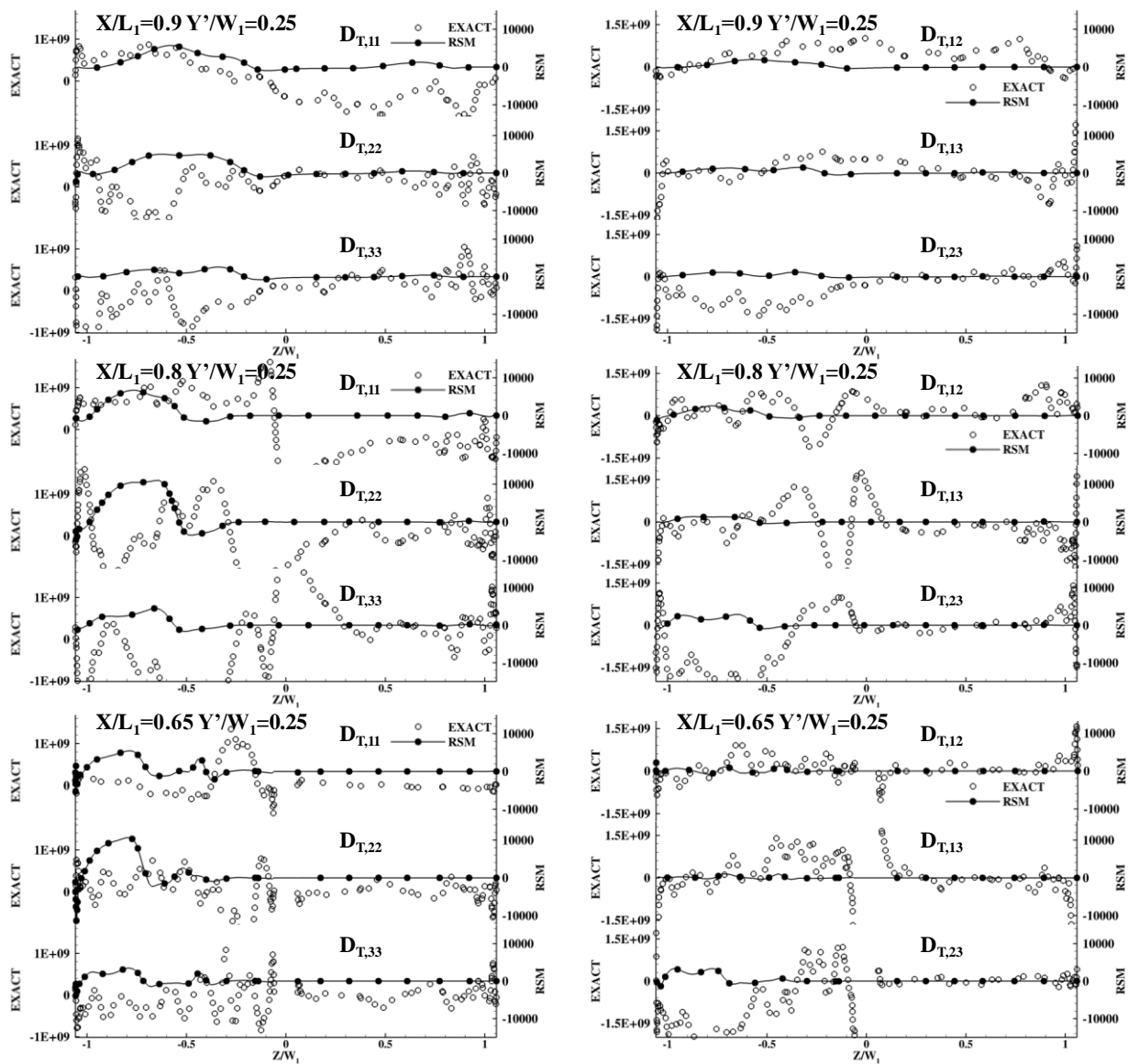
Figure 46. Comparison of turbulent diffusion in RSM calculated by RSM data and in exact definition calculated by LES data.
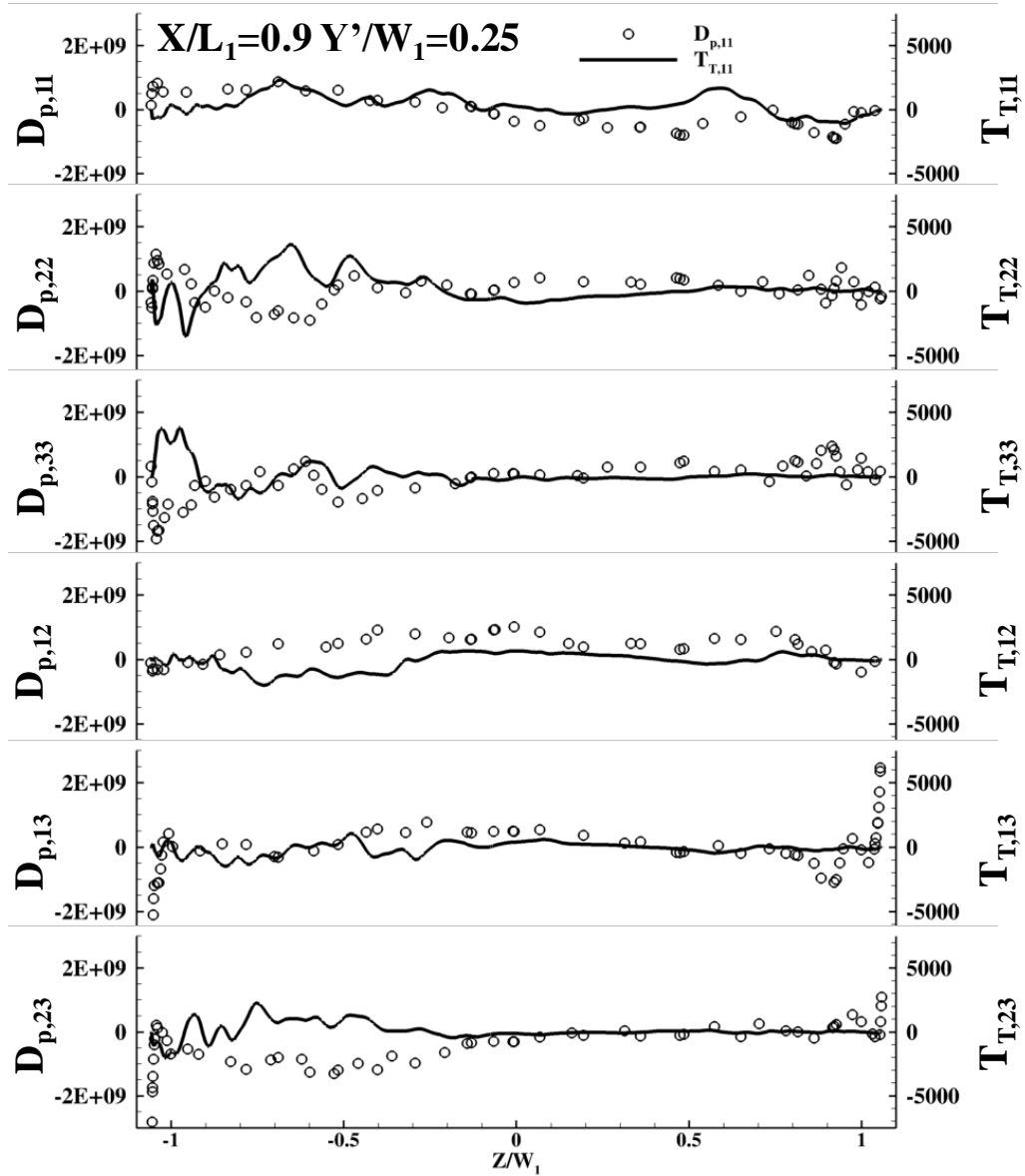
Figure 47. Pressure diffusion vs. turbulent transport at $X/L_1 = 0.9$.
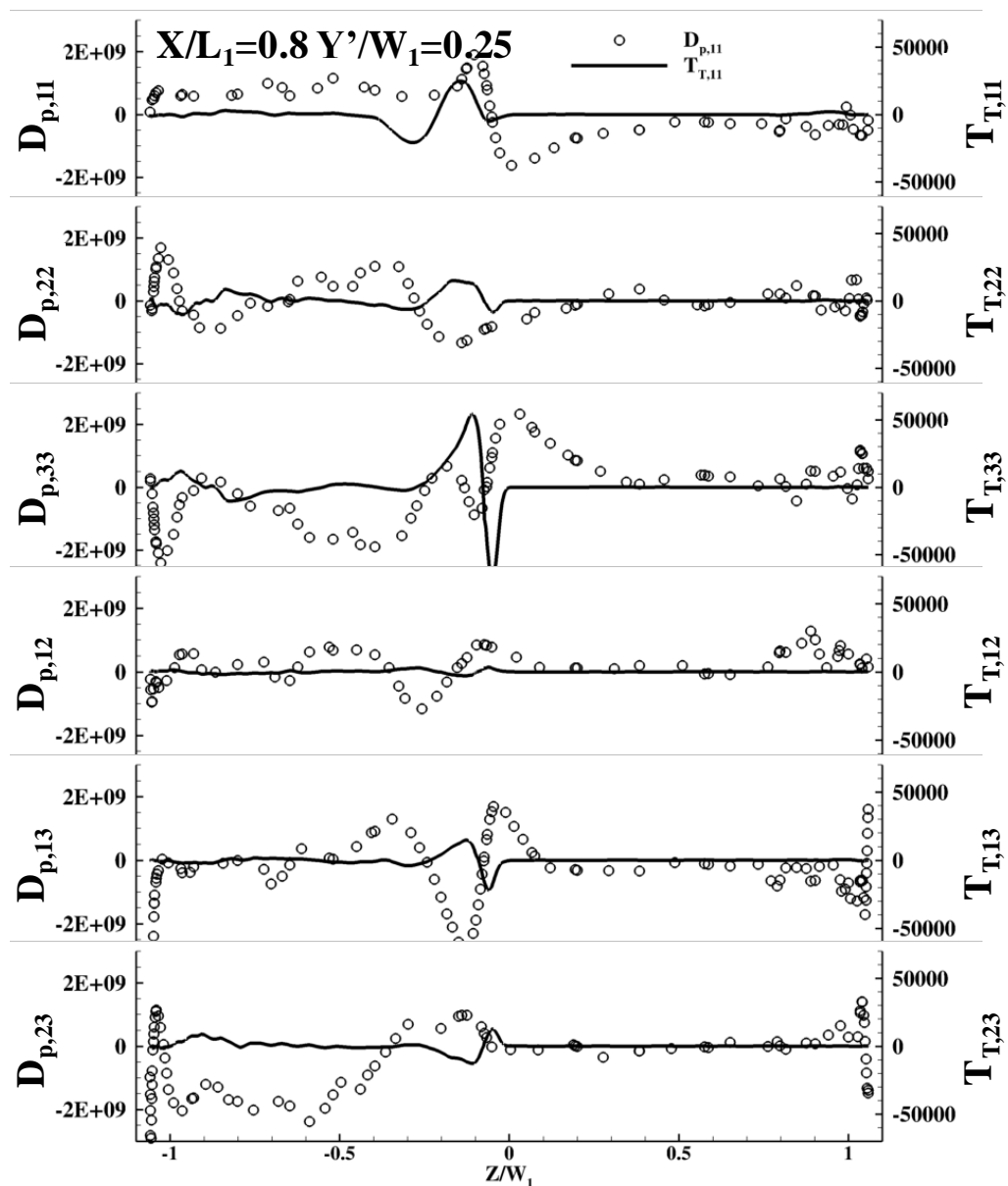
Figure 48. Pressure diffusion vs. turbulent transport at $X/L_1 = 0.8$.
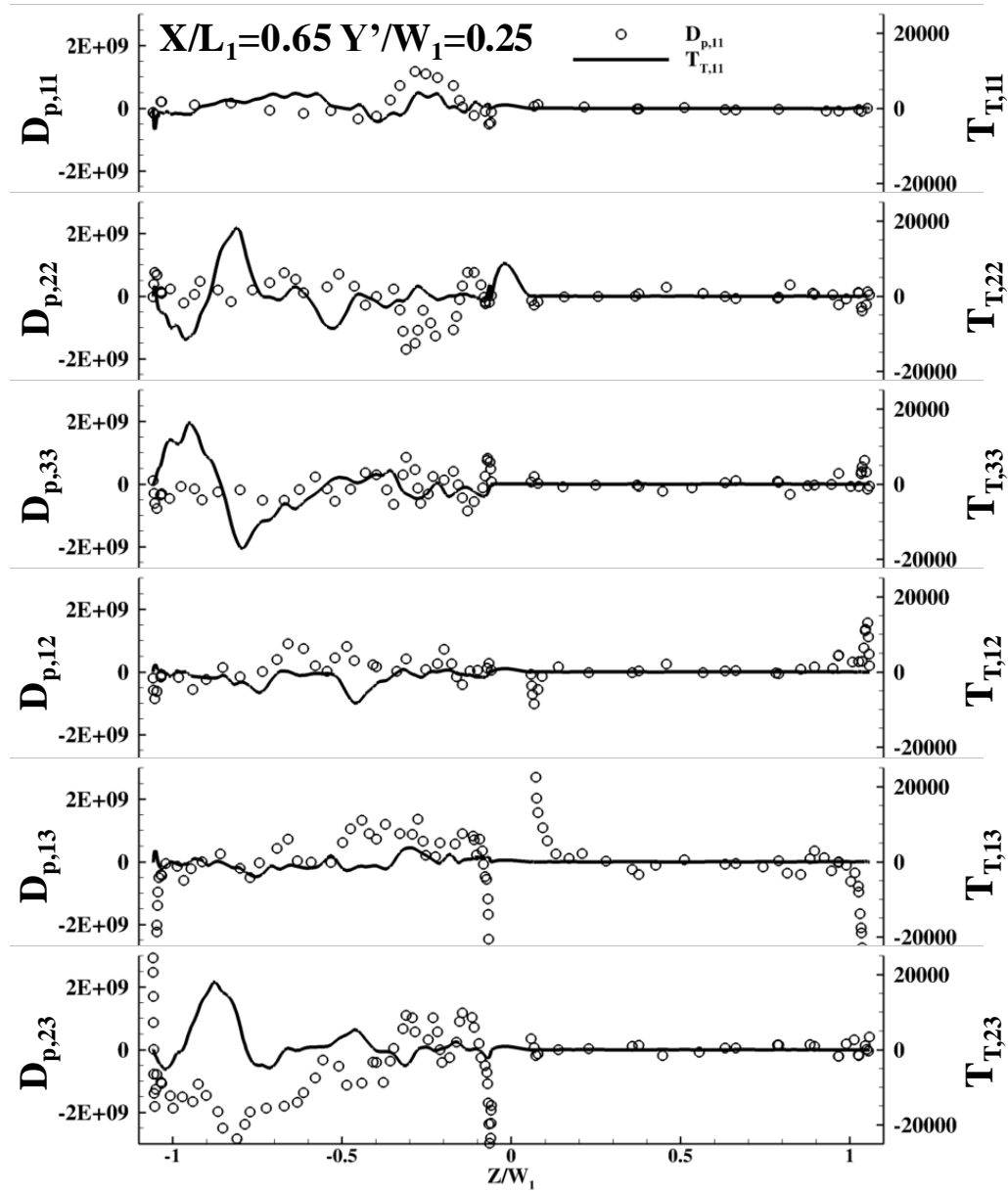
Figure 49. Pressure diffusion vs. turbulent transport at $X/L_1 = 0.65$.

4.4.3   Pressure-Strain Rate vs. Pressure Diffusion

Mansour, et al. [53] proposed pressure-strain rate (Π) and pressure diffusion (D_p) to be modeled together because these two terms have opposite signs and tend to cancel each other near wall boundaries. To examine this assertion, Fig. 50 compares each of six component of Π_{ij} and D_{ij} based on Exact definition using LES data as the following equation:

$$\Pi_{ij} = \overline{\frac{p'}{\rho}\left(\frac{\partial u_i'}{\partial x_j} + \frac{\partial u_j'}{\partial x_i}\right)}$$

$$D_{p,ij} = \frac{\partial}{\partial x_k}\left(\overline{\frac{p'u_i'}{\rho}}\delta_{jk} + \overline{\frac{p'u_j'}{\rho}}\delta_{ik}\right)$$

Pressure-strain rates are shown on the top and pressure diffusion on the bottom. The legends are similarly arranged. From this figure, it can be seen that for the problem being studied, the difference between Π_{ij} and $D_{p,ij}$ can be as high as 10^5. At the tip of the separator, where unsteady separation starts, $D_{p,ij}$ can be 10,000 to 100,000 larger than Π_{ij}. In the down-leg, where separated flows moves downstream, $D_{p,ij}$ is about 50,000 larger than Π_{ij}. Though the magnitudes differ considerably, Π_{ij} and $D_{p,ij}$ have similar qualitative features including their signs, especially in the down-leg. The enormous difference between Π_{ij} and $D_{p,ij}$ in the down-leg shows that Mansour, et al.'s assertion is not always true.

The question now is that what is the physical meaning of $D_{p,ij}$ being much greater than Π_{ij}? When $D_{p,ij} \gg \Pi_{ij}$, Reynolds stresses in the down-leg will diffuse from the outer wall where it is highest toward the inner wall where it is lowest at a much higher rate. This diffusion is so large that it causes the local flow to behave as if its local Reynolds number is near unity. Flows at such low Reynolds numbers can flow about the turn with a small separation bubble. This indicates that when there is unsteady separations, modeling pressure diffusion is as important as modeling pressure-strain rate. As shown in Figs. 45 and 46, the RSM-$\tau\omega$ model developed by Wilcox does have the potential to predict larger values of pressure diffusion tensors yet it is still far from achieving the target.
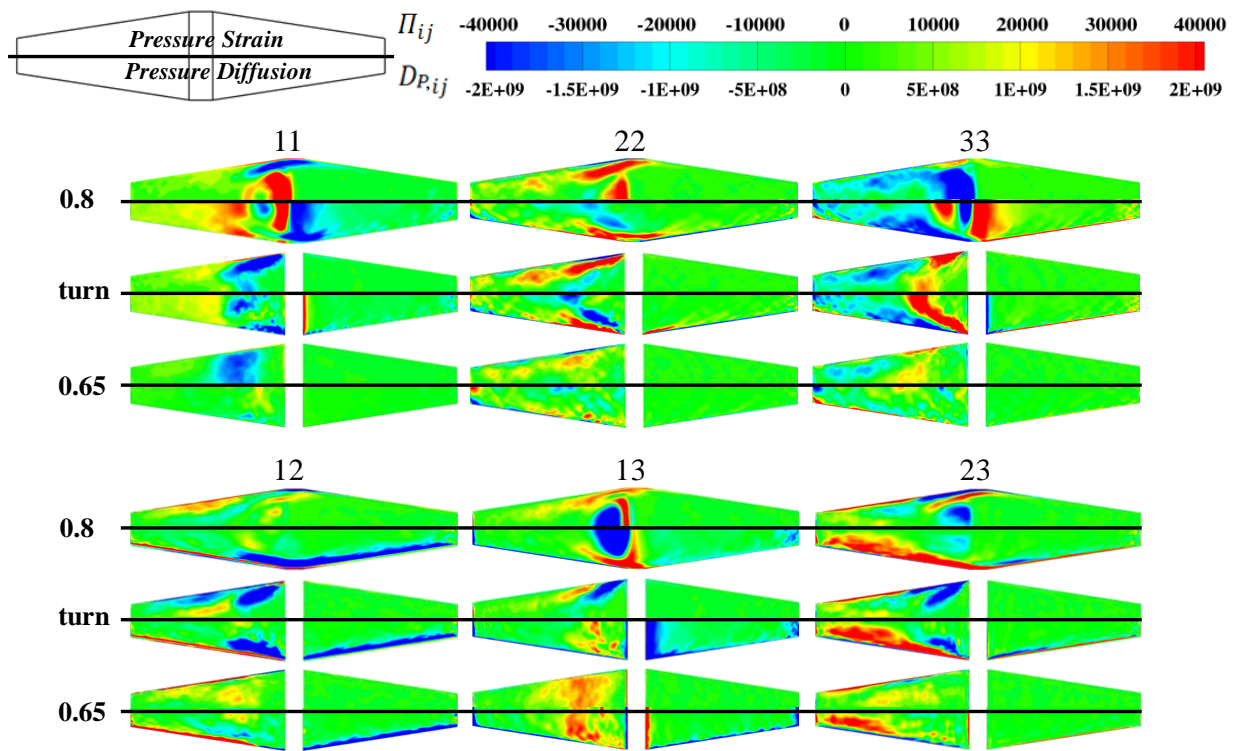
Figure 50. Pressure-strain rate vs. pressure diffusion (exact definition) at

$X/L_1 = 0.8$, turn, and 0.65.

4.5   Eddy Diffusivity Hypothesis: RANS vs. LES

The velocity-temperature fluctuation correlations that close the thermal energy equations computed by k-ε model, SST model, and RSM model are compared to the time-averaged LES data in Fig. 51 on several locations. It shows that $\overline{u'T'}$ has the most difference between LES and RANS everywhere in the U-duct even in the upstream straight part, where $\overline{v'T'}$ and $\overline{w'T'}$ are predicted fairly accurately. In the first turn region, three velocity-temperature correlations, as well as the difference between RANS and LES, grow rapidly. In the entire turn region, the trend of $\overline{u'T'}$ is roughly captured by RANS models but misses the magnitude by a factor around five. Comparatively, $\overline{v'T'}$ modeled by RANS model shows a good agreement with LES data. In the second part of turn region, where Z/W_1<0 and X/L_1= 0.8 and 0.9, k-ε model gives a prediction with similar trend to LES. The same result is not given by SST and RSM. In the prediction of SST and RSM, not only the trends do not follow LES data, even the sign of the values are different for most of the data in that section. However, the divergence disappears in the further downstream in the down-leg, which shows at X/L_1= 0.65. Even so, SST and RSM predict two peaks while only one by k-ε and LES.

The following discussion is divided into two categories represents the two components used in EDH: the temperature gradients and the turbulent diffusivity of heat, which involved the obtained turbulent viscosity and the Prandtl number.

4.5.1   Temperature Gradient

As one of the ingredients in eddy diffusivity hypothesis, the temperature gradients from three RANS models and LES on the middle of the cutting planes (Fig. 43) are compared quantitatively in Figs. 52 to 54. In the up-leg, all RANS models and LES yield similar results for $\partial T/\partial x$ but the inability of predicting secondary flow of eddy-viscosity models causes a noticeable error for both $\partial T/\partial y$ and $\partial T/\partial z$. RSM on the other hand, is able to predict the secondary flow and has a better match of $\partial T/\partial z$ near the inner wall, and even perfectly match at the center of the duct with LES data, but still lacks of accuracy near the outer wall. A common error made by all RANS models is the prediction of $\partial T/\partial y$ in the near wall region, where LES data shows a small area of positive value while no RANS model is able to capture that. Since

secondary flow is not able to be predicted by eddy-viscosity models, it is quite straightforward that the temperature is kept decreasing from the center of the duct toward the walls in any aspect.

However, when the main stream-wise flow dominates and the secondary flow is induced, which is able to be seen by RSM and LES, the hot air is forced from the core of the duct to the corners, and the air cooled by the walls is rolled back around the center of the walls, which causes the positive temperature gradient in y-direction as Fig. 53 shows. The flow patterns in Fig. 55 show that although RSM is capable to predict secondary flow, certain inaccuracy still exists on the size, strength, and location of the corner vortices. On both inner-wall and outer-wall sides, smaller and weaker corner vortices are predicted by RSM closer to the corners, so that the convex contour lines of low temperature as shown by LES do not appear in the prediction of RSM, resulting in the error of $\partial T/\partial y$ near the walls in the straight duct. To improve that, more efforts on accurately approaching $\overline{v'v'}$, $\overline{w'w'}$ and $\overline{v'w'}$ via RSM have to be made.
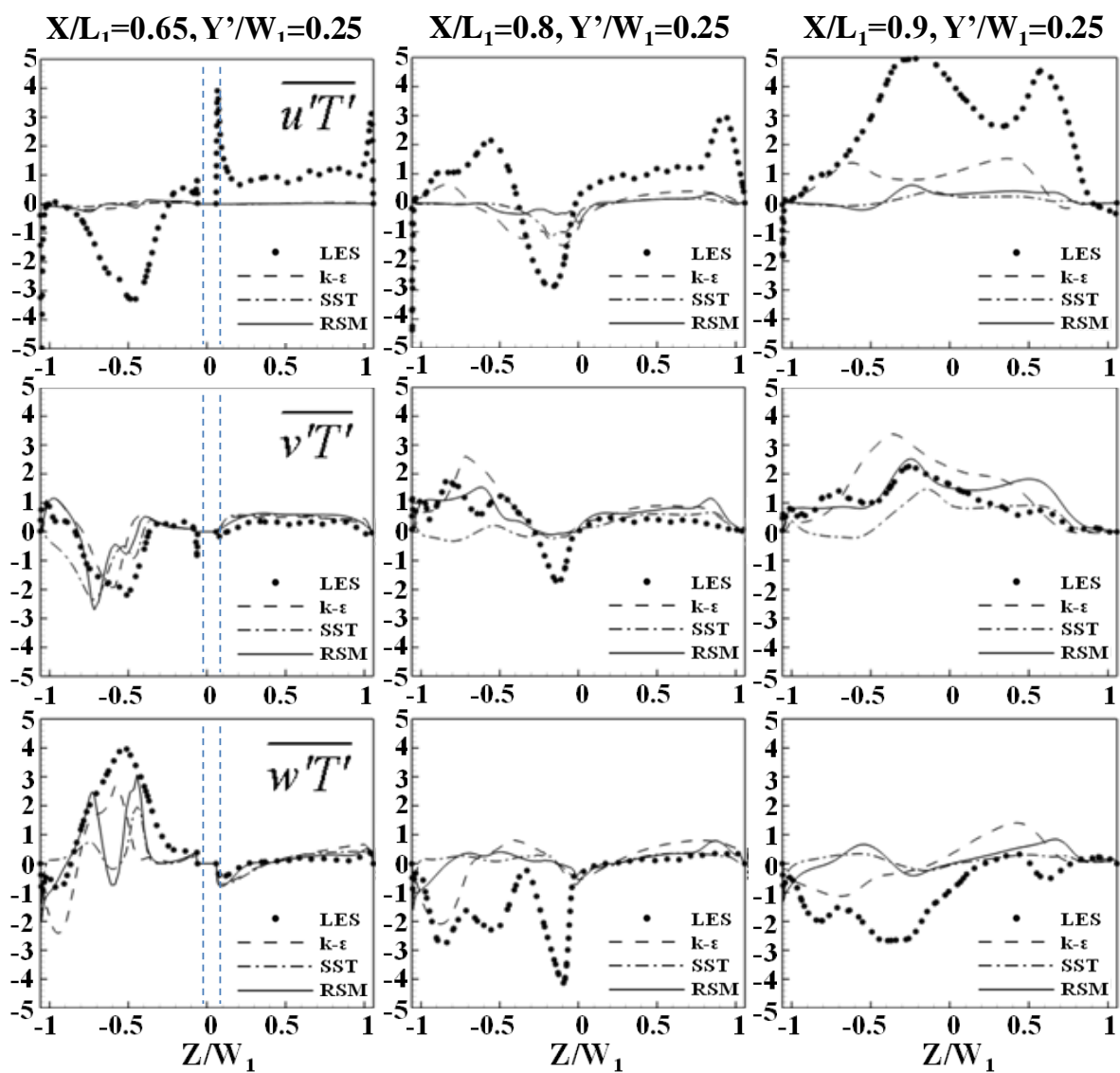
Figure 51. Evaluation of Eddy-Diffusivity Hypothesis of RANS: heat transfer budget.
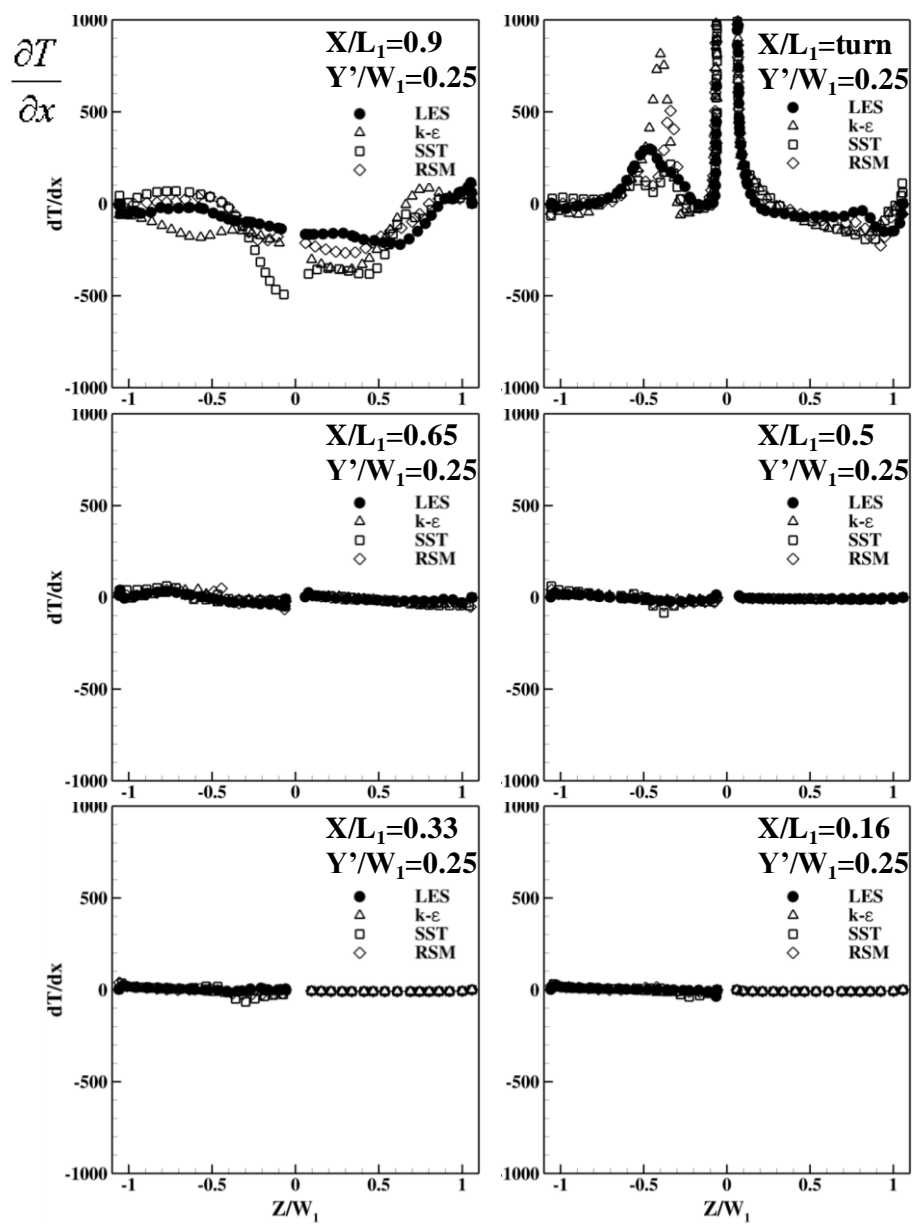
Figure 52. Evaluation of RANS models: $\partial T/\partial x$.

$$\frac{\partial T}{\partial y}$$
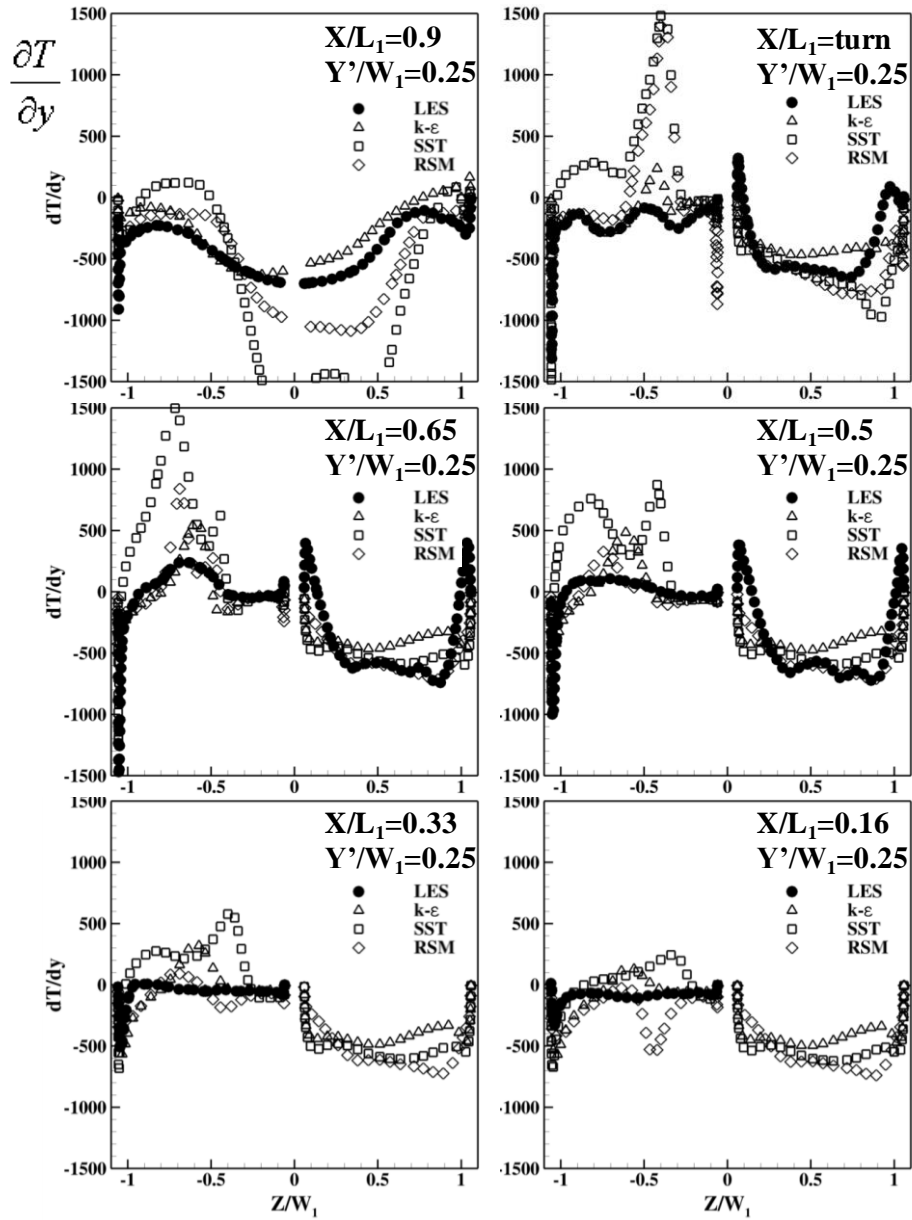
Figure 53. Evaluation of RANS models: $\partial T / \partial y$.
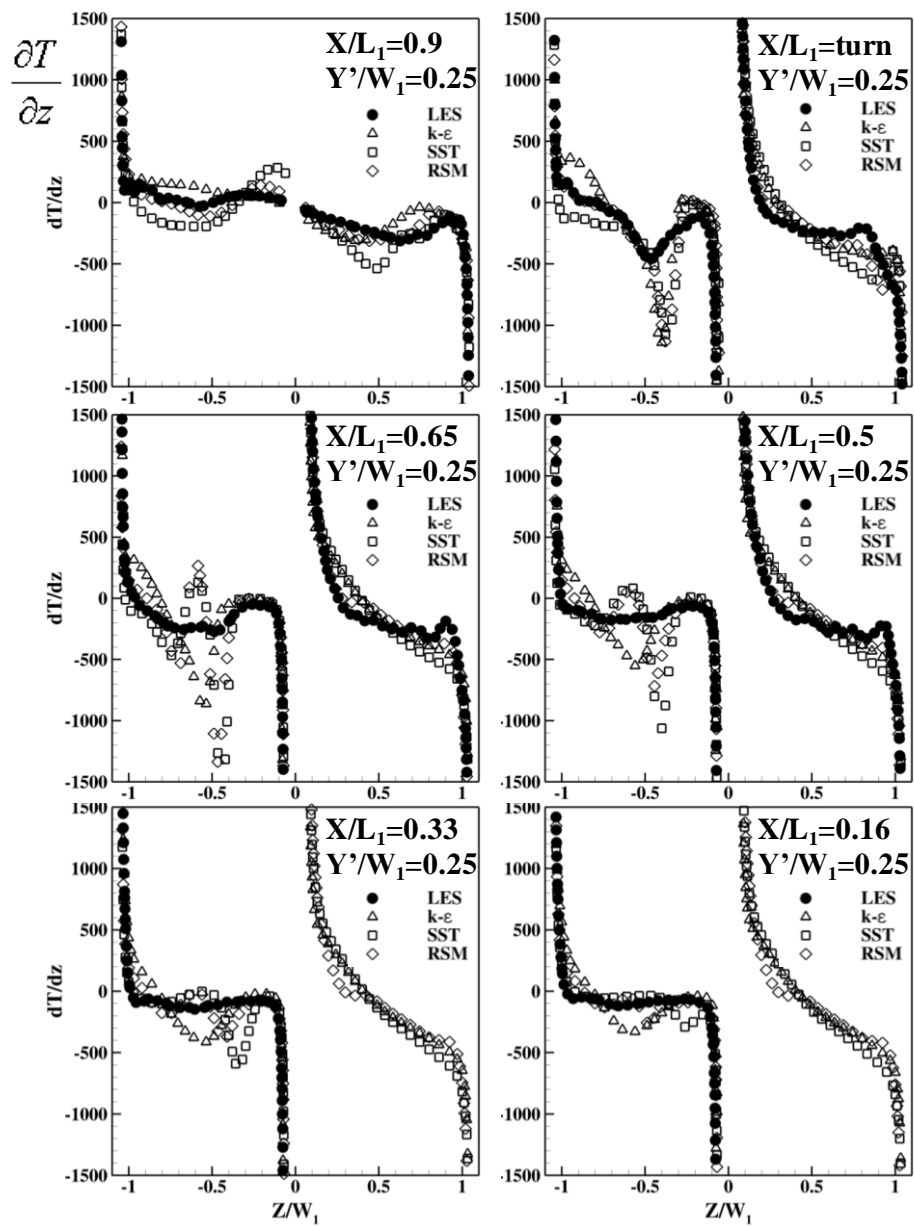
Figure 54. Evaluation of RANS models: $\partial T / \partial z$.
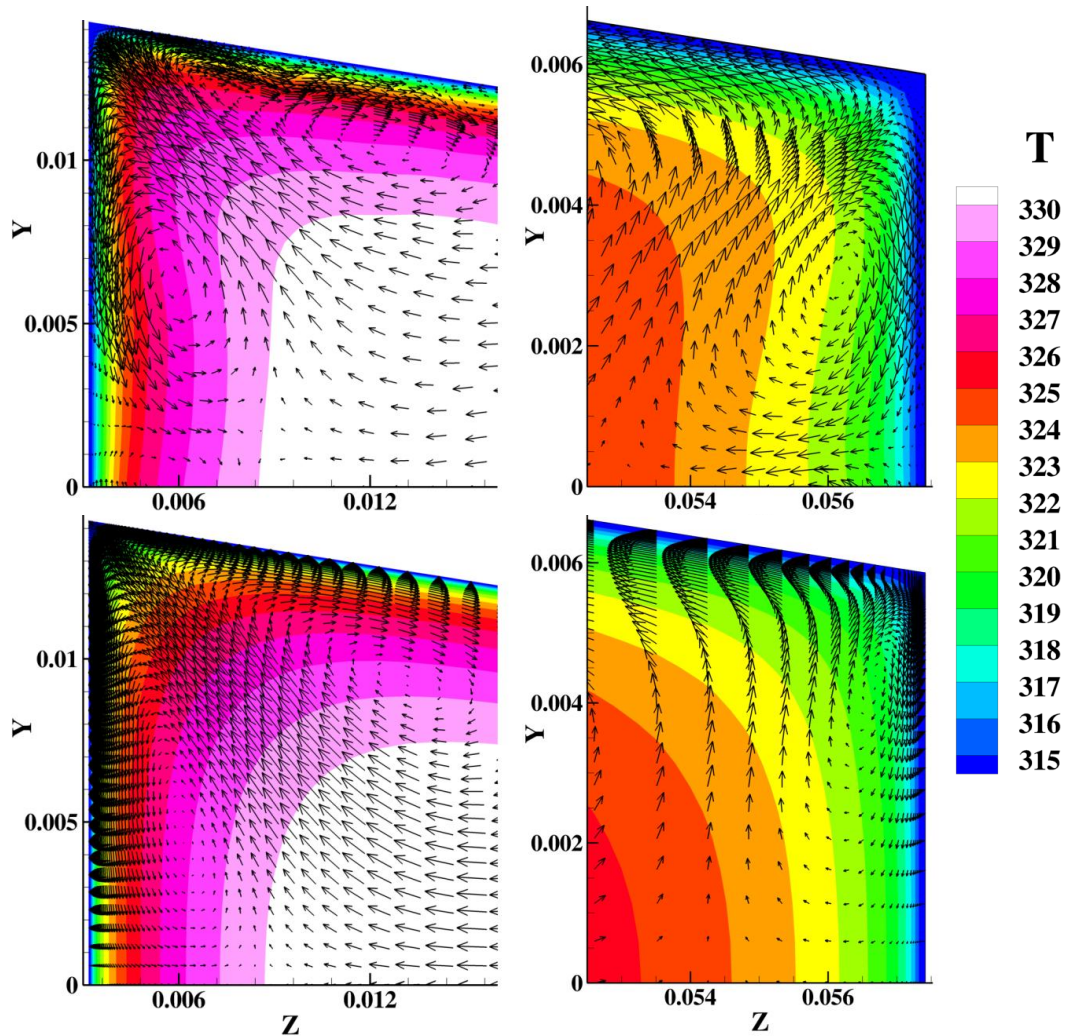
Figure 55. Flow fields in corners of the up-leg near the inner wall (left) and the outer wall (right) on X/L$_1$=0.5, colored by temperature (K): LES (top) vs. RSM (bottom).

4.5.2 Turbulent Diffusivity of Heat & Turbulent Prandtl Number

As another ingredient of EDH, the turbulent diffusivity of heat is modeled by RANS as the following equation:

$$\Gamma_{t,RANS} = \frac{\mu_{t,RANS}}{Pr_{t,RANS}} \tag{24}$$

where

$$Pr_{t,RANS} = \sigma_t = 0.85 \tag{25}$$

$\mu_{t,RANS}$ represents the eddy viscosities computed by k-ε model, SST model, and RSM-τω model.

To evaluate this part of the model, LES data is used to calculate the turbulent diffusivity of heat as well. Since three combinations of velocity-temperature fluctuation correlations and temperature gradients are obtained by LES, least square method is applied once again to satisfy the assumed isotropy of this model, and the turbulent diffusivity of heat is computed by the following equation:

$$\Gamma_{t,LES} = \frac{-\overline{u_i'T'}\dfrac{\partial \overline{T}}{\partial x_i}}{\dfrac{\partial \overline{T}}{\partial x_j}\dfrac{\partial \overline{T}}{\partial x_j}} \tag{26}$$

Then the turbulent Prandtl number can be calculated with the following equation:

$$Pr_{t,LES} = \frac{\mu_{t,LES}}{\Gamma_{t,LES}} \tag{27}$$

The comparison of the turbulent Prandtl number between equation (25) and (27) is plotted in Fig. 56. The constant RANS models used is fairly accurate in the straight duct and in

the turn region. But LES data shows some extreme values around the tip of the separator, where strong shear force occurs, and near the inner-wall of the down-leg, both before and after the reattachment of the separation flow. The calculated turbulent Prandtl number ranged from -15 to 15 in the shear layer between the separation flow and the main flow, -3 to 15 near the inner-wall before the reattachment, and -20 to 3 near the inner-wall after the reattachment.

4.6   Summary

Large-eddy simulations (LES) show k-ε, SST, and RSM models to be inadequate in predicting the flow and heat transfer in the turn and down-leg regions of the U-duct because they were unable to predict the unsteady flow separation about the separator that was induced and sustained by turbulent fluctuations and not by geometry or asymmetry.

Basically, k-ε and SST could not predict any of the Reynolds stresses correctly in the turn region and in the down-leg of the U-duct. For RSM-τω, the modeling of the pressure-strain rate was found to match LES data well qualitatively and quantitatively. On turbulent diffusion, the exact correlations based on LES data can be up to five orders of magnitude higher than those predicted RSM-τω. This huge error indicates that the two terms in turbulent diffusion – turbulent transport and pressure diffusion – should be modeled separately. LES data shows turbulent transport to be ignorable throughout the entire domain. Thus, the focus should be on modeling the pressure diffusion. Unfortunately, RSM-τω model currently still lacks the ability to provide correct modeling of pressure diffusion for this class of flows. On the velocity-temperature correlations, only $\overline{v'T'}$ is reasonably well-predicted, but not $\overline{u'T'}$ and $\overline{w'T'}$, not even qualitatively. The eddy-diffusivity model for the velocity-temperature correlations was found to be an extreme over simplification because the turbulent Prandtl number is clearly not a constant and can vary appreciably. The LES data could be used to guide the development of a better model for these terms.
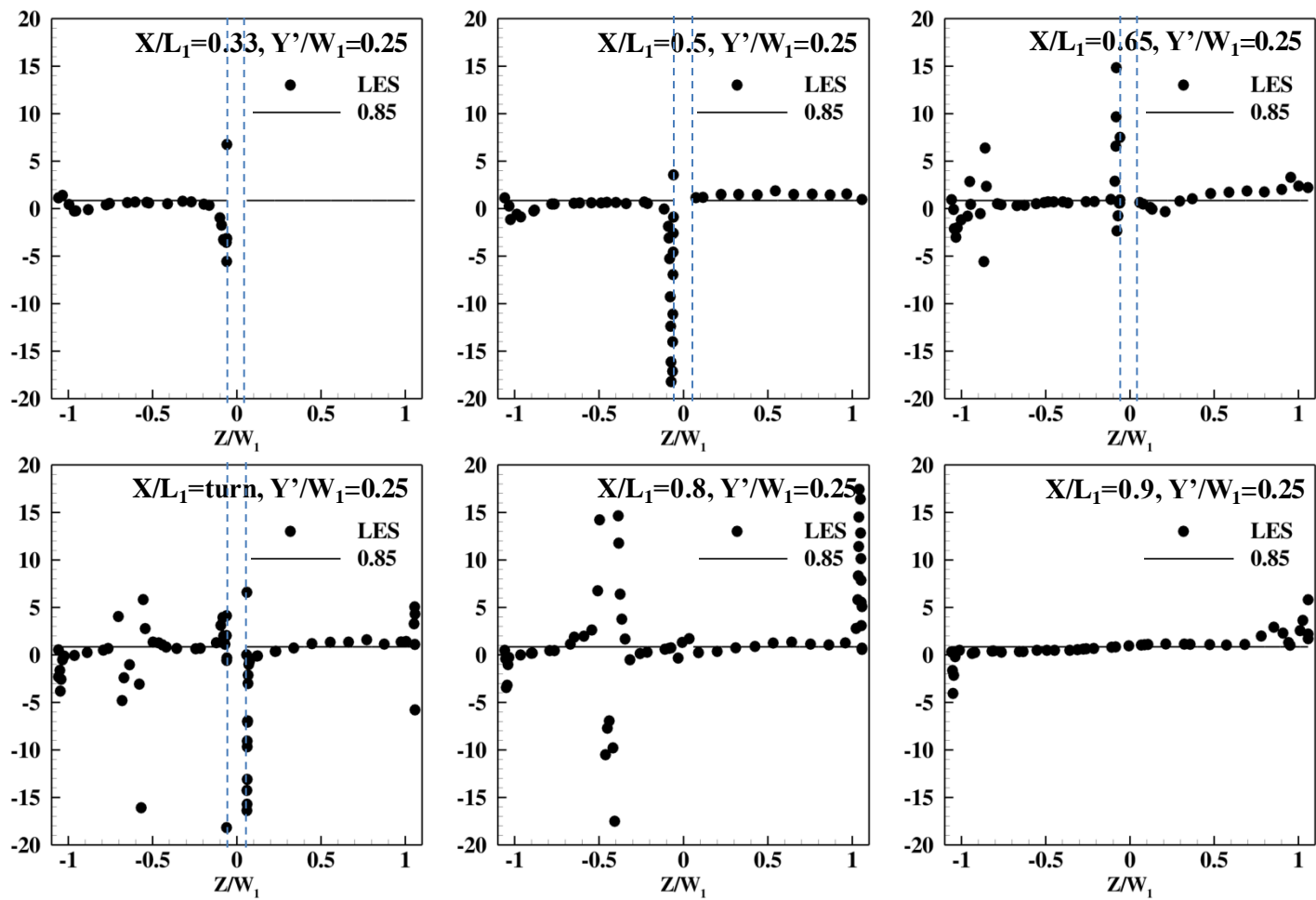
Figure 56. Evaluation of Eddy-Diffusivity Hypothesis of RANS: turbulent Prandtl number.

CHAPTER 5.   CONCLUSION

In this chapter, the key findings from the previous chapters are summarized. First, the performances of four popular RANS models were assessed for the "smooth" and "pin-finned" U-duct by comparing the heat transfer coefficient with the experimental measurements. Second, to ensure the accuracy of LES, two grid types and two grid resolutions were evaluated by investigating the straight duct with square cross section. Also, the correctness of the inflow boundary condition for the U-duct was ensured. Next, the flow field and the heat transfer from RANS simulations and LES were compared to show the disability of RANS models. Lastly, the details of the inaccurate predictions from RANS models were indicated and the guidance from LES results was provided.

5.1   Steady RANS: Smooth vs. Pin-Finned U-duct

5.1.1   Smooth U-duct

- Similar results were provided by all RANS models in the up-leg duct but only RSM-$\tau\omega$ and RSM-LPS could capture the corner vortices, namely the secondary flow, because they can account for anisotropic effects of turbulence.

- In the turn region and beyond, realizable k-ε and RSM-LPS, as well as SST and RSM-$\tau\omega$, yielded similar predictions due to the usage of the same model in the near-wall region. This showed the modeling in the near-wall region dominates the prediction of surface heat transfer for the smooth U-duct.

- In the turn region, a jet-like flow impinges on the U-duct's tip, which enhances heat transfer on the tip wall as well as on the top and bottom walls, can only be predicted by SST and RSM-$\tau\omega$.

- Around the bend in the down-leg, all models predicted a large separated region. The heat transfer is greatly reduced in the separation but increased outside of the separation, where the flow is accelerated.

- The Dean-type secondary flows transported cooler fluid from the core of the U-duct to the walls. Based on the averaged HTC predicted, the SST model is preferred because of its accuracy and its ease of use.

5.1.2   Pin-Finned U-duct

- The pin fins transfer considerably more heat on the leading edge of each pin fin where the flow impinges on it than the top and bottom walls. On the top and bottom walls, heat flux is highest in the region where the horseshoe vortex is induced by the pin fins and lowest in the wake region.

- The pin fins behaved like guide vanes in the turn region, resulting in the size of the separation bubbles are enormously reduced.

5.2   LES Methodology

- The wrap-around O-grid next to all walls is better than H-grids that cluster to all walls. Typically, the filter width in LES is linked to grid spacing and is assumed to be constant. H-grids produce huge changes in grid spacing about the four corners of the trapezoidal cross section, but O-grids do not.

- A concurrent LES of incompressible fully-developed flow in a straight duct with the same cross section and flow conditions as the U-duct produced correct inflow boundary conditions at reasonable cost.

5.3   RANS vs. LES: Flow and Heat Transfer

- LES can predict HTC with the experimental measurement within 10% relative errors in the down-leg, whereas the results provided by RANS models can be as high as 80%.

- LES showed that the separation from the leading edge sheds so that the separation is highly unsteady. The nature of the flow in the down-leg changes greatly by this unsteadiness. All RANS models are inadequate due to their incapability of predicting this unsteadiness and shedding around the bend. Hence, LES is needed for this class of flow passages.

5.4   Guidance from LES

5.4.1   Eddy-Viscosity Models

- For k-ε and SST, the secondary flow could not be predicted in the up-leg duct, and the

Reynolds stresses could not be predicted correctly in the turn region and in the down-leg of the U-duct.

5.4.2   Stress-Omega Reynolds Stress Model

- The modeling of the pressure-strain rate, which was considered the most important term, was found to match LES data well qualitatively and quantitatively.

- On turbulent diffusion, the exact correlations based on LES data can be up to five orders of magnitude higher than those predicted by RSM-$\tau\omega$. By using the data obtained from LES, the two terms in turbulent diffusion – turbulent transport and pressure diffusion – were found to be prodigious distinct to each other.

- LES data shows the turbulent transport to be ignorable throughout the entire domain. The focus should be on modeling the pressure diffusion.

- By comparing the pressure-strain rate and the pressure diffusion using LES data with the exact definition, these two terms were found to be analogous despite the fact that the pressure diffusion is around 50,000 larger than the pressure-strain rate. The factors in the pressure-strain rate model could play a role when developing better models for pressure diffusion.

5.4.3   Eddy-Diffusivity Hypothesis

- The eddy-diffusivity hypothesis for the velocity-temperature correlations was found to be an extreme over simplification because the turbulent Prandtl number is clearly not a constant and can vary appreciably. The LES data could be used to guide the development of a better model for these terms.

APPENDIX A. LES DATA AVERAGING FOR U-DUCT CASE

For the LES of the U-duct, Fig. 57 shows the history of the x-velocity and the gradient of x-velocity with their instantaneous values, "moving" time-averaged values, and the "moving" standard error. The definitions of each curve are described below:

$$Instantaneous\ Value\ (t) = u(0.1 + N\Delta t)$$

$$Mean\ Value\ (t) = \overline{u(0.1 + N\Delta t)} \equiv \sum_{k=1}^{N} \frac{u(0.1 + k\Delta t)}{k}$$

$$Standard\ Error\ (t) = SE(0.1 + N\Delta t) \equiv \sum_{j=1}^{N} \left\{ \frac{u(0.1 + j\Delta t) - \overline{u(0.1 + N\Delta t)}}{j} \right\}$$

where $N \in \mathbb{Z}^+$, $\Delta t = 0.00001$ is the time step size.

The mean velocity and the mean velocity gradient are averaged from t = 0.1 to 0.832. The Reynolds stresses, the velocity-pressure correlations used to analyze the pressure-strain rate and the pressure-diffusion, and the triple correlations used to analyze the turbulent transport are averaged from t = 0.3 to 0.832. In this figure, the "moving" mean values are approaching to steady values and the standard errors are approaching 0, which means the time-averaged data are approaching steady state and ready to be used for analyses.
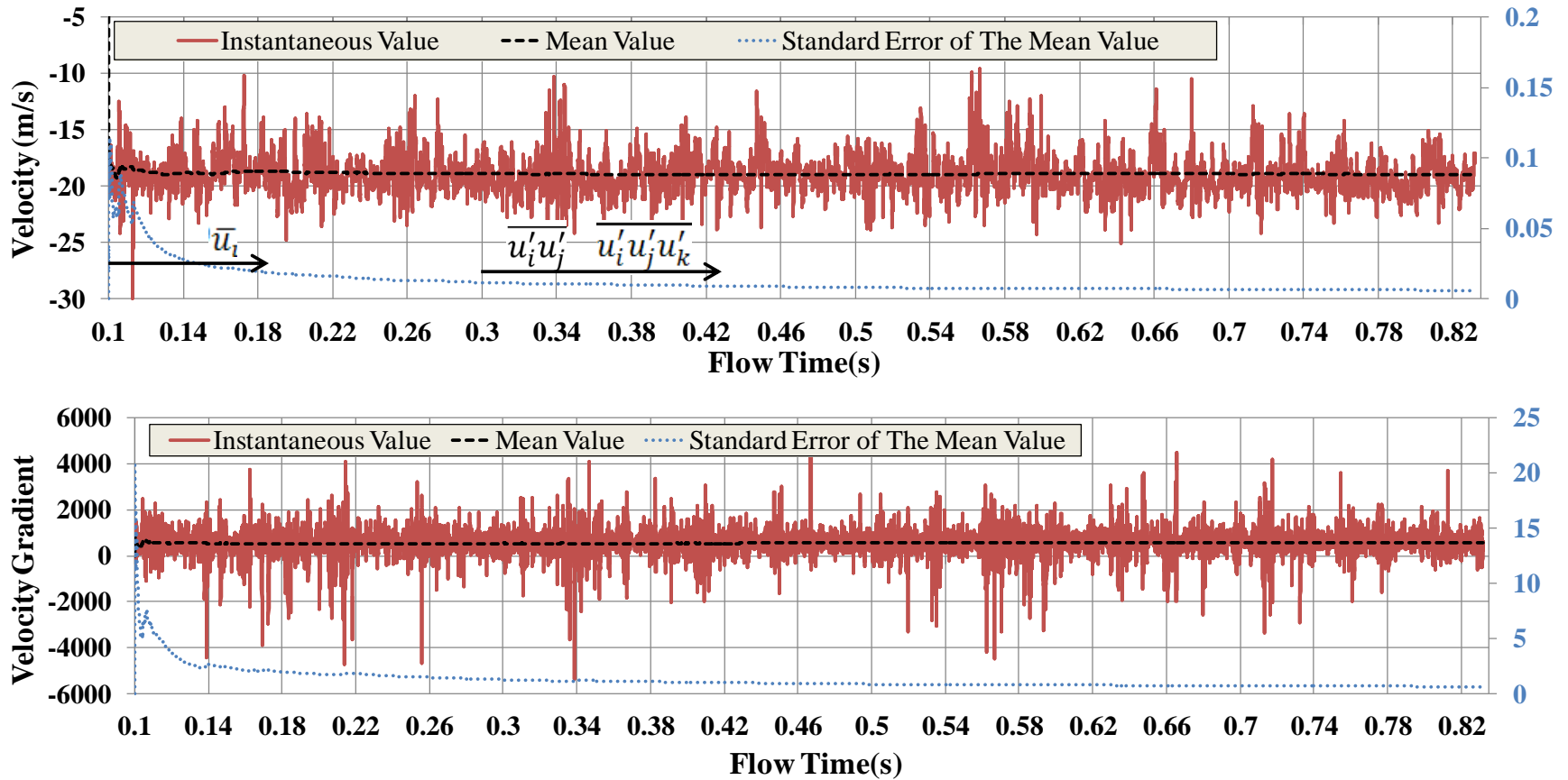
Figure 57. Instantaneous values, time-averaged values, the standard error of the time-averaged values of the velocity (top) and the velocity gradient (bottom) in x-direction on the probe marked in Figure 39.

APPENDIX B.   VALIDATION AND VERIFICATION FOR PRESSURE DIFFUSION CALCULATION

To validate and verify the calculation for the pressure-strain rate, the pressure diffusion, and the turbulent transport, the same processors were operated for the square straight duct simulation and the results were shown in Fig. 58 (a). From the figure, these three terms were in the same order of magnitude and none of them was obviously dominant. Three of the pressure diffusion components were compared to the DNS data provided by Huser [19] and shown in Fig. 58 (b). According to the figure, the calculation was able to give reasonable pressure diffusion values. From Fig. 58, the correctness of the pressure diffusion calculation could be ensured.
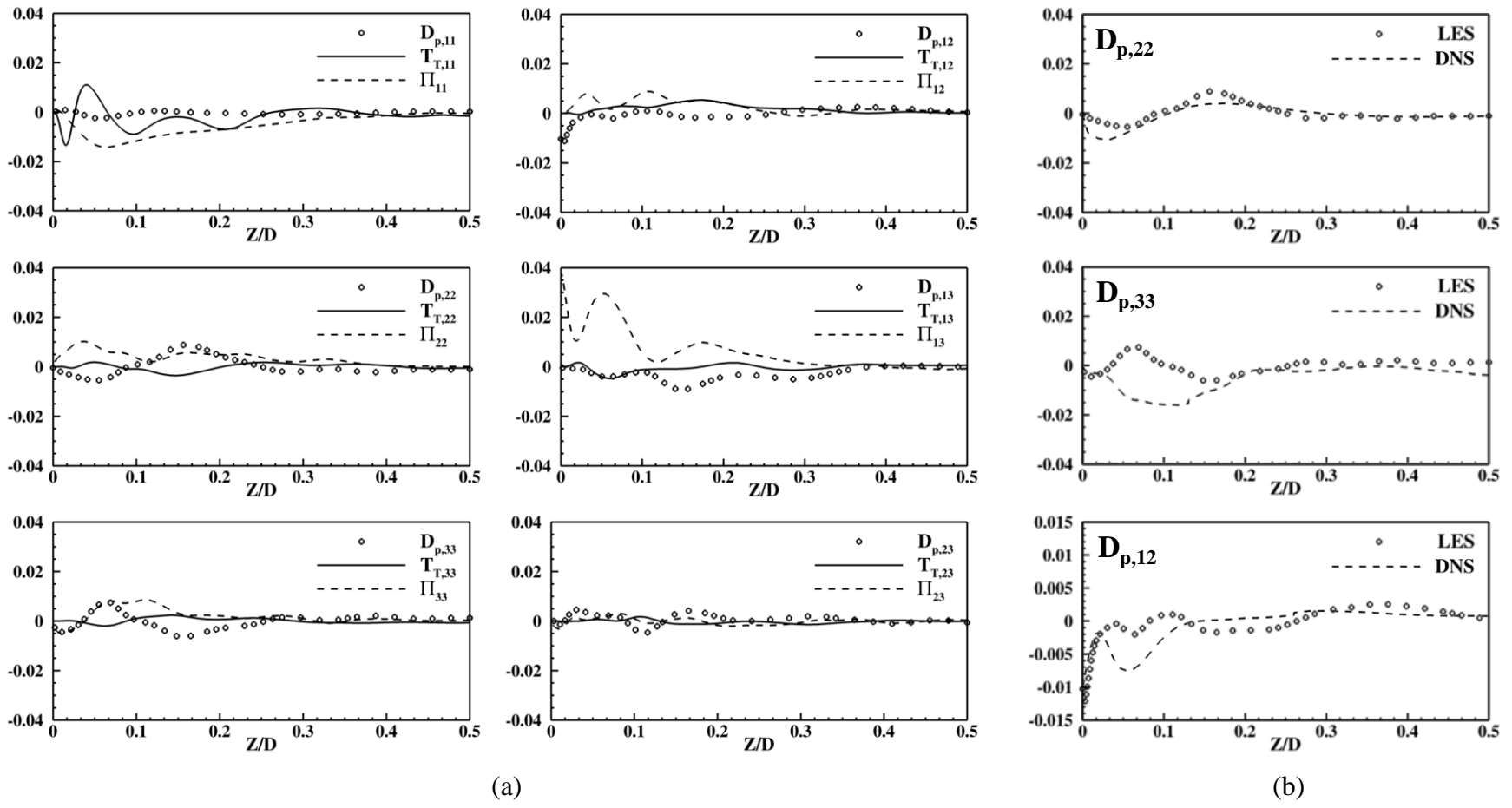
Figure 58. Budget terms analyses for square straight duct with fine-O grid in Figs. 25 and 26 on Y/D = 0.5 : (a) the pressure diffusion vs. turbulent transport vs. the pressure-strain rate, (b) comparison of the pressure diffusion between LES data and the DNS data provided by Huser [19].

REFERENCES

[1] Shih, T.I-P. and Yang, V., Editors, Turbine Aerodynamics, Heat Transfer, Materials, and Mechanics, Progress in Astronautics and Aeronautics, Vol. 243, American Institute of Aeronautics and Astronautics, 2014.

[2] Shevchuk, I. V., Jenkins, S. C., Von Wolfersdorf, J., Weigand, B., Neumann, S. O., and Schnieder, M., "Validation and Analysis of Numerical Results for a Varying Aspect Ratio Two-Pass Internal Cooling Channel," *Journal of Heat Transfer*, Vol. 133, No. 5, Jan. 2011, 051701.

[3] Su, G., Chen, H. C., Han, J. C., and Heidmann, J. D., 2004, "Computation of Flow and Heat Transfer in Two-Pass Rotating Rectangular Channels (AR=1:1, AR=1:2, AR=1:4) With 45-Deg Angled Ribs by a Reynolds Stress Turbulence Model," *ASME Turbo Expo 2004: Power for Land, Sea, and Air*, Vol. 3, *ASME Paper*, 2004, No. GT2004-53662, pp. 603-612.

[4] Wang, T. S., and Chyu, M. K., "Heat Convection in a 180-Deg Turning Duct with Different Turn Configurations," *Journal of. Thermophysics and Heat Transfer*, Vol. 8, No. 3, 1994, pp. 595–601.

[5] Liou, T. M., and Chen, C. C., "LDV Study of Developing Flows Through a Smooth Duct With a 180 Deg Straight-Corner Turn," *Journal of Turbomachinery*, Vol. 121, No. 1, Jan. 1999, pp. 167–174.

[6] Liou, T. M., Tzeng, Y. Y., and Chen, C. C., "Fluid Flow in a 180 Deg Sharp Turning Duct With Different Divider Thicknesses," *ASME Journal of Turbomachinery*, Vol. 121, No. 3, Jul. 1999, pp. 569–576.

[7] Smith, M. A., Mathison, R. M., Dunn, M. G., "Heat Transfer for High Aspect Ratio Rectangular Channels in a Stationary Serpentine Passage with Turbulated and Smooth Surfaces," *ASME Journal of Turbomachinery*, Vol. 136, No. 5, Sep. 2013, 051002.

[8] Apsley, D., and Leschziner, M., "Advanced Turbulence Modelling of Separated Flow in a Diffuser," *Flow, Turbulence and Combustion*, 2000, 631/4, pp. 81–112.

[9] Wallin, S. and Johansson, A. V., "An Explicit Algebraic Reynolds Stress Model for Incompressible and Compressible Turbulent Flows," *Journal of Fluid Mechanics*, Vol. 403, 2000, pp. 89–132.

[10] Pope, S. B., 2000, "Turbulent Flows," Cambridge University Press, Cambridge, UK.

[11] Wilcox, D. C., "Turbulence Modeling: An Overview," 39th Aerospace Sciences Meeting and Exhibit, AIAA Paper, 2001, No. 2001-0724.

[12] Patel, V. C., Rodi, W., and Scheuerer, G., "Turbulence Models for NearWall and Low-Reynolds-Number Flows: A Review," *AIAA Journal*, Vol. 23, No. 9, 1985, pp. 1308– 1319.

[13] Sarkar, A., and So, R. M. C., "A Critical Evaluation of Near-Wall TwoEquation Models Against Direct Numerical Simulation Data," *International Journal of Heat and Fluid Flow*, Vol. 18, No. 2, April 1977, pp. 197–208.

[14] Lin, Y.-L., Shih, T. I.-P., Stephens, M. A., Chyu, M. K., "A Numerical Study of Flow and Heat Transfer in a Smooth and Ribbed U-duct With and Without Rotation," *ASME Journal of Heat Transfer*, Vol. 123, No. 2, Sep. 2000, pp. 219-232.

[15] Metais, O., Salinas-Vasquez, M., "Large-eddy Simulation of Turbulent Flow Through a Heated Square Duct," *Journal of Fluid Mechanics*, Vol. 453, Feb. 2002, pp. 201-238..

[16] Hebrard, J., Metais, O., Salinas-Vasquez, M., "Large-eddy Simulation of Turbulent Duct Flow: Heating and Curvature Effects," *International Journal of Heat and Fluid Flow*, Vol. 25, No. 4, Aug. 2004, pp. 569-580.

[17] Munch, C., "Large Eddy Simulation of the Turbulent Flow in Heated Curved Ducts: Influence of the Reynolds Number" *TSFP4 Williamburg, VA, USA*

[18] Guleren, K. M., Turan, A. "Validation of Large-Eddy Simulation of Strongly Curved Stationary and Rotating U-Duct Flows," *International Journal of Heat and Fluid Flow*, Vol. 28, No. 5, Oct. 2007, pp. 909-921.

[19] Huser, A. and Biringen, S., 1993, "Direct Numerical Simulation of Turbulent Flow in a Square Duct", *J.-Fluid-Mech.*, 257, pp. 65-95.

[20] Gavrilakis, S., "Numerical simulation of low-Reynolds-number turbulent flow through a straight square duct," *J. Fluid Mech.*, 244, 1992.

[21] Y. Joung, S. Choi, J. Choi, "Direct Numerical Simulation of Turbulent Flow in a Square Duct: Analysis of Secondary Flows," *Journal of Engineering Mechanics*, 2007.

[22] Raiesi, H., Piomelli, U., Pollard, A., 2011, "Evaluation of Turbulence Models Using Direct Numerical and Large-Eddy Simulation Data," *ASME, J. Fluids Eng.*,133, 021203-1.

[23] Shih, T. I-P. and Durbin, P. A., 2014, "Modeling and Simulation of Turbine Cooling," Turbine Aerodynamics, Heat Transfer, Materials, and Mechanics. T. Shih and V. Yang, eds., Progress in Astronautics and Aeronautics, Vol. 243, American Institute of Aeronautics and Astronautics, pp. 389-421.

[24] Ooi, A., Iaccarino, G., Durbin, P., and Behnia, M., 2002, "Reynolds Averaged Simulation of Flow and Heat Transfer in Ribbed Ducts," *Int. J. Heat and Fluid Flow*, Vol. 23, No. 6, pp. 750-757.

[25] Durbin, P.A. and Shih, T.I-P., "An Overview of Turbulence Modeling," Modelling and Simulation of Turbulent Heat Transfer, Edited by B. Sundén and M. Faghri, WIT Press, Ashurst, Southhampton, 2005, Chapter 1, pp. 3-31.

[26] Parneix, S., Laurence, D., and Durbin, P. A., 1998, "A Procedure for Using DNS Databases," *ASME J. Fluids Eng.*, 120(1), pp. 40–47.

[27] Shih, T.-H., Liou, W., Shabbir, A., and Zhu, J., "A New k-ε Eddy-Viscosity Model for High Reynolds Number Turbulent Flows – Model Development and Validation," *Computers and Fluids*, Vol. 24, No. 3, 1995, pp. 227-238.

[28] Launder, B.E. and Spalding, D.B., "The Numerical Computation of Turbulent Flows," *Computer Methods in Applied Mechanics and Engineering*, Vol. 3, 1974, pp. 269-289.

[29] Menter, F.R., Zonal Two-Equation k-ω Turbulence Models for Aerodynamc Flows, *AIAA Paper* 93-2906, 1993.

[30] Menter, F.R. and Rumsey, C.L., Assessment of Two- Equation Turbulence Models for Transonic Flows, *AIAA Paper* 94-2343, 1994.

[31] Wilcox, D.C., Turbulence Modeling for CFD, DCW Industries, Inc., La Canada, California, 1993.

[32] F. R. Menter, M. Kuntz and R. Langtry, "Ten Years of Industrial Experience with the SST Turbulence Model" 2003.

[33] Lien, F. S. and Leschziner, M.A., 1994, "Assessment of Turbulent-Transport Models Including Non-Linear RNG Eddy-Viscosity Formulation and Second-Moment Closure for flow over a backward-facing step," *Computers and Fluids*, Vol. 23, No. 8, pp. 983-1004.

[34] Fu, S., Launder, B.E., and Leschziner, M.A., 1987 , "Modeling Strongly Swirling Recirculating Jet Flow with Reynolds-Stress Transport Closures," *Sixth Symposium on Turbulent Shear Flows*, Toulouse, France.

[35] Gibson, M. M. and Launder, B. E., 1978, "Ground Effects on Pressure Fluctuations in the Atmospheric Boundary Layer," *J. Fluid Mech.*, Vol. 86, pp. 491-511.

[36] Tannehill, J.C., Anderson, D.A., and Pletcher, R.H., Computational Fluid Dynamics and Heat Transfer, 2nd edition, Taylor & Francis, Washington, 1997.

[37] Shih, *T. I-P., "Mathematical Models for the Numerical Study of Turbulent Flows," Journal of the Chinese Institute of Engineers*, Vol. 11, 1988, pp. 121-136.

[38] Shih, T. I-P., and Sultanian, B., "Computations of Internal and Film Cooling," Heat Transfer in Gas Turbines, Editors: B. Sundén and M. Faghri, WIT Press, Ashurst, Southhampton, 2001, Chapter 5, pp. 175-225.

[39] http://www.fluent.com/software/fluent/index.htm.

[40] Chyu, M. K., Ding, H., Downs, J. P., and Soechting, F. O., "Determination of Local Heat Transfer Coefficient Based on Bulk Mean Temperature Using a Transient Liquid Crystal Technique," *Journal of Experimental Thermal and Fluid Science*, Vol. 18, No. 2, 1998, pp. 142–149.

[41] Sathyanarayanan, S.K. and Shih, T.I-P., "Time-Accurate Conjugate Analysis of Transient Measurements of Heat-Transfer Coefficients," *AIAA Journal of Thermophysics and Heat Transfer*, Vol. 31, No. 3, 2017, pp. 527-537 doi: 10.2514/1.T4723.

[42] Nicoud, F., and Ducros, F., 1999, "Subgrid-scale stress modelling based on the square of the velocity gradient tensor," *Flow, Turbul. Combust.*, pp. 183–200.

[43] Lampitella, P., "Large Eddy Simulation for Complex Industrial Flows." *PhD Thesis*, 2014

[44] Celik, I., Cehreli, Z., Yavuz, I., "Index of Resolution Quality for Large Eddy Simulation," *Journal of Fluid Engineering*, Vol. 127, 2005, pp. 949-58.

[45] Taylor, GI., " The Spectrum of Turbulence" *Proc. R. Soc. Land. A* 164:476-90.

[46] George, W. K., *Lectures in Turbulence for the 21st Century*, (Chalmers University of Technology, 2009), pp. 209.

[47] Leutheusser, H.J. "Turbulent flow in rectangular ducts," *Journal of Hydr. Div. ASCE*, Vol. 89(3), 1963, 1-19.

[48] Knight, D.W., Demetriou, J.D., Hamed, M.E., "Boundary shear in smooth rectangular channels," *Journal of Hydraulic Engineering*, ASCE, Vol. 110(4), 1984, 405-422.

[49] Brundrett, E., Baines, W. "The production and diffusion of vorticity in duct flow." *Journal of Fluid Mech.*, Vol. 19, 1964, 375–394.

[50] Gessner, F.B., Po, J.K., Emery, A.F., "Measurement of developing turbulent flow in a square duct," *Turbulent Shear Flows I*, p. 119, Springer, 1979.

[51] Niederschulte, M.A., "Turbulent flow through a rectangular channel," *Ph.D. thesis*. University of Illinois, Urbana, 1989.

[52] B. E. Launder, G. J. Reece, and W. Rodi, 1975, "Progress in the Development of a Reynolds-Stress Turbulence Closure," *J. Fluid Mech.*, 68(3):537-566.

[53] Mansour, N. N., Kim, J., Moin, P., 1988, "Reynolds-stress and dissipation rate budgets in a turbulent channel flow," *J. Fluid Mech.* 194, 15.

PUBLICATIONS

1. Hu, "Kenny" Shih-yung, "Heat Transfer Enhancement in Thermoelectric Power Generation" (2009).*Graduate Theses and Dissertations.* 12196. *AIAA 2009-1210 Jan. 2009*. 12196. https://lib.dr.iastate.edu/etd/12196

2. Hu "Kenny" S.-Y., Chi, X., Shih, T.I-P., Bryden, K.M., Chyu, M.K., Ames, R., and Dennis, R.A., "Flow and Heat Transfer in the Tip-Turn Region of a U-Duct Under Rotating and Non-Rotating Conditions," *ASME paper GT2011-46013, Turbo Expo: Power for Land, Sea, and Air, Volume 5: Heat Transfer, June 2011, Vancouver, Canada* ,doi:10.1115/GT2011-46013.

3. Kenny S.-Y. Hu, Xingkai Chi, Minking Chyu, Michael Crawford, and Tom I-P. Shih, "Steady RANS of Flow and Heat Transfer in a Smooth and Pin-Finned U-Duct with a Trapezoidal Cross Section," *ASME Journal of Engineering for Gas Turbines and Power GTP-18-1307, Proceeding of ASME TurboExpo 2018, Turbomachinery Technical Conference & Exposition, June 2018, Oslo, Norway*.

4. Kenny S.-Y. Hu and Tom I-P. Shih, "Large-Eddy and RANS Simulations of and Heat Transfer in a U-Duct with a High Aspect Ratio Trapezoidal Cross Section," *GT-2018-75535, Proceeding of ASME TurboExpo 2018, Turbomachinery Technical Conference & Exposition, June 2018, Oslo, Norway*.

5. Kenny S.-Y. Hu and Tom I-P. Shih, "Large-Eddy vs. RANS Simulations in Predicting Flow and Heat Transfer in a U-Duct with a Trapezoidal Cross Section," *AIAA paper 2018-4432, 2018 Joint Propulsion Conference. AIAA Propulsion and Energy forum, July 2018, Cincinnati, Ohio,* https://doi.org/10.2514/6.2018-4432.